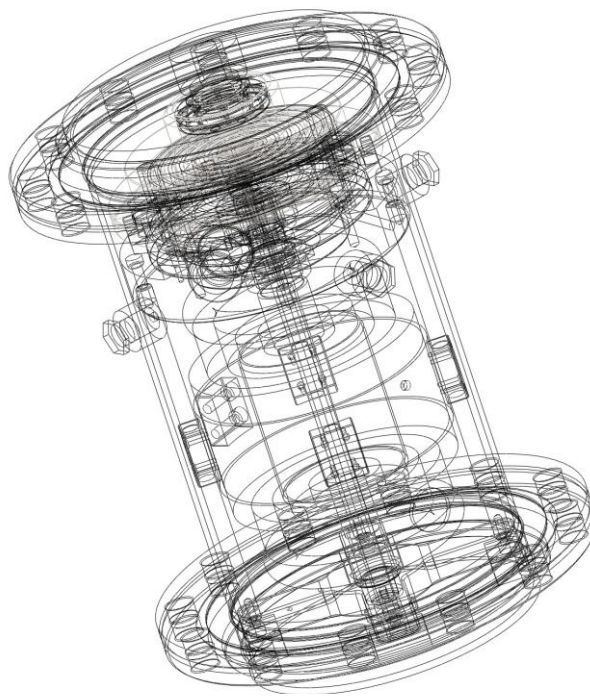

Design and fabrication of a variable wall thickness two-stage scroll expander to be integrated in a micro-solar power plant

by
Rémi DICKES



Thesis submitted in partial fulfillment of the requirements
for the degree of
Electromechanical Engineer
(Energy engineering)

Mens et Manus

To my grandparents

Design and fabrication of a variable wall thickness two-stage scroll expander to be integrated in a micro-solar power plant

by

Rémi DICKES

Master thesis submitted on August 20th 2013 to the Faculty of Applied Sciences of the
University of Liège in partial fulfilment for the requirements for the degree of
Electromechanical Engineer

Improving access to energy in developing countries without exacerbating climate change requires novel technical strategies. Micro-CSP power plants using organic Rankine cycles (ORCs) are one example of a promising approach for meeting this challenge. Specifically, expander development has been identified as a critical component for enhancing the performances of small ORC units. The goal of this project is to develop an optimized two-stage scroll expander to be integrated in a micro-CSP power plant designed to supply remote, off-grid areas.

The expansion requirements are firstly defined so as to meet production specifications. Then, employing a deterministic model and a selection process, optimal scroll geometries are chosen for both expansion stages. The deterministic model is executed with Matlab and accounts for the relevant physical phenomena i.e. radial and flank leakages, throttling losses at the intake and exhaust processes, friction between the two scrolls and mechanical losses in the different bearings. A performance enhancement of about 6% of the isentropic efficiency is predicted in comparison with baseline practice.

A CAD model of a single-stage prototype is developed in Solidworks following the main architectural features of a compliant HVAC scroll compressor. This CAD is updated and improved with the optimal scroll geometries and some parts are 3D printed to verify their mechanical assembly. Toolpaths to control CNC machines are generated using the CAM program HSMXpress and the parts constituting the expander prototype are manufactured in a machine shop.

In conclusion, the properties of the enhanced scroll expander are evaluated in the context of a typical Micro-CSP plant. A simple steady state model in EES is developed to quantify how three parameters (T_{ev} , T_{cond} and η_{exp}) influence the power plant overall sunlight to electricity conversion efficiency (a gain of 0.73% is predicted). This project underscores the importance of optimizing the expansion process and identifies further research pathways to progress towards this goal.

Acknowledgment

There are many people I would like to thank for their contribution in this project.

To begin with, I would like to thank Sylvain Quoilin who gave the priceless opportunity to spend a semester at MIT, but also Pr. Lemort from Liège and Pr. Hemond from MIT who accepted this internship.

I would like to convey my sincere thanks to my family for their unqualified support all along my studies, and especially to my mother who welcomed me several times this last few month to offer me a place that I could call "Home" on the other side of the Atlantic.

I would also like to thank Bertrand Dechesne for his time given to answer to my questions and for his help in many ways.

Jordan Henrotte, my old friend I haven't seen for ages, thanks to have provided me a priceless computer resource when I had to run my models.

A special thank to Amy Mueller who made me save a lot of time by developing the edge finders code, but also for letting me use her computer for days so I could get my database in time.

Thank to Mark Belanger who gave me access to his machine shop when I needed it and who answered to my practical questions when I was in trouble.

Thanks to my American friends without whom my experience in the USA would not have been the same.

To Co, my sweet, for her help, her presence and her unconditional support she has given me since we have been together, *grazie mille*.

And last but not least, I want to express my deepest gratitude to Matt Orosz, my *boss*, who taught me the true meaning of "work" ... but also who gave me the opportunity to work on a project combining humanitarian aspect, renewable technologies and technical challenge. He helped me so many times for so many things and without him this internship would not have been so fantastic to me. Once again, thank you!

Contents

Abstract	3
Acknowledgment	3
List of Figures	7
List of Tables	10
Acronyms	12
Symbols	13
Sub/superscripts	14
1 Introduction	15
1.1 Context	15
1.2 Description and History of the ORC technology	16
1.3 Description and History of Scroll machines	21
1.4 Thesis overview	29
2 Deterministic modeling of a scroll expander	30
2.1 Geometric model overview	31
2.2 Thermodynamic model overview	35
2.2.1 Modeling principle	36
2.2.2 Mass flows	38
2.3 Mechanical losses	41
2.3.1 Friction between the scrolls	41

2.3.2	Journal bearing losses	41
2.3.3	Thrust bearing losses	44
2.3.4	Sensitivity study	45
3	Selection of optimal scroll geometries	48
3.1	Operating condition requirements	48
3.2	Scroll generation	49
3.2.1	Danfoss frame	49
3.2.2	Parameter domains	51
3.2.3	Minimum wall thickness requirements	55
3.3	Selection strategy	59
3.4	Results discussion	61
3.4.1	First stage geometry	61
3.4.2	Second stage	62
3.4.3	Overall expansion	65
4	Prototype architecture and CAD modeling	71
4.1	Architecture and pieces description	71
4.1.1	Overall architecture	72
4.1.2	Fixed and orbiting scrolls	74
4.1.3	Electric generator	76
4.1.4	Casing elements and fixtures	77
4.1.5	Bearings	79
4.1.6	Counterweight, shaft adapter and Oldham joint	81
4.1.7	Lubrication circuit	82
4.2	3D printing	83
4.3	CAM with HSMXpress	83
4.4	Draft of the two-stage/single-shaft scroll expander	85
5	Manufacturing of a single stage prototype	86
5.1	Machines an tools	86
5.1.1	Machines	86
5.1.2	Tools	88
5.2	Elements of manufacturing theory	91
5.2.1	Measurement systems	91
5.2.2	Feed rate, depth of cut and cutting speed	93
5.2.3	MIG welding	95
5.2.4	Tolerance and fits	96
5.3	Materials selection	97
5.4	Operations summary and assembly	100

6	MicroCSP test rig	104
6.1	CSP description	104
6.2	Micro-CSP performance modeling	110
6.2.1	Influence of the condensing temperature	110
6.2.2	Influence of the expansion efficiency	111
6.2.3	Influence of the evaporating temperature	114
6.2.4	Results comparison	117
7	Conclusion and perspectives	119
	Appendix	120
	Bibliography	121

List of Figures

1.1	Rankine cycle principle	16
1.2	T-s diagram for steam and different organic fluids (source: Sylvain Quoilin [26])	18
1.3	Dish Stirling	22
1.4	Solar Power Tower	22
1.5	Parabolic through collectors (PTC)	22
1.6	Linear Fresnel collectors	22
1.7	Scroll expander principle	24
1.8	Radial and flank leakages occuring in a scroll expander	25
1.9	Type of possible designs	26
1.10	Example of a circle involute aka <i>Archimedean spiral</i>	26
1.11	Mathematical description of a constant wall thickness scroll geometry	27
1.12	Isentropic efficiency as a function of the compactness factor [10]	28
1.13	Variable wall thickness scroll compressor built by Copeland	28
2.1	Lemort's semi-empirical model of a scroll expander	30
2.2	Deterministic model overview	31
2.3	Inlet port	33
2.4	Exhaust port	34
2.5	Leakage length between one pair of P1 and P2	34
2.6	Evolution of pocket volume as a function of the crank angle	35
2.7	Outlet temperature convergence	38
2.8	Overall model architecture	39
2.9	Normal vector along the orbiting scroll	43
2.10	Resulting radial force - magnitude and direction	44
2.11	Isentropic efficiency in function of the oil film thickness ([5 – 50] μm) and the oil fraction ([50 – 100]%)	46
2.12	Isentropic efficiency in function of the oil film thickness ([5 – 50] μm) and the oil fraction ([50 – 100]%)	47
3.1	Two stage expansion diagrams	50
3.2	Scroll generation	51

3.3	Parameters inter-dependence	52
3.4	Lower (yellow) and upper (blue) domain limits	52
3.5	Orosz et. al.'s model algorithm	53
3.6	Hierarchical parameters selection	53
3.7	Cantilever beam theory	55
3.8	Pressure difference along the scroll	56
3.9	Selection process diagram	58
3.10	Comparison between the actual wall thickness (blue) and the minimum one required (magenta) in case of an over/under- expansion	58
3.11	Pressure difference along the scroll	59
3.12	Selection process diagram	60
3.13	Three types of geometry investigated	60
3.14	Relation between compactness factor and isentropic efficiency (first stage candidates)	62
3.15	Scroll geometry selected for the first stage	63
3.16	Mechanical losses fraction in the first stage	64
3.17	Relation between compactness factor and isentropic efficiency (second stage candidates)	64
3.18	Scroll geometry selected for the second stage	66
3.19	Mechanical losses fraction in the second stage	67
3.20	Pressure profile in each pocket	68
3.21	Temperature profile in each pocket	68
3.22	Enthalpy profile in each pocket	68
4.1	Overall scroll expander	72
4.2	Exploded view of the expander	73
4.3	Scrolls	74
4.4	BPC gaskets	75
4.5	BPC and pressure holes	76
4.6	Induction generator	77
4.7	Generator rotor design features	78
4.8	Fixtures and casing	80
4.9	Journal bearings (left) and thrust bearing (right) of the ex- pander prototype	80
4.10	Counterweight (left), shaft adapter (middle) and Oldham joint (right)	81
4.11	BPC (red) and lubrication (blue) circuits	82
4.12	Pieces 3D printed with a FDM printer	83
4.13	Tool paths generated for the Oldham joint	84
4.14	Draft overview of the two-stage prototype	85

5.1	Lathe + DRO	89
5.2	CNC milling machine	89
5.3	Horizontal bandsaw	89
5.4	MIG welding station	90
5.5	Coolant system	90
5.6	Lathe tools	92
5.7	Drilling tools	92
5.8	Tapping tools	92
5.9	Milling tools	92
5.10	Effect of the workpiece material on the cutting speed	94
5.11	Effect of the tool material on the cutting speed	94
5.12	MIG welding principle	95
5.13	Welding equipments	95
5.14	ISO types of tolerance	97
5.15	ISO fits	98
5.16	All the manufactured pieces	102
5.17	Assembly - Step A	103
5.18	Assembly - Step B	103
5.19	Assembly - Step C	103
5.20	Assembly - Step D	103
6.1	Working principle of a Micro-CSP system (source: STG international)	105
6.2	Heating element	106
6.3	P&I diagram of a Micro-CSP (source: STG international)	107
6.4	Parabolic trough collectors of the test rig	109
6.5	ORC unit of the test rig	109
6.6	Condenser and thermal tank of the test rig	109
6.7	T-s and h-s diagrams of the ORC cycle under nominal conditions	111
6.8	ORC performance in function of the condensing temperature	112
6.9	ORC performance as a function of the expansion efficiency	113
6.10	ORC performance as a function of the evaporating temperature	114
6.11	High pressure as a function of the "evaporating" temperature	115
6.12	Temperature distribution along a PTC for the HTF, the absorber tube and the cover tube (source: Ashraf Kotb [15])	116
6.13	PTC thermal efficiency in function of the HTF temperature (source: SopoNova datasheet)	116
6.14	η_{PTC} , η_{ORC} and $\eta_{MicroCSP}$ in function of the evaporating temperature	117

List of Tables

1.1	Comparison summary between ORCs and Rankine cycles . . .	19
3.1	Steady state model inputs and results	49
3.2	Performance table for the first stage	63
3.3	Influence of losses on the isentropic efficiency - first stage . . .	65
3.4	Performance table for the second stage	66
3.5	Influence of losses on the isentropic efficiency - second stage .	67
3.6	Thermophysical properties of the full expansion	69
3.7	Comparison of the performance of the Design A, B and C . . .	70
5.1	Tool materials used in the project	90
5.2	US and SI systems comparison	93
5.3	Mechanical properties of the selected materials	99
5.4	Operation summary table	101
6.1	Technical specification of the Micro-CSP plant	108
6.2	Nominal conditions	110
6.3	ORC performance in function of the condensing temperature .	112
6.4	ORC performance as a function of the expansion efficiency .	113
6.5	ORC performance as a function of the evaporating temperature	114

Acronyms

BPC	B ack P ressure C hamber
CAD	C omputer- A ided D esign
CAM	C omputer- A ided M anufacturing
CF	C ompactness F actor
CFD	C omputational F luid D ynamics
CNC	C omputer N umerical C ontrol
CSP	C oncentrated S olar P ower
DCF	D iscounted C ash F low
DRO	D igital R ead O ut
EES	E ngineering E quation S olver
FDM	F used D eposition M odeling
GMAW	G as M etal A rc W elding
HP	H igh P ressure
HSS	H igh S peed S teel
HTF	H eat T ransfer F luid
HVAC	H eating V entilation A ir C onditioning
LP	L ow P ressure
MIG	M etal I nter G as
OF	O rganic F luid
ORC	O rganic R ankine C ycle
SW	S olid W orks
TIG	T ungsten I nter G as
WF	W orking F luid

Symbols

A	Area	m^2
c	Radial clearance	m^2
D	Diameter	m
E	Young modulus	MPa
f	Losses coefficient	$[-]$
F	Force	N
G	Gap	m
h_1	Enthalpy	J/kg
h_2	Height	m
k	Constant	$[-]$
L	Length	m
M	Mass	kg
\dot{M}	Mass flow	kg/s
n	Curves resolution	$nbrpoints$
N	Spindle speed	rpm
P	Pressure	Pa
Q	Heat	J
r	Radius	m
r_v	Volumetric ratio	$[-]$
Re	Reynolds number	$[-]$
t	Thickness	m
T	Temperature	$^{\circ}C$ or K
s	Entropy	$J/kg.K$
S	Sommerfeld number	$[-]$
u	Specific internal energy	J/kg
U	Internal energy	J
v	specific volume	m^3/kg
V_1	Volume	m^3
V_2	Linear velocity	m/s
W	Work	J
\dot{W}	Power	W
x	Fraction	$\%$
X	Domain limits	$[-]$
δ	Wall deflection	m

η	Efficiency	%
γ	Heat capacity ratio	[—]
μ	dynamic viscosity	P
ρ	Density	kg/m^3
θ	Crank angle	rad
φ	Tangent or involute angle	rad
ω	Spindle speed	rad/s

Sub/superscripts

<i>c</i>	cold
<i>cond</i>	condensing
<i>crit</i>	crit
<i>e</i>	electric
<i>ev</i>	evaporating
<i>ex</i>	exhaust
<i>fric</i>	friction
<i>in</i>	inlet or intern
<i>init</i>	initial
<i>is</i>	isentropic
<i>flk</i>	flank
<i>exp</i>	expansion
<i>h</i>	hot
<i>max</i>	maximum
<i>min</i>	minimum
<i>rad</i>	radial
<i>ref</i>	refrigerant
<i>scl</i>	scroll
<i>TB</i>	thrust bearing
<i>th</i>	teeth
<i>tot</i>	total

Chapter 1

Introduction

This document reports on research undertaken by Rémi DICKES during the academic year 2012-2013, in fulfillment of a masters degree in electromechanical engineering. The main part of this thesis has been realized during a five month internship at the Parsons Laboratory of MIT (*Massachusetts Institute of Technology*), under the supervision of Dr. Sylvain QUOILIN (University of Liège) and Dr. Matthew S. OROSZ (MIT - STG International). The global objective of this project is to design and build a variable wall thickness scroll expander to be integrated in a micro-solar power plant. This chapter first gives an overview of context and issues related to this work, followed by a full description of Organic Rankine Cycle (ORC) and scroll machines. Finally, the overall thesis architecture is described with a brief summary of each chapter.

1.1 Context

Since the first industrial revolution in the early XIXth century, humanity has witnessed an exponential development of societies based on fossil fuels. Consumption (some would argue over-consumption) of energy resources has led to social benefits as well as tensions on many level: global climate change, exhaustion of oil reserves, destruction of ecosystems and extinction of species are common themes in modern discourse. While ecologically motivated reactions to these tensions began to emerge in the 1960's, by the second decade of the 21st century it has become generally accepted that the development of renewable energy technologies and optimization of energy systems is necessary to ensure a sustainable future for subsequent generations.

Although the majority of the world has achieved a certain level of development, over 15 % of the Earth's population still lives in precarious conditions without easy access to electricity and tap water [3]. Furthermore, most of

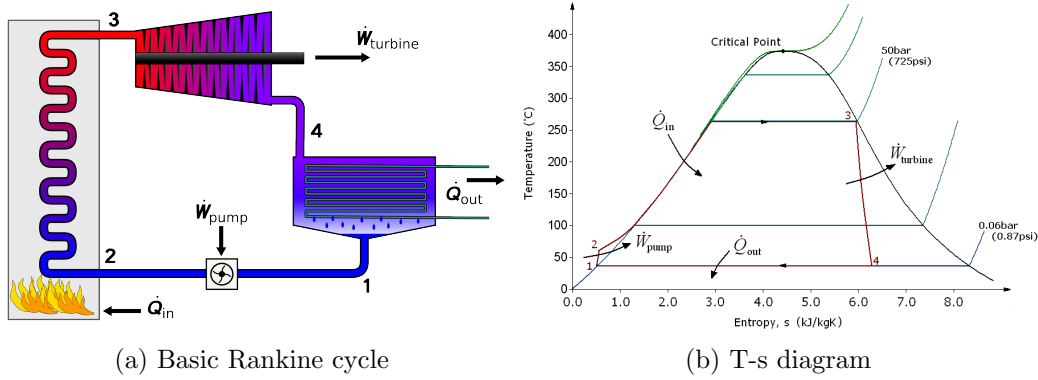


Figure 1.1: Rankine cycle principle

those developing regions (e.g. Sub-Saharan Africa countries and India) possess favorable insolation conditions during much of the year.

It is in this context that, in 2006, the non-profit organization *STG International* started a project to develop a small scale CSP system (aka μ -CSP) based on ORC technology in order to produce electricity and hot water in remote areas of developing countries (see www.stginternational.org). In the course of this project, the relative scarcity of suitable expansion machines became apparent, thus motivating the research by Dechesne [10] which this work builds upon and further develops.

1.2 Description and History of the ORC technology

Like the *Brayton*, *Stirling* or *Ericsson* cycles, a *Rankine* cycle is an ideal thermodynamic model which describes the conversion of heat into mechanical work. It is named after the Scottish engineer and physicist William John Macquorn Rankine (1820- 1872) who was – together with Carnot, Thomson, Clausius and many others – a founding contributor of the field of thermodynamics. Widely developed, 90 % of electricity capacity worldwide is generated by technologies based on the Rankine cycle, such as nuclear, coal, oil or biomass power plants [4].

As shown in Figure 1.1, a Rankine cycle is a closed loop cycle in which the working fluid undergoes four successive processes:

- **Isentropic compression ($1 \Rightarrow 2$)** – The working fluid is compressed in a pump. Because of the low specific volume of the liquid, the work required is relatively small and often negligible for a steam cycle.

- **Isobaric heating ($2 \Rightarrow 3$)** – The high pressure liquid is heated up by an external source. Moreover, the higher the maximum cycle temperature, the higher the related Carnot efficiency.
- **Isentropic expansion ($3 \Rightarrow 4$)** – The hot and high pressure vapor is then expanded in a turbine or an expander which generates mechanical power. This work can be used to power any mechanical systems or a generator in order to produce electricity.
- **Isobaric cooling ($4 \Rightarrow 1$)** – The vapor-liquid mixture leaving the expansion process is then condensed at low pressure (often below the atmospheric pressure, depending on the selected working fluid).

One can summarize the principle of the Rankine cycle as follows: the work required to compress a cold liquid from a pressure P_1 to P_2 is smaller than the work obtained by expanding its hot vapor phase from P_2 to P_1 . In practice however, power plants are based on cycles much more complex than the one described above, e.g. in order to improve the global efficiency of the plant, strategies such preheating, reheating or regeneration are often employed.

Unlike traditional Rankine cycles based on water and steam, *Organic Rankine Cycles* use organic compounds as working fluid. By definition an organic fluid (*OF*) is a fluid whose molecules contain at least one carbon atom. Different kinds of organic fluids have been used so far and can be classified as follow:

- **CFCs** : Chlorofluorocarbons contain only fluorine, chlorine and carbon. CFCs have been removed from the market since the Montreal protocol in 1987 because of their active contribution to ozone depletion in the upper atmosphere. Examples of CFCs are R11 and R12.
- **HCFCs** : Hydrochlorofluorocarbon compounds contain hydrogen, fluorine, chlorine and carbon. Like CFCs, HCFCs have also been phased out the market for the same reason. Examples of HCFCs are R22 or R123.
- **HFCs** : Hydrofluorocarbons contain only a few fluorine atoms, hydrogen and carbon. As they don't contain any chlorine, they are harmless regarding ozone depletion; however they may still exhibit high Global Warming Potential (GWP). Examples of HFCs are R134 or R245fa.
- **HCs** : Hydrocarbons contain only carbon and hydrogen atoms. Like HFCs, HCs are harmless to the ozone layer since they do not contain any chlorine. Examples of HCs are *isobutane* or *pentane*.

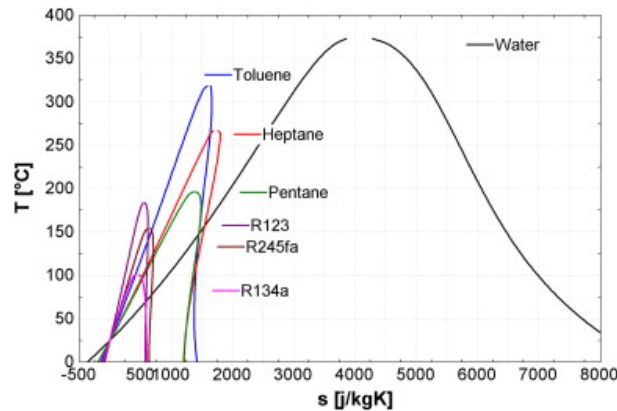


Figure 1.2: T-s diagram for steam and different organic fluids (source: Sylvain Quoilin [26])

Water and organic fluids have fundamentally different properties. Indeed, several observations can be made from Figure 1.2 which represents the Temperature-specific entropy (T - s diagram) of water and different OFs. First of all, one can see that organic fluids have a boiling point at a lower temperature than steam. This property allows the Rankine cycle to operate with low temperature heat sources, which significantly extends its range of applications. Secondly, organic fluids show a more vertical (or even positive) slope along the saturated vapor curve of their T-s diagram. Three main consequences result from this:

1. The expansion can be completely dry without having to superheat the saturated vapor. There is thus no need to reach a higher temperature than the boiling point for a given saturation pressure. Moreover, the absence of liquid in the expander improves its efficiency and extends its life expectancy.
2. The working fluid remains superheated at the end of the expansion process. One can thus install a recuperator between the expander outlet and the pump outlet in order to preheat the working fluid at the entrance of the evaporator. On one hand, it reduces the amount of energy required to reach the saturated vapor state. On the other hand, it decreases the pinch gap between the two temperature profiles in the boiler which reduces irreversibilities of the heat exchange. It also reduces heat losses rejected in the condenser.
3. Organic fluids present a lower enthalpy of vaporization. The required mass flow rate is therefore higher for an ORC system than for a steam cycle

Advantages of ORCs	Drawbacks of ORCs
<ul style="list-style-type: none"> • Lower boiling point <ul style="list-style-type: none"> – Larger range of application (heat recovery possible) – Less thermal stress on boiler and expansion device • Dry fluids <ul style="list-style-type: none"> – Better expansion efficiency – Increase expansion devince lifetime – No over heating required – Recuperator between • Lower evaporating pressure • Higher condensing pressure • Smaller latent energy 	<ul style="list-style-type: none"> • Higher pump consumption • Better water properties <ul style="list-style-type: none"> – Availability – Not toxic – Not flammable – Environmentally friendly • Lower cycle efficiency because of Carnot limitation

Table 1.1: Comparison summary between ORCs and Rankine cycles

Finally, ORCs require a much lower evaporating pressure, which is beneficial to the unit safety and to the simplicity of the components. Moreover, organic fluids condense to a pressure higher than P_{atm} which avoids infiltration inside the cycle in the event of manifold leaks.

However, apart from these advantages, ORCs also present some drawbacks in comparison to a regular steam cycle. First of all, water is a better working fluid in many regards: it is widely available, not toxic, not flammable, natural and is environmentally harmless (from a global warming and ozone depletion perspective). Secondly, lower temperatures achieved by ORCs penalize considerably the related Carnot efficiency, which results in a smaller ideal efficiency. Finally, one can expect a higher pump power consumption in ORCs because of the higher volume flow rate.

A summary of this comparison study between ORCs and Rankine cycle is given in Table 1.1.

From an historical point of view, while ORCs have been actively re-

searched and deployed over the past 40 years, the technology has been used in practice since the early age of heat engines. Early systems using this principle include the *Naphtha Launch*, which was marketed in the 1880's as a means of avoiding regulations pertaining to steam boilers (at the time the U.S. government required a licensed engineer on board vessels with steam boilers). Designers of personal launches developed boats propelled by a Rankine engine boiling naphtha instead of water, the commercial idea being to enable the wealthy to pilot their boats without the assistance of an engineer. Today ORC technology is well developed and more than 250 power plants based on its principle are in use around the world. Five major domains of application can be identified: Biomass, Geothermal, Waste heat recovery and Solar power plants [26].

Concerning this last domain of application, solar energy can be converted directly into electricity (by using commonly available photovoltaic panels) or indirectly via thermal conversion using a heat engine. A standard CSP (concentrating solar power) technology uses collectors and a tracking system in order to concentrate solar rays during sunshine hours. This concentrated beam is then absorbed and used as heat source for a thermodynamic cycle (generally using steam, only a few commercial CSP in the world are based on ORC). Different types of collectors and absorbers have been developed for this application, and these are illustrated in Figures 1.3, 1.4, 1.5 and 1.6. One can distinguish four main technologies:

- **Parabolic dishes** (Figure 1.3) feature point-focus optics and are generally coupled with cavity receivers driving a Stirling engine. This type of configuration yields a high sunlight to electricity conversion efficiency. However, dish systems are unwieldy to scale, have a high engine to aperture area specific cost ratio, and therefore tend to be limited to small scale power generation. An example is the 50kW *Big Dish* plant located in Canberra, Australia.
- **Solar power towers** (Figure 1.4) are point focus systems where the optics consists of a field of heliostats targeting a receiver (various types are employed) mounted on a central tower. This technology achieves the highest temperature among large scale CSP systems and thus presents the opportunity for high conversion efficiency. Moreover, power towers present a better thermal storage capacity which can extend the production time beyond the solar day. Solar power towers are more suitable for large scale power generation and an example of such technology is the 20 MW *PS20* near Sevilla, Spain.
- **Parabolic through collectors**(Figure 1.5) (PTCs) are line focus sys-

tems comprised of linear parabolic mirrors focusing sunlight on an absorber tube placed along the focal line. A single axis tracking system is used to optimize the mirrors position during operation. PTCs are the most widely developed CSP system and it is the technology used in the frame of this project (i.e. the μ -CSP power plant installed in Lesotho by STG International). An early commercial example of PTC power generation is the SEGS CSP plant in California's Mojave desert.

- **Linear Fresnel reflectors** (Figure 1.6) are line focus systems composed of several thin plane mirrors positioned in order to focus solar rays along a tube traveled by a thermal fluid. Flat mirrors are much cheaper and easier to fabricate than parabolic receptors. This technology is suitable for medium to large scale power plants, an example of which is the *PE2* power plant constructed in Murica, Spain.

While solar power in various forms has been employed since antiquity, the first commercialized CSP systems was commissioned in the 1980's. Today the total amount of CSP capacity installed worldwide is estimated at 1.17 GW including both small and large scale power plants [28]. Some examples of such power plants are the 354 MW SEGS (Solar Energy Generating System) in California or one of the eleven 100 MW power plants constructed in Spain. In the framework of this project, the developed scroll expander would be integrated in an approximately $5kW_e$ μ -CSP plant which supplies electricity to remote areas having no access to the grid.

1.3 Description and History of Scroll machines

As described in the previous section, an expansion device is required in order to achieve the conversion of a pressure difference into some mechanical work. Since an ORC uses a low temperature heat source, the related Carnot efficiency, given by

$$\eta_{carnot} = 1 - \frac{T_c}{T_h} \quad (1.1)$$

which represents the maximum ideal efficiency of conversion feasible between the two temperature T_c and T_h , is very low. As discussed in Chapter 6, because any optimization is limited by constraints on the condenser, the evaporator or the workings conditions, it is critical to design for a high expansion efficiency (i.e. as near to isentropic as possible).

Many expansion devices have been developed so far and they can be classified into two main families:

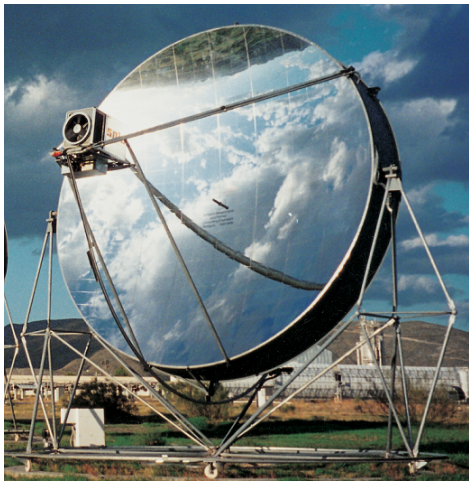


Figure 1.3: Dish Stirling

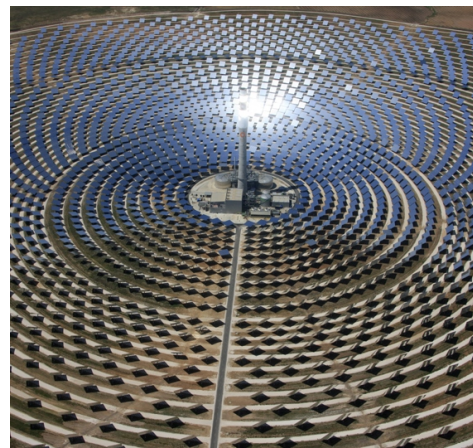


Figure 1.4: Solar Power Tower



Figure 1.5: Parabolic through collectors (PTC)



Figure 1.6: Linear Fresnel collectors

- **Turbomachines** wherein the expansion conversion occurs by an aerodynamic interaction with rotor blades. One can distinguished radial and axial turbines. This kind of expansion device is used primarily in large scale ORC ($\dot{W}_e > 100kW_e$) and regular Rankine power plants.
- **Positive displacement expanders** wherein the expansion conversion occurs by a changing chamber volume process. This type of expansion device is more suitable for ORCs because of their small or medium scale power generation ($\dot{W}_e \in [1 - 100]kW_e$). The main type of technologies found on the market are *piston*, *screw*, *rotary vane*, *gerotor* and *scroll* expanders. Although they are all mature technologies as deployed in compressor applications, most of them are prototypes or in early stages of commercialization for an expander application.

Among the different possibilities aforementioned, the scroll technology has several advantages in comparison with the others which make it a suitable candidate for an ORC application. Historically, the first idea of a scroll machine was proposed in 1905 by the french engineer Léon Creux, but the manufacturing and casting capabilities of the time were not accurate enough to build a workable system. Indeed, tight manufacturing tolerances are required to avoid leakages and ensure an efficient running of the mated scroll elements. With the advent of CNC (*Computer Numerical Control*) manufacturing in the mid 1970's, the scroll machine concept became commercially realizable. Scroll machines were initially designed to work as compressors and are widely employed today in HVAC applications, and also as automobile superchargers and vacuum pumps. Over time the idea to reverse the scroll machine and employ it as an expander began to gain traction within the community of ORC researchers.

A scroll expander is composed of two interleaving *scrolls* having the same shape and indexed 180 degrees with respect to the other so as to allow them to mesh [1]. This relative position creates crescent shaped gas pockets bounded by the involutes and the two base plates of both scrolls. In operation, one scroll remains fixed while the other is attached to an eccentric that drives a generator shaft. As the moving scroll orbits (without rotation) around the fixed scroll, the two small pockets formed by the meshed scrolls at the center follow the spiral outward and enlarge in size. The expander inlet is at the center of the scrolls, where the entering gas is trapped in two opposing gas pockets which then expand as the pockets move toward the periphery, where the discharge port is located. This process is illustrated in Figure 1.7. As explained in [19], scroll machines can be either hermetic, semi-hermetic or open. One can also distinguish compliant and kinematically constrained scroll expanders.

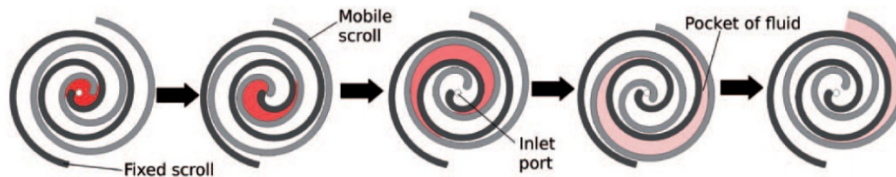


Figure 1.7: Scroll expander principle

Scroll expanders are particularly well suitable for ORC applications due to the following advantages [20]:

- ◇ mechanical simplicity (no valve gear like in a piston machine);
- ◇ low rotational speed;
- ◇ small number of moving parts (on average 70% fewer moving parts than a conventional reciprocating compressors)[2];
- ◇ high reliability and robustness;
- ◇ smooth, continuous and quiet working;
- ◇ the orbiting scroll can be counterbalanced to minimize vibration;
- ◇ high isentropic efficiency;

Besides these advantages, scroll expanders also present some drawbacks. In addition to a complex geometry and a demanding machining process, scrolls expanders require a tight manufacturing tolerance so has to ensure the perfect mesh of the orbiting and fixed scrolls. If this is not achieved, leakages will occur and will dramatically penalize the isentropic efficiency of expansion. Leakages are, with mechanical friction, the primary mode of losses in a scroll machine, heat losses being comparatively small [18]. One can distinguish two main types of leakages as represented on Figure1.8

- **Radial leakages** which occur between the base plate of one scroll and the tip of the other. Radial leakages can be lowered by a tight machining tolerance, a good lubrication or by adding a low friction gasket acting as a tip seal. Manzagol et al. [21] shows experimentally that a $1\ \mu\text{m}$ increase in radial clearance leads on average to a 0.5% loss of isentropic efficiency.
- **Flank leakages** which occur between the inner wall of one scroll and the outer wall of the other. This type of leakage can be minimized

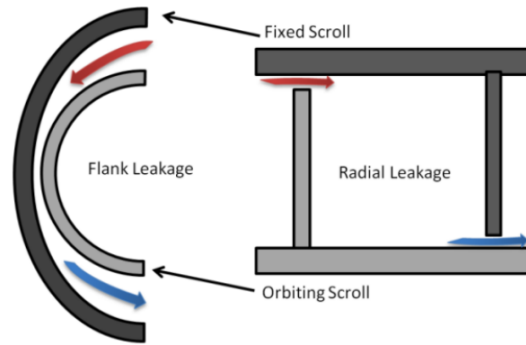


Figure 1.8: Radial and flank leakages occurring in a scroll expander

by maintaining tight tolerances in the scrolls. In the same aforementioned study, Manzagol et al. determines that a $1\ \mu\text{m}$ increase in axial clearance leads on average to a 2.5% loss of isentropic efficiency.

Unlike compressors, expander versions of a scroll machine have yet to be mass produced or substantially commercialized. Two possibilities then exist to obtain a scroll expander. One can adapt a scroll compressor to run in reverse as an expander after some changes in the design as describe by Oralli et al. in [23]. Even if this options is the most commonly used, it has severe drawbacks as explain by Orosz et al. in [25]. Indeed, most scroll compressors have a relatively small intrinsic volume ratio compared to the conditions in an ORC, which limits the operating range (T_{ev} and T_{cond}) or imposes under-expansion conditions, both cases resulting in a drop of the power plant efficiency.

The other option is to design and fabricate a scroll expander with characteristics matched to an ORC application. According to the temperatures and the working fluid selected, the optimal volume ratio required so to maximize power generation may reach values up to 15 or 20. In such case, a single stage design is not feasible and it is required to divide the expansion process by two. As represented in Figure 1.9, one can then put in series two distinct expansion units or can design a two-stage/single-shaft expander. This last option has many advantages over the first one. Since only one generator is used to produce electricity, there is only one output voltage and one signal frequency. Moreover, it also reduces by two the power electronics required which makes the expansion unit simpler and cheaper. On the other hand, a two-stage/single-shaft design has also some drawbacks. Indeed, this architecture is still a prototype, and just few companies (example: *Enertime*) have worked on such a design so far.

Concerning the scroll geometry itself, almost all scroll machines built to date have a constant wall thickness profile. In such a case, scrolls are made

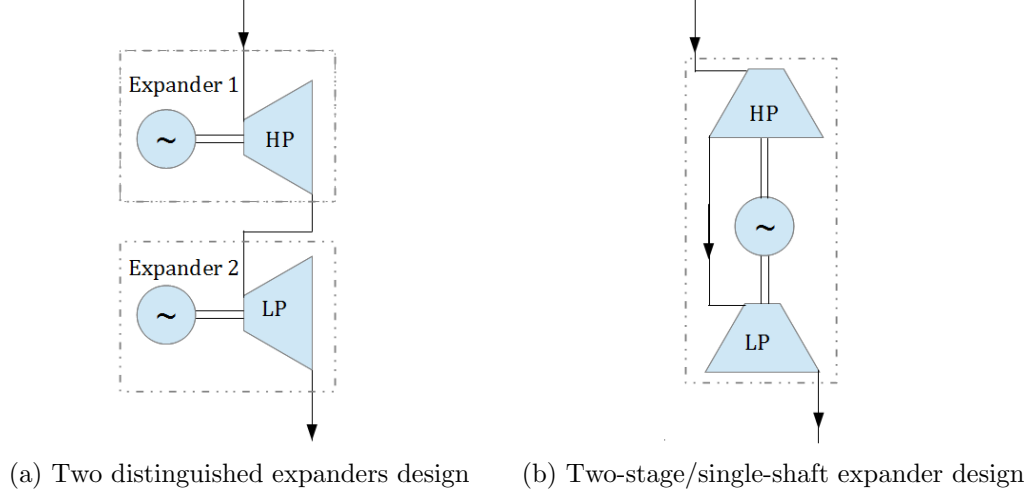
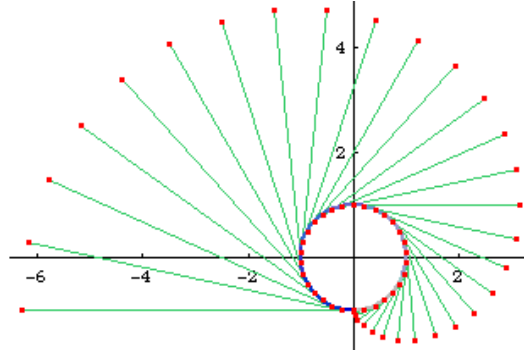


Figure 1.9: Type of possible designs

Figure 1.10: Example of a circle involute aka *Archimedean spiral*

of a pair of *Archimedean spirals*, also called *circle involutes*, separated by a constant distance. Mathematically speaking, an *involute* is a curve obtained by the path followed by an imaginary taut string attached to a given curve (here, a circle), like illustrated in the Figure 1.10. As described by Chen's [7], such a circle involute can be defined using the general mathematical differential equation:

$$\frac{\delta L(\varphi)}{\delta \varphi} = r_b \quad (1.2)$$

where, as shown in Figure 1.11-a, r_b is the circle radius, φ is the involute angle and $L(\varphi)$ is the magnitude of the vector \vec{L} connecting the radius vector tip to the involute. Assuming r_b constant, one can integrate Equation 1.2 and get the following polar expressions describing the pair of involutes for a constant wall thickness scroll geometry

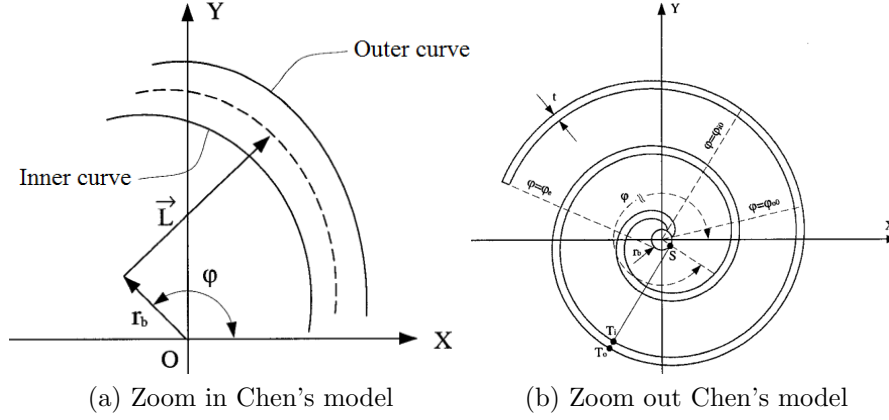


Figure 1.11: Mathematical description of a constant wall thickness scroll geometry

$$L_i(\varphi) = r_b(\varphi - \varphi_{i0}) \quad (1.3)$$

$$L_o(\varphi) = r_b(\varphi - \varphi_{o0}) \quad (1.4)$$

where,

- L_i is the length of the vector \vec{L} for the inner involute
- L_o is the length of the vector \vec{L} for the outer involute
- φ_{i0} is the initial angle for the inner involute
- φ_{o0} is the initial angle for the outer involute

However, in this project we investigate variable wall thickness scroll geometries. This approach is motivated by the fact that a variable wall thickness profile allows an expander to achieve a given volumetric ratio in a more compact device. Indeed, as it will be demonstrated later in this thesis, as the expansion process takes place, the pressure difference between each sides of the scroll decreases along the wrap. It is then possible to reduce the minimum wall thickness required to resist a given deflection of the wall. Doing this, one can thus reduce the overall size of the expansion unit which impacts positively the losses in several ways. For example, reducing the overall wall thickness decreases the contact area between the two scrolls which lowers mechanical friction between them. Moreover, increasing the compactness of the two scrolls reduces the outside surface and thus the ambient heat losses. The hypothesis of a positive effect of the expander compactness has already

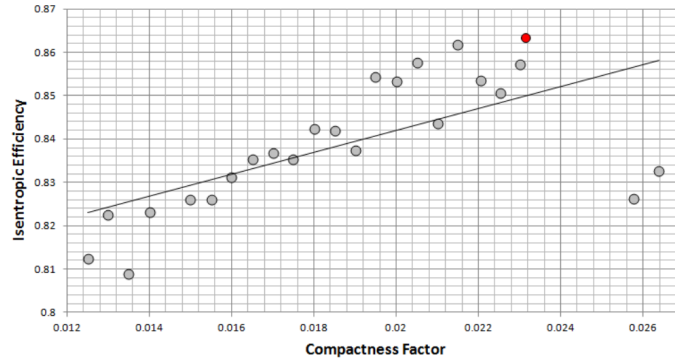


Figure 1.12: Isentropic efficiency as a function of the compactness factor [10]

been proposed by Orosz et. al. [25], whereby the isentropic efficiency of the expander would be linearly proportional to a geometric parameter called the *compactness factor* (see Figure 1.12) defined by

$$CF = \frac{r_v}{D} \quad (1.5)$$

where r_v is the volumetric ratio and D the scroll diameter.

Although no publications could be found describing it in the open literature, some variable wall thickness prototypes have already been developed commercially by HVAC companies. An example is given in Figure 1.13 which is a scroll compressor built by Copeland.

Finally, variable wall thickness geometries are generated using an 8-dimensionnal planar curve frame described by Gravensen and Henriksen [11]. This tool is described in detail in Chapter 3, as well as the strategy to select an optimal scroll geometry.

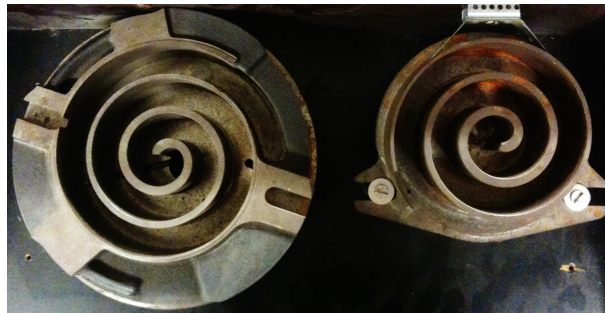


Figure 1.13: Variable wall thickness scroll compressor built by Copeland

1.4 Thesis overview

In concluding this introduction, the contents of this work are briefly described as follows:

- **Chapter 1 - Introduction** - Context and issues are first discussed. Then ORC and scroll machines technologies are described.
- **Chapter 2 - Deterministic modeling of a scroll expander** - A complete description of the deterministic model used to simulate scroll expander performance is given. We then focus on the theory used to model mechanical losses.
- **Chapter 3 - Selection of optimal scroll geometries** - Firstly, the expansion requirement of the prototype in order to meet our production goals is defined. Then we describe the *Danfoss frame* used to generate variable wall thickness geometries and we investigate its parameter domains. Afterwards, minimum wall thickness requirements are clearly described and the overall selection process strategy is explained. Finally, results for the first and second expansion stage are presented.
- **Chapter 4 - Prototype architecture and CAD modeling** - This chapter depicts the single stage prototype architecture and describes its main components. A brief note about 3D-printing and CAM is then presented. Finally, a draft overview of the two-stages/single-shaft prototype is given.
- **Chapter 5 - Manufacturing of a single stage prototype** - In this chapter, we present the practical side of the project. First, interesting elements of manufacturing theory are discussed, then an overview of the performed operations is given with some pictures of the assembled prototype.
- **Chapter 6 - MicroCSP** - This chapter describes the μ -CSP plant for which the scroll expander is developed. Then, a model of the power plant performance as a function of different parameters is carried out in order to demonstrate effect of increasing the expander efficiency and the built-in volume ratio.
- **Chapter 7 - Conclusion** - The thesis is concluded with a summary of major results of this project.

Chapter 2

Deterministic modeling of a scroll expander

Modeling is an important step in a design process. Its goal is to investigate the performance of a system in different operating conditions without requiring many time-consuming and expensive experiments.

In this work, two main categories of models will be distinguished: *semi-empirical* and *deterministic* models. Semi-empirical models are based on lumped parameters identified from experimental data in order to model a system while extrapolating to other operating conditions. An example of semi-empirical scroll expander model is the one published by Lemort [18] as illustrated in Figure 2.1.

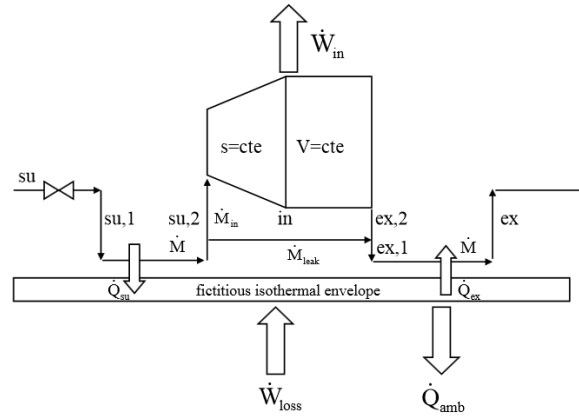


Figure 2.1: Lemort's semi-empirical model of a scroll expander

In this model, the expansion process is divided into a first isentropic expansion followed by an isochoric process. Moreover, the model accounts for the pressure drop at the inlet, heat exchange with the ambiance, leakages, mechanical losses of the expander itself and finally electromechanical

losses in the generator. Although much less computationally intensive, a semi-empirical model also presents severe drawbacks. Firstly, one requires experimental data to define the model parameters. Moreover, these parameters are often only viable within a limited range of operating conditions. Finally, such kind of model cannot be used to investigate the influence of geometrical parameters on the performance. Precisely, in the frame of this project, we cannot use a semi-empirical model to study the influence of scroll geometries on the expansion efficiency. To achieve this, one needs to use a *deterministic* model.

A deterministic model simulates in detail the most relevant physical phenomena occurring in the system. Ideally, it does not require any empirical parameters, although in practice this will rarely be the case since situations with complex fluid dynamics, heat transfer, lubrication and kinematic machinery tend to involved models with empirical coefficients. The initial deterministic model described in this chapter is based on Dechesne's work [10] which was based on a scroll compressor model developed by Legros (University of Liège). As shown in Figure 2.2, the model is divided in two parts modeling respectively the geometric features and the thermodynamic variables during the expansion. Whereas this initial work did not account for all the mechanical losses generated in a scroll expander, the present work has this and other pertinent aspects. A full description of this topic can be found in section 2.3 (page 41).

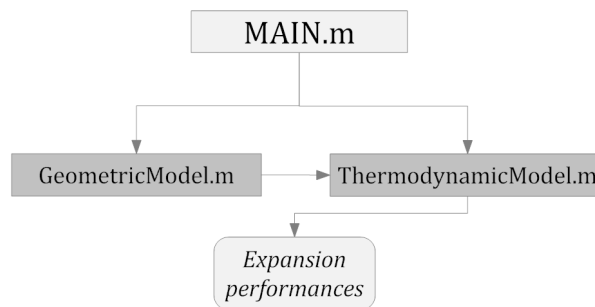


Figure 2.2: Deterministic model overview

2.1 Geometric model overview

The scroll models discussed in this work are coded and implemented in Matlab, following a hopefully intuitive naming convention. The first code run by the top level program *MAIN.m* in the course of simulating the scroll expander performance is *GeometricModel.m*. Its aim is to compute all the geometrical

data required by the thermodynamical model (see next section). *Geometric-Model.m* and all the other sub-codes presented here below are provided in an attached data CD¹.

The geometric model is based on different parameters described as follows:

- the target inlet area required to scale the scroll geometry in order to meet the volume inlet requirement. It is defined as $A_{in*} = \frac{V_{in}}{h}$ where V_{in} and h are the inlet volume and the scroll height.
- the 8 parameters required by the the Danfoss frame in order to generate a variable wall thickness scroll geometry. For more information on this tool, refer to section Chapter 3.
- the curves resolution n defining the number of points composing each scroll wrap. It is fixed to 5000 as a trade-off between computational effort and geometrical accuracy.
- the number of angular steps *num_ang_step* used to discretize the whole revolution of the orbiting scroll. This parameter highly influences the simulation time of the geometric code. For example, running the *GeometricModel.m* with $n = 5000$ takes 190 sec if *num_ang_step* = 200 and 15 min if *num_ang_step* = 1000. Furthermore, once *num_ang_step* is defined, one can compute the step angle $\Delta\theta$ between each discretized crank angle i.e.

$$\Delta\theta = \frac{2\pi}{num_ang_step} \quad (2.1)$$

From these inputs, *my_scroll_optim.m* provides the Cartesian coordinates of the two scrolls using the theory described in [11]. Then, the positions of all conjugacy points for each crank angle θ_i are computed with *calc_conj_index.m*. Other important data such as number of expansion pockets N_{exp} ², the discharge angle θ_d and the related index N_d are also computed i.e.

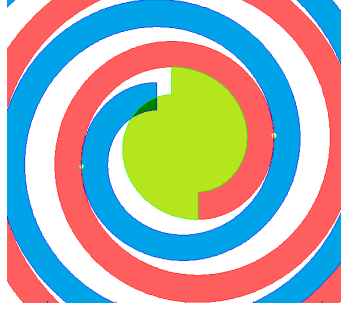
$$N_{exp} = floor(N - 1) \quad (2.2)$$

$$\theta_d = 2\pi(N - floor(N)) \quad (2.3)$$

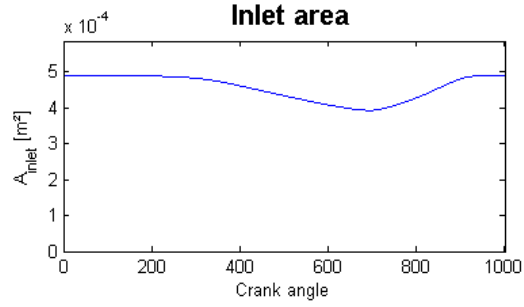
$$N_d = round(frac\theta_d\Delta\theta) \quad (2.4)$$

¹this chapter gives only an overview of the different codes, anyone interested in more details about them is invited to read Dechesne's thesis [10] or contact this author.

²At the beginning of the revolution, there is thus one inlet pocket (pocket #1), N_{exp} expansion pockets (pockets #2 to $\#N_{exp} + 1$) and one exhaust pocket ($\#N_{exp} + 2$). At the discharge angle θ_d however, the last expansion chamber disappears and only $N_{exp} + 1$ chambers remain. In the model, all parameters related to the chamber $\#N_{exp} + 1$ are set to zero as soon $N > N_d$



(a) Optimized inlet port while overlapped by the orbiting scroll



(b) Inlet area in function of the crank angle θ

Figure 2.3: Inlet port

The radial and flank gap values are derived from Manzagol et al. [21] and set to 10 and $20\mu\text{m}$ for the radial and the flank gaps respectively.

Following this initial step, a loop computes all the required geometrical features for each crank angle of the discretized revolution. As the relative position of the orbiting scroll is changed to the next crank angle the following data is computed:

- **Inlet area** - In order to decrease throttling losses during the intake process, the inlet port is designed in order to maximize its surface area. We thus exploit the entire surface area available between the two scrolls as illustrated in green in Figure 2.3a. Nevertheless, for some crank angles, the orbiting scroll overlaps the inlet port resulting in a decrease of the actual inlet area (see Figure 2.3a). As a consequence, the inlet area is not constant and its evolution is computed as a function of the crank angle as shown in in Figure 2.3b.
- **Outlet area** - The exhaust process when the last expansion chamber ($\#N_{exp+2}$) opens to the exhaust is modeled as a flow through a nozzle. The nozzle surface area is made equal to the outlet port area defined as the scroll height times the distance k between the two mating sides at the end of the scroll (see Figure 6.10a). As with the inlet, the outlet port area is not constant because of the relative motion of the orbiting scroll as depicted in Figure 6.10b.
- **Leakages area**- As previously explained, two types of leakages, aka *radial* and *flank* leakages, occur in a scroll expander. Flank leakage surface area remains constant during the complete orbit and is given by

$$A_{flank} = G_f \cdot h \quad (2.5)$$

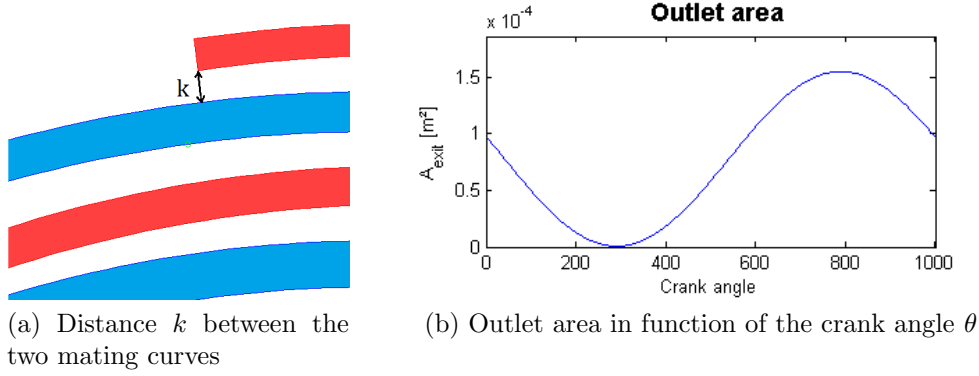


Figure 2.4: Exhaust port

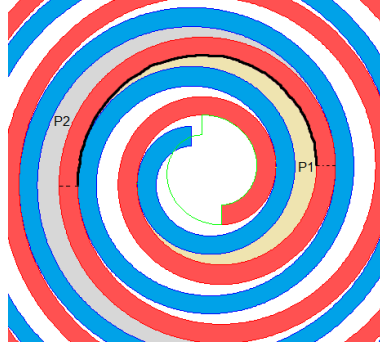


Figure 2.5: Leakage length between one pair of P1 and P2

where G_f is the flank gap (set to $20\mu\text{m}$ in accordance with [21]) and h is the scroll height. On the other hand, the radial leakage surface area is given by

$$A_{\text{radial}} = G_r \cdot L_r \quad (2.6)$$

where G_r is the radial gap (equal to $10\mu\text{m}$ in accordance with [21]) and L_r is the leakage length between two adjacent pockets (e.g. P1 and P2 as represented in grey and orange in Figure 2.5). This leakage length is defined as the length of the inner side of the scroll part seen by both P1 and P2. An example is given in Figure 2.5 in which the leakage length between P1 and P2 is drawn in black. Finally, one has to keep in mind that each expansion pocket is twinned (i.e. duplicated symmetrically within the scroll), therefore the actual leakage length must be multiplied by two as well.

- **Pockets volume and volume derivative** - Pockets volume is computed by the pocket's area times the scroll height. Pocket area is obtained using the Matlab function *polyarea* which computes the area

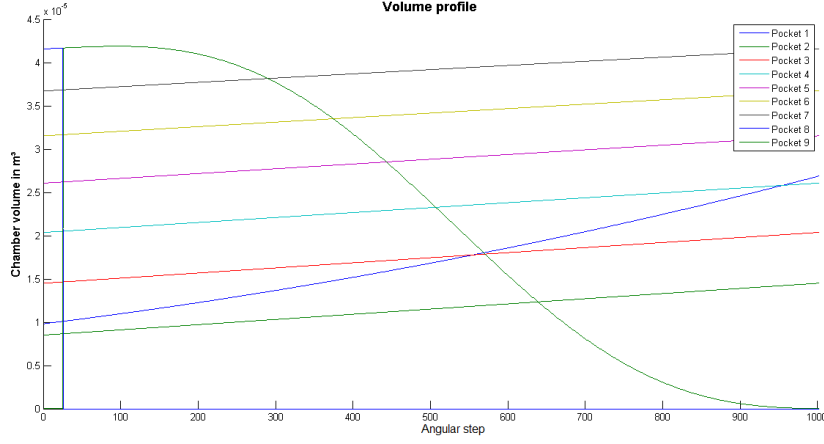


Figure 2.6: Evolution of pocket volume as a function of the crank angle

enclosed by different curves. An example of pockets volume profile in function of the crank angle for one scroll geometry is given in Figure 2.6. Finally, volume first derivative is approximated using the *five points formula* i.e.

$$V'(\theta) = \frac{V(\theta - 2\Delta\theta) - 8V(\theta - \Delta\theta) + 8V(\theta + \Delta\theta) - V(\theta + 2\Delta\theta)}{12\Delta\theta} \quad (2.7)$$

However, Equation 2.7 is not valid for the beginning and the end of the volume vector V . Hence, forward and backward derivative approximations are required, as detailed in [10].

Once the loop is completed and all these features are known for every crank angle, the results are saved in a 'Geometric.mat' file to be used later when running the thermodynamic code.

2.2 Thermodynamic model overview

Having defined the relevant geometrical features, the goal of the thermodynamic model is to compute the expander performance by simulating all the thermodynamic variables in each chamber and at each crank angle. This model takes into account the main phenomena occurring during the expansion process i.e.

- flank and radial leakages
- friction between the two scrolls

- a possible over or under-expansion if the volumetric ratio of the expander does not match the operating conditions [18]
- mechanical losses in the journal and the thrust bearings
- heat losses from the system

The next section describes the modeling paradigm and some details about the way to model the different mass flows. Mechanical losses models are investigated in a distinct section because they have been a main research topic in this thesis.

2.2.1 Modeling principle

The initial step while running *ThermodynamicModel.m* is to define the operating conditions such as the working fluid as well as the inlet/outlet temperatures and pressures. Following this, *ThermodynamicModel.m* runs the code *ThermoExpanderNozzle.m* in order to simulate the main thermodynamic variables (P , T , h and s) in each pocket at each crank angle. This code starts by setting initial values of the pressure and the entropy of each chamber at the first crank angle ($\theta = 0$). Hence, the entropy is assumed to be the same in each pocket (perfect expansion) and the pressure profile decreasing linearly. Afterwards, *ThermoExpanderNozzle.m* starts to model a full revolution. Its general principle can be described as follow: once all the thermodynamic variables in the expander are known for a crank angle θ_i , we evaluate the mass and the internal energy variations in each chamber i.e.

$$\frac{dM}{d\theta} = \frac{1}{\omega} \left(\sum_i \dot{M}_{in,i} - \sum_j \dot{M}_{out,j} \right) \quad (2.8)$$

$$\frac{dU}{d\theta} = \frac{\dot{Q}}{\omega} - P \frac{dV}{d\theta} + \frac{1}{\omega} \left(\sum_i \dot{M}_{in,i} \cdot h_{in,i} - \sum_j \dot{M}_{out,j} \cdot h_{out,j} \right) \quad (2.9)$$

where ω is the shaft speed expressed in rad/s , $\dot{M}_{in,i}$ and $\dot{M}_{out,j}$ are any flows going in and out of the studied pocket, $h_{in,i}$ and $h_{out,j}$ are their corresponding enthalpies and, finally, \dot{Q} is the resulting heat exchange of the pocket with its environment³.

Equations 2.8 and 2.9 are then used to compute the internal energy U and the working fluid mass M in each pocket for the next crank angle θ_{i+1} .

³but this loss is not taken into account in this model, $\dot{Q} = 0$ in all cases

From these values, and knowing V from the geometric code, we compute the specific volume v and the specific internal energy u for all chambers i.e.

$$U_{pocketj,\theta=\theta_{i+1}} = U_{pocketj,\theta=\theta_i} + \frac{dU}{d\theta}_{pocketj,\theta=\theta_i} \Delta\theta \quad (2.10)$$

$$M_{pocketj,\theta=\theta_{i+1}} = M_{pocketj,\theta=\theta_i} + \frac{dM}{d\theta}_{pocketj,\theta=\theta_i} \Delta\theta \quad (2.11)$$

$$u_{pocketj,\theta=\theta_{i+1}} = \frac{U_{pocketj,\theta=\theta_{i+1}}}{M_{pocketj,\theta=\theta_{i+1}}} \quad (2.12)$$

$$v_{pocketj,\theta=\theta_{i+1}} = \frac{V_{pocketj,\theta=\theta_{i+1}}}{M_{pocketj,\theta=\theta_{i+1}}} \quad (2.13)$$

From u and v , one can finally determine all the other thermodynamic variables for the new crank angle θ_{i+1} using the thermodynamic library *refprop*. This process is then repeated for every crank angle until the whole revolution is modeled.

At the end of the round ($\theta = 2\pi$), a convergence test based on the the outlet temperature is executed to check that steady-state conditions have been reached. Convergence is defined as the outlet temperatures between two consecutive iterations approaching within 0.01°C , i.e.:

$$|T_{ex,it=i} - T_{ex,it=i-1}| \leq 0.01^\circ\text{C} \quad (2.14)$$

At which point, the function *ThermoExpanderNozzle.m* exits and *ThermodynamicalModel.m* computes the expander performance: the mechanical and thermal losses, the generated power \dot{W} , the isentropic efficiency η_{is} , the filling factor FF [26], etc. These three last parameters defined as:

$$\eta_{is} = \frac{\dot{W}}{\dot{W}_{is}} = \frac{\dot{M}(h_{su} - h_{ex}) - \dot{W}_{loss} - \dot{Q}_{amb}}{\dot{M}(h_{su} - h_{ex,is})} \quad (2.15)$$

$$FF = \frac{\dot{V}_{mes}}{\dot{V}_{th}} \quad (2.16)$$

On the other hand, if the outlet temperature does not satisfy Equation 2.14, a new iteration to model the whole revolution begins with new initial values for the pressure and the entropy of each pocket. In particular, the pressure and the entropy of a pocket j are set to the last value of the

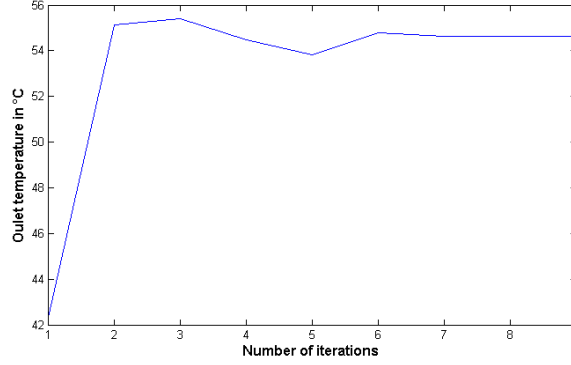


Figure 2.7: Outlet temperature convergence

pocket $j - 1$ found at the previous iteration i.e.

$$P_{(pocket1,\theta=0,iteration=i+1)} = P_{su} \quad (2.17)$$

$$S_{(pocket1,\theta=0,iteration=i+1)} = S_{su} \quad (2.18)$$

$$P_{(pocketj,\theta=0,iteration=i+1)} = P_{(pocketj-1,\theta=2\pi,iteration=i)} \quad (2.19)$$

$$S_{(pocketj,\theta=0,iteration=i+1)} = S_{(pocketj-1,\theta=2\pi,iteration=i)} \quad (2.20)$$

$$P_{(pocketN_{exp}+2,\theta=0,iteration=i+1)} = P_{(pocketN_{exp}+2,\theta=2\pi,iteration=i)} \quad (2.21)$$

$$S_{(pocketN_{exp}+2,\theta=0,iteration=i+1)} = S_{(pocketN_{exp}+2,\theta=2\pi,iteration=i)} \quad (2.22)$$

The number of iterations required to achieve the convergence depends on the scroll geometry and the operating conditions but it is generally close to ten. An example of the convergence curve is given in Figure 2.7 showing the outlet temperatures obtained as a function of the number of iterations.

Finally, the overall code architecture is represented in Figure 2.8.

2.2.2 Mass flows

Inlet, exhaust and flank leakage flows

Intake, exhaust and flank leakage flows are all modeled as a flow through a nozzle [18]. In this case, mass flow is dictated by the following equations:

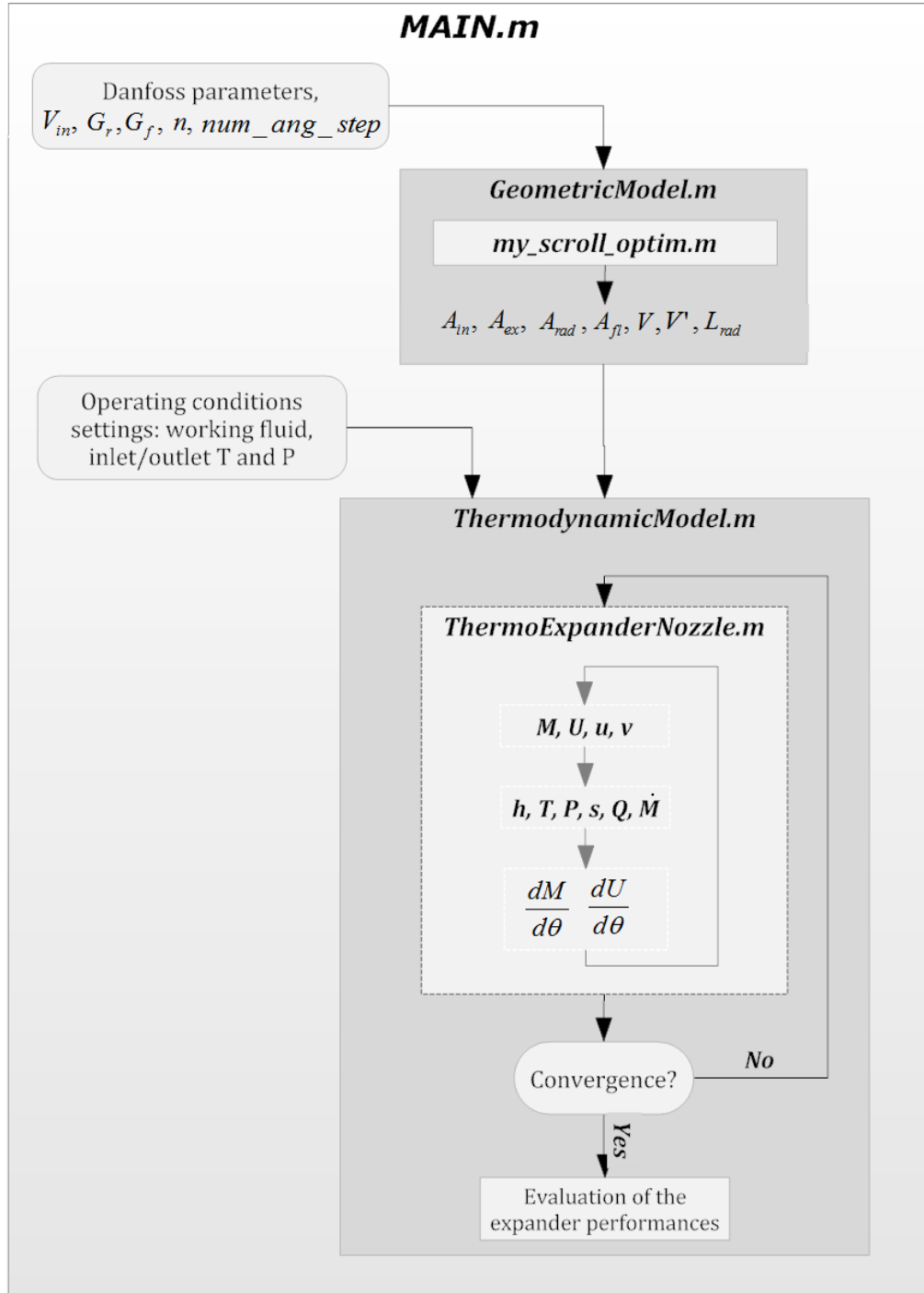


Figure 2.8: Overall model architecture

$$\dot{M} = A_n \sqrt{\frac{2P_h}{v_h}} \sqrt{\frac{\gamma}{\gamma-1} \left[\left(\frac{P_l}{P_h} \right)^{\frac{2}{\gamma}} - \left(\frac{P_l}{P_h} \right)^{\frac{\gamma+1}{\gamma}} \right]} \quad \text{if } P_l > P_{crit} \quad (2.23)$$

$$\dot{M} = A_n \sqrt{\frac{2P_h}{v_h}} \frac{\gamma}{\gamma+1} \frac{2\gamma}{\gamma+1} \frac{1}{\gamma-1} \quad \text{if } P_l < P_{crit} \quad (2.24)$$

$$P_{crit} = P_h \left(\frac{2}{\gamma+1} \right)^{\frac{\gamma}{\gamma-1}} \quad (2.25)$$

where A_n is the nozzle area, P_h is the upper pressure, P_l is the lower pressure, γ is the heat capacity ratio, P_{crit} is the critical pressure and v_h is the specific volume of the fluid at the high pressure P_h . Equation 2.23 is used in case of a regular flow whereas Equation 2.24 describes a choked flow.

Radial leakages

Radial leakages, however, are not modeled with a nozzle theory. According to [10], it has been shown experimentally that a *frictional mass flow* model is more suitable. In such a case, the mass flow is dictated by the following equations:

$$Re = \frac{\rho U D_h}{\mu} \quad (2.26)$$

$$f = \frac{64}{Re} \quad \text{if } Re < 1037.88 \quad (2.27)$$

$$f = 0.35 Re^{-0.25} \quad \text{if } Re \gg 1037.88 \quad (2.28)$$

$$\dot{M} = A_{rad} \sqrt{\frac{2D_h \rho \Delta P}{f t_{rad}}} \quad (2.29)$$

where Re is the Reynolds number, D_h the hydraulic diameter, U the flow velocity, μ the dynamic viscosity, f the friction coefficient, \dot{M} the mass flow, A_{rad} the radial leakage area, t_{rad} the scroll thickness, ρ the fluid density and, finally, ΔP is the pressure difference.

The hydraulic diameter is given by the theory of fluid mechanics i.e. $D_h = (4A_{rad})/P_{rad}$ where P_{rad} is the *wetted diameter* of the flow cross section. In our particular case, one can reformulate

$$P_{rad} = 2(G_r + L_r) \quad (2.30)$$

where G_r and L_r are the radial gap and leakage length computed in the geometric model.

2.3 Mechanical losses

As explained in [18] (and confirmed in Tables 3.3 and 3.5), mechanical losses and leakages are the main sources of reduction in isentropic efficiency in a scroll expander, aside from any under/over-expansion. Leakages were already modeled in the initial code whereas mechanical losses were partially taken into account. Hence, the main investigation topic of this thesis is the improvement of mechanical losses models in the thermodynamic code. Firstly, this section describes each type of mechanical loss and the theory used to model it in a deterministic way. Then, a sensitivity analysis is conducted to investigate the influence of various parameters on the simulation results.

2.3.1 Friction between the scrolls

The first kind of mechanical losses is due to friction between the two scroll wraps (where the radial leakages occur). Assuming that the gap between the tip and the plate of the two mating scrolls is full of oil and refrigerant, we model this loss as a lubricated friction and the friction force F_{fric} is given by the equation proposed by Caillac et al. [6] i.e.:

$$F_{fric} = \frac{V\mu A_{fric}}{G_{rad}} \quad (2.31)$$

where $V = \omega R^*$ is the linear speed between the two scrolls, A_{fric} is the total contact area (two times the scroll surface area), G_{rad} is the radial gap (set to $10\mu m$ [21]) and μ is the dynamic viscosity of the mixture oil-refrigerant between the two scrolls. Friction losses are finally given by

$$\dot{W}_{fric} = VF_{fric} = \frac{V^2\mu A_{fric}}{G_{rad}} \quad (2.32)$$

Further information about μ and the oil fraction in the oil-refrigerant mixture are provided in section 2.3.4 (pages 45).

2.3.2 Journal bearing losses

A journal bearing is a mechanical device composed of a simple supporting sleeve in which a shaft can rotate freely. In operation, an oil film of variable thickness is created and acts as a separation, preventing thereby any direct contact between the shaft and the bearing inside surface. Unlike ball bearings, it does not contain any rolling element. Mechanical losses in journal bearings depend on the type of lubrication for which we distinguish the cases

of dry lubrication (with a metal-metal contact) and hydrodynamic lubrication (without a metal-metal contact). In the frame of this work, we assume that only the second case occurs. Hence, mechanical losses are only due to friction shear in the oil film.

As explained in *Hydrodynamic Lubrication* [14], in order to calculate exactly the friction losses inside a journal bearing, one has to determine the exact pressure field in the bearing and thus solve the Reynolds equation i.e.

$$\frac{\partial}{\partial x}(h^3 \frac{\partial p}{\partial x}) + \frac{\partial}{\partial z}(h^3 \frac{\partial p}{\partial z}) = 6\mu U \frac{\partial h}{\partial x} \quad (2.33)$$

where $p(x, z)$ is the oil film pressure, $h(x, z)$ is the oil film thickness and U is the circumferential velocity of the journal. Finding an analytical solution for the Equation 2.33 is a challenge that has interested many investigators [13]. One of the most salient results is the one proposed by Sommerfeld which states that the generic expression of the solution might be written as:

$$\frac{r}{c}f = \Phi[(\frac{r}{c})^2 \frac{\mu N}{P}] \quad (2.34)$$

where r is the shaft radius, c is the radial clearance⁴, f is the losses coefficient, N is the shaft speed and P is the radial pressure acting on the bearing. The term in brackets is known as the *Sommerfeld number* S , or *bearing characteristic number*. It is a dimensionless quantity used in lubrication analysis and which contains all the parameters influencing the bearing behavior.

Furthermore, solving Equation 2.33 is impractical in this situation since the radial force is not static (see Figure 2.10) and this complex equation should be solved for every crank angle θ . Instead of this, we use the Vogenhols law in order to model mechanical losses in the journal bearings. This law is based on the results obtained when solving the Reynolds equation for two extreme cases: when $S \rightarrow 0$ and when $S \rightarrow \infty$. A complete description of the mathematical development of this solution can be found in [9]. The final expression is

$$f \frac{r}{c} = \begin{cases} \pi(2\pi S), & \text{if } 2\pi S \geq 1 \\ \pi\sqrt{2\pi S}, & \text{if } 2\pi S < 1 \end{cases} \quad (2.35)$$

giving the loss coefficient f . This coefficient can then be used to compute the friction force and finally the loss power, i.e.:

$$F_{loss,JB} = f.F_{rad} \quad (2.36)$$

$$\dot{W}_{loss,JB} = F_{loss,JB}.r.\omega \quad (2.37)$$

⁴see Chapter 5 for more information about its selection

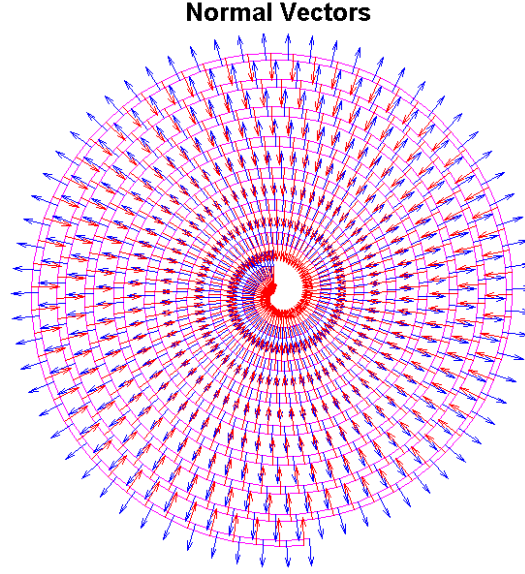


Figure 2.9: Normal vector along the orbiting scroll

where F_{rad} is the radial load on the bearing, $F_{loss,JB}$ is the loss force, r is the journal radius, ω is the shaft speed in rad/s and, finally, $\dot{W}_{loss,JB}$ is the power lost in the bearing.

As shown in Equation 2.36, an important parameter to determine in order to compute the mechanical losses in a journal bearing is the resulting radial force acting on it. By neglecting centrifugal forces due to any imbalance, the resulting radial load is due to the asymmetry of pressure applied on the orbiting scroll [5], evaluated as follows. First the normal vector coordinates of each point along the orbiting scroll are computed, as represented in Figure 2.9. This is realized in the geometric model by the four Matlab functions *Norm_1o.m*, *Norm_1i.m*, *Norm_2o.m* and *Norm_2i.m*. Afterwards in the thermodynamic model, once *ThermoExpanderNozzle.m* completes the expansion simulation, the Matlab function *resulting_force.mat* is run to compute the resulting force acting in each pocket and on both sides of the orbiting scroll. These forces are then summed to find the resulting force acting on the orbiting scroll at a given crank angle θ . As shown in Figure 2.10, the result is a rotating force which follows the orbiting scroll position, and its magnitude (in blue) oscillates around a mean value (in red). To simplify the model, this mean value is used in Equation 2.36.

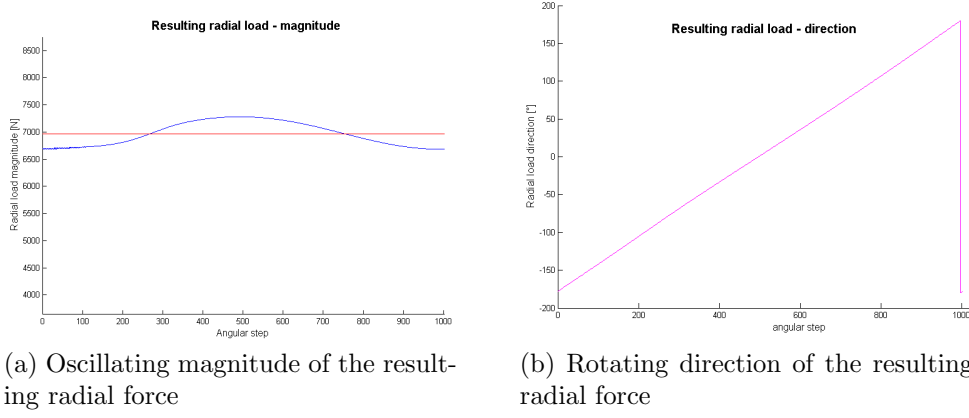


Figure 2.10: Resulting radial force - magnitude and direction

2.3.3 Thrust bearing losses

In contrast with journal bearings, a thrust bearing is a mechanical device designed to support axial loads acting on a rotating surface. In the case of a *fluid thrust bearing*, the axial load is supported by a thin oil film that prevents any direct contact between the two surfaces. Assuming the oil film thickness is uniform, we can model the lubricated friction losses in the thrust bearing with the same relations previously described, i.e.:

$$\dot{W}_{TB} = V F_{TB} = \frac{V^2 \mu A_{TB}}{G_{TB}} \quad (2.38)$$

where $V = \omega R^*$ is the orbitation speed of the moving scroll, A_{TB} is the thrust bearing contact area, G_{TB} is the oil film thickness and μ is the dynamic viscosity of the mixture oil-refrigerant under the thrust bearing.

In the frame of this work, the oil film thickness is assumed to be constant for all scroll geometries. To justify this assumption, we update the thrust bearing area A_{TB} as a function of the axial load which depends of the scroll geometry itself. The resulting axial load acting on the thrust bearing is given by the sum of the orbiting scroll weight and the resulting axial force of expansion computed by the thermodynamic model, i.e.:

$$F_{axial} = W_{weight, scl} + F_{ax, load} \quad (2.39)$$

The thrust bearing area is then determined by a linear interpolation, i.e.:

$$A_{TB} = \alpha F_{axial} + \beta \quad (2.40)$$

where α and β are two empirical parameters derived from measurement on two Copeland scroll compressors⁵. Keeping the inner diameter of the thrust

⁵See the Matlab code *LinearInterpolationThrustArea.m* for more details

bearing constant for every geometry, the outside diameter is finally calculated easily.

Regarding the oil film thickness itself, its value is difficult to evaluate exactly. According to the *Machinery's Handbook* [22], the oil film thickness for this kind of application is within 5 and 50 μm . The value chosen for the thermodynamic model, 15 μm , is issued from a sensitivity study presented in the next section.

2.3.4 Sensitivity study

A major drawback of deterministic models is the necessity to know accurately each parameter influencing the investigated phenomenon. In this study, three key inputs of the above models are unknown:

- the oil film thickness supporting the thrust bearing;
- the oil fraction in the refrigerant-oil mixture in the different bearings;
- the oil fraction in the refrigerant-oil mixture between the two scrolls;

Specifically, the three unknown variables involve tribological aspects of the machinery in operation.

Whereas references [22] provide some guidance as to the thrust bearing film thickness,⁶ no information could be obtained regarding the oil fraction. A theoretical study based on oil solubility in the refrigerant cannot be realized since this information (i.e. a Daniels plot) does not exist in the open literature for R245fa and any POE (polyolester oil) at the temperatures and pressures found in a scroll expander. Furthermore, variations in local pressure and temperature in the different bearings could influence the oil solubility, and modeling these would entail a considerable effort using e.g. CFD (Computational Fluid Dynamics) tools. Confronted with these challenges, an alternative approach is to conduct a sensitivity study in order to quantify the influence of these unknown parameters on the expansion efficiency η_{is} . The goal of this analysis is to select values for each unknown parameter which minimize the error in computing the modeled isentropic efficiency.

Towards this goal, a 3D-map of the expansion isentropic efficiency is generated as a function of the oil film thickness and the oil fraction (considered initially equal everywhere). The thickness range is chosen to be [5 - 50] μm in accordance with [22]. An initial wide range for the oil fraction x_{oil} (from 50% to 100%) is investigated, and the mixture viscosity is computed as a

⁶For such type of application, the thickness should be within 5 and 50 μm

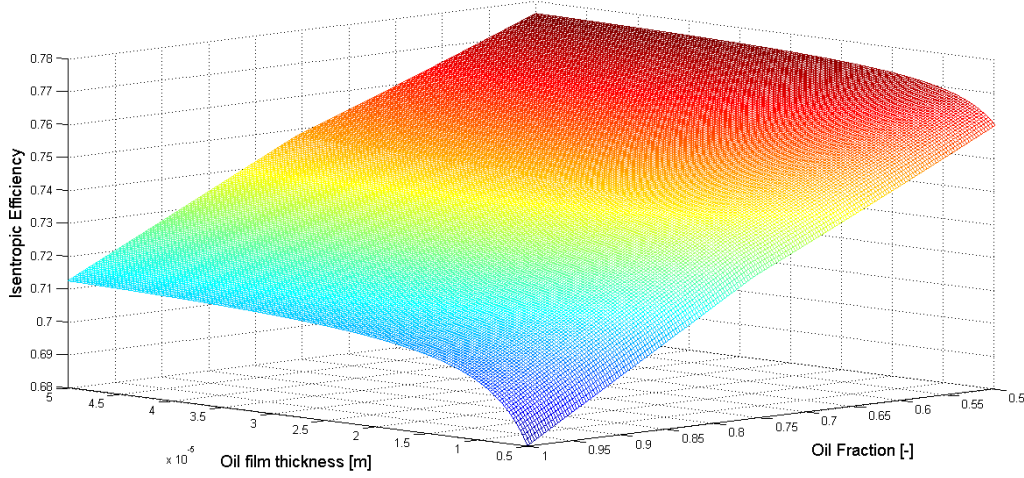


Figure 2.11: Isentropic efficiency in function of the oil film thickness ($[5 - 50]\mu\text{m}$) and the oil fraction ($[50 - 100]\%$)

linear combination of the refrigerant and the oil viscosity,⁷ i.e.:

$$\mu_{mix} = x_{oil} \mu_{oil} + (1 - x_{oil})\mu_{ref} \quad (2.41)$$

The mapping is obtained by running the Matlab function *LossesParametersStudy.m* and the result is shown in Figure 2.11. As expected, the smaller the oil fraction or the thicker the oil film height, the better the expansion efficiency. The two extremes are 68.01 and 77.61% in the worst and the best cases. It is also evident that the impact of film thickness drops off beyond $20\mu\text{m}$. The average difference of efficiency $\Delta\eta_{is}$ between a film thickness of 5 and $50\mu\text{m}$ is around 3.5%. Hence, to split the difference an oil film thickness of $15\mu\text{m}$ is selected. In this case, the largest possible error that can be applied to isentropic efficiency due to an uncertainty in this parameter should be less than 2%.

Furthermore, it is assumed that the oil fraction is not the same in the bearings as it is between the two scrolls, in which case the same mapping exercise can be performed to investigate the effect of oil fraction on the expansion efficiency. Supposing that the oil fraction between the two scrolls $x_{oil,scl}$ is smaller than in the bearings $x_{oil,bcl}$, their ranges are set to $[30 - 70]\%$ and $[70 - 90]\%$ respectively. The resulting mapping is given in Figure 2.12. One can observe that the oil fraction in the bearings has more effect on the isentropic efficiency than the oil fraction between the two scrolls. Indeed, the efficiency difference $\Delta\eta_{is}$ between $x_{oil,scl,min}$ and $x_{oil,scl,max}$ is only equal to 0.6

⁷ $\mu_{oil}(T)$ and $\rho_{oil}(T)$ for the *Emkarate RL 100 POE* are taken from [10]

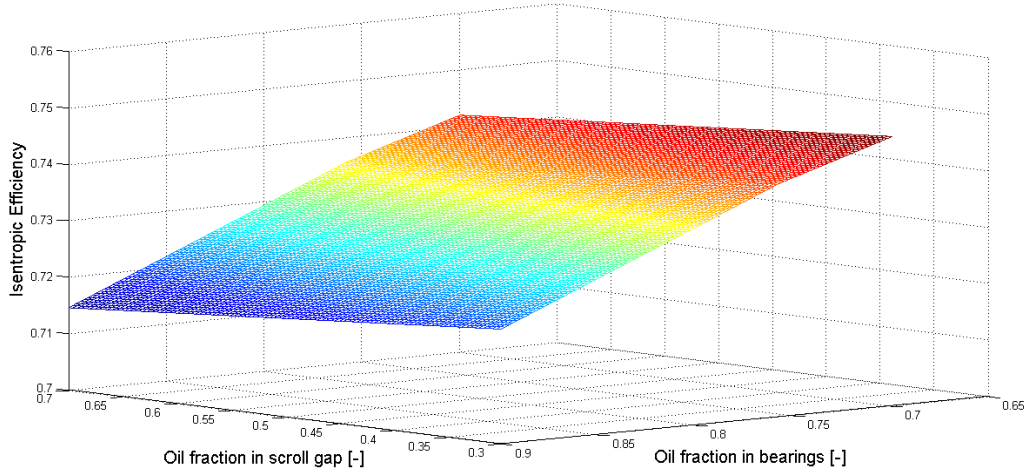


Figure 2.12: Isentropic efficiency in function of the oil film thickness ($[5 - 50]\mu m$) and the oil fraction ($[50 - 100]\%$)

% on average, whereas it is 2.7% between the two limits of $x_{oil,bearing}$. Keeping the same strategy as before, values are chosen that split the differences. The final oil fractions selected are thus 85% and 55% for $x_{oil,scl}$ and $x_{oil,scl}$ respectively.

Chapter 3

Selection of optimal scroll geometries

This chapter describes the selection process used to find the optimal scroll geometries for the two-stage expander prototype. We first define the expansion requirements so as to meet our electric production expectations. Afterwards, we give a description of the Danfoss framework (and its domain science) used to generate different scroll geometries. Finally, an overview of the codes employed and the obtained results is provided.

3.1 Operating condition requirements

So as to define the requirements that the expander must meet (mass flow, volume ratios, etc.), a simple steady state model of the double expansions process is developed with Engineering Equation Solver (code in appendix). The evaporating and condensing temperatures are imposed by the ORC test rig and we assume an expansion isentropic efficiency of 72%. The shaft speed is chosen to be 3000 *rpm* since it corresponds to the 50 Hz grid frequency of an induction generator with one pair of poles. Moreover, as shown in [10], this speed range corresponds well with the optimal trade off between leakages and friction losses for the type of scroll machine. A gross power production of 5kW is proposed, divided equally between the two stages since they are placed on a same shaft. It should be noted that other criteria could have been selected, such as imposing scroll geometries producing equal axial loads. However, such a condition would have required substantial computational effort by running the thermodynamic program for every geometry so as to check viability. Imposing equivalent power production for both stages is a simple and straightforward criteria which defines the volume ratios within the steady state model.

Input conditions			Results		
T_{ev}	=	135 °C	\dot{m}	=	0.1508 kg.s ⁻¹
T_{cond}	=	35 °C	P_{su}	=	2568 kPa
η_{ex}	=	72 %	P_{int}	=	694.4 kPa
\dot{W}_{tot}	=	5 kW	P_{ex}	=	211 kPa
\dot{W}_1	=	\dot{W}_2	$r_{v,tot}$	=	16.48
			r_{v1}	=	4.9
			r_{v2}	=	3.363

Table 3.1: Steady state model inputs and results

As can be seen in Table 3.1, a mass flow of 150.8 g/s with a total volumetric ratio $r_{v,tot}$ of 16.48, divided into a 4.9 ratio for the first stage and 3.363 for the second one, is required to achieve the aforementioned requirements. Figure 3.1 represents the h - s and T - s diagrams of the full expansion. Among other observations, one can see on the h - s diagram that the physical properties of R245fa are such that as pressure increases, isobars become relatively compressed relative to enthalpy. Accordingly, for an equivalent amount of work ($\Delta h_1 = \Delta h_2$), the first pressure drop ΔP_1 must be higher than ΔP_2 of the second expansion, and correspondingly $r_{v1} > r_{v2}$.

3.2 Scroll generation

As described in the introduction, most of the scroll machines developed to date have a constant wall thickness profile. Nevertheless, in this project we investigate variable thickness scroll geometries since they are able to achieve a given volumetric process in a more compact expansion unit. This choice is motivated by the assumed relationship between the compactness factor (as defined in Equation 1.5) and the isentropic efficiency. Indeed a more compact scroll device would generate fewer leakages, mechanical and heat losses losses which would improve its expansion efficiency [24].

3.2.1 Danfoss frame

Scroll geometries are generated using an 8-dimensional planar curve frame developed by Gravensen and Henriksen. The following section gives some information about this generation tool without comprehensively explicating the mathematical details. A complete description can be found in the work of [11] and [12].

Although most planar curves are given by a parametrization like $t \rightarrow$

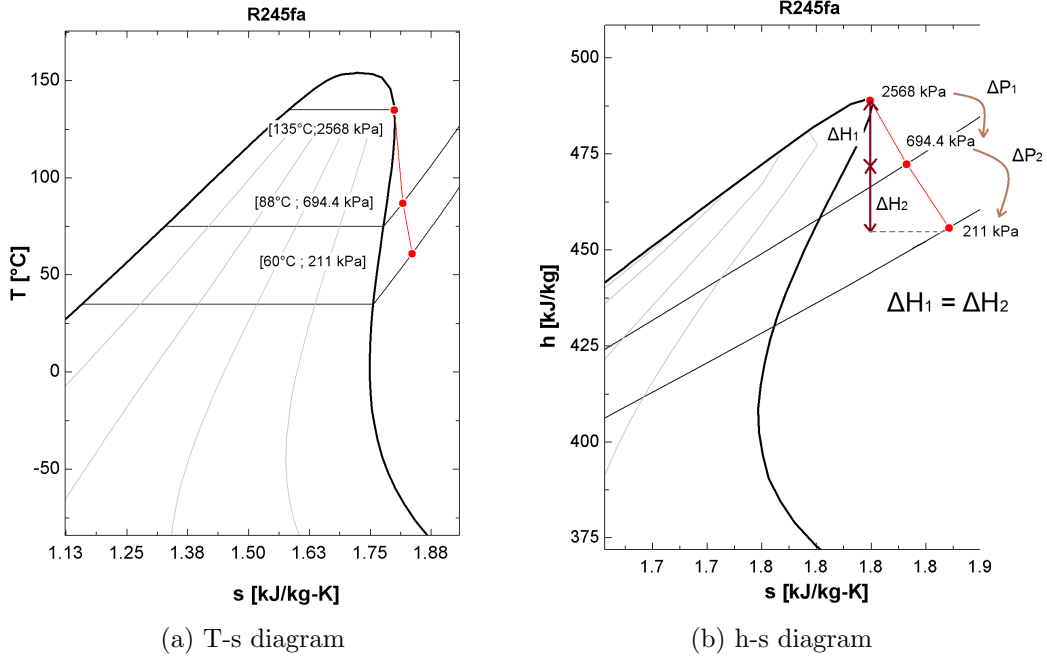


Figure 3.1: Two stage expansion diagrams

$\mathbf{x}(t)$, curves defining the shape of the scroll are represented by an *intrinsic* equation, i.e.:

$$s_x = c_1 + c_2\varphi + c_3\varphi^2 + c_4\varphi^3 + c_5\varphi^4 \quad (3.1)$$

where $[c_1, c_2, c_3, c_4, c_5]$ are five scalar parameters and φ is the tangent angles as shown in Figure 3.2a. From this equation, Cartesian coordinates for the initial scroll wrap can be derived as described in [11], giving

$$\mathbf{x} = [\alpha \sin(\varphi) + \beta \cos(\varphi), \beta \sin(\varphi) - \alpha \cos(\varphi)] \quad (3.2)$$

where α and β are values dependent on the aforementioned c_i and φ i.e.

$$\alpha = (c_1 - 6c_3) + (2c_2 - 24c_4)\varphi + 3c_3\varphi^2 + 4c_4\varphi^3 \quad (3.3)$$

$$\beta = (2c_2 - 24c_4) + 6c_3\varphi + 12c_4\varphi^2 \quad (3.4)$$

This result defines one side of the moving scroll. One can then determine the mating side on the fixed scroll as the envelope of the newly designed side of the moving scroll. Finally, the other mating pair of sides is given by reflection at a suitable point as represented in Figure 3.2b. A pair of scrolls is thus characterized by 8 parameters:

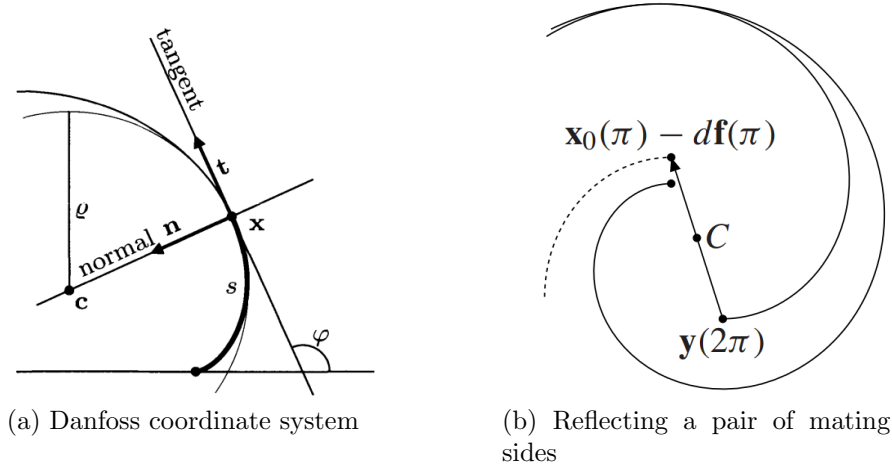


Figure 3.2: Scroll generation

- c_1, c_2, c_3, c_4 and c_5 - five scalar coefficients of the intrinsic equation;
- R - the orbital radius of the moving scroll
- N - the number of turns of the scroll spiral
- d - a scalar length related to the center point of reflection and the wall thickness

3.2.2 Parameter domains

This geometrical frame is a powerful tool which permits definition of any type of scroll geometry. However, it cannot be used in reverse so as to derive the 8 aforementioned parameters knowing some geometrical features of the wanted geometry (such as the initial thickness or the thickness profile). As a result, one has to choose random parameter values within an infinite space so as to generate several candidates and finally select the one that best meets the desired features. Unfortunately, most of the parameter combinations do not result in a viable geometry and it takes computational effort to generate and verify a large enough database of potential scroll geometries.

The scroll generation speed can nonetheless be increased by only exploring *viability domains* as traced by Orosz et al. in [25]. To define these parameter domains in which the probability to generate a viable geometry is greater, Orosz et al. have used a generate-and-test algorithm illustrated in Figure 3.5 for expanding the parameter domains until it detects their envelopes. With these envelopes, interdependent relationships between parameters are derived

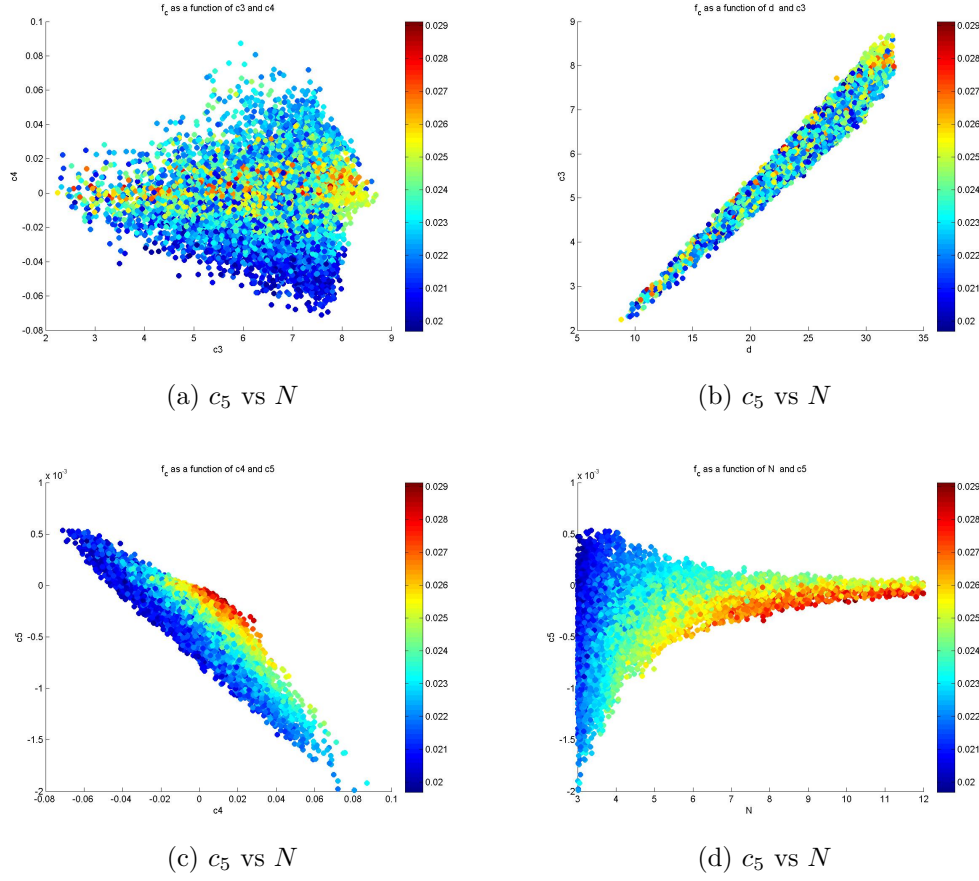


Figure 3.3: Parameters inter-dependence

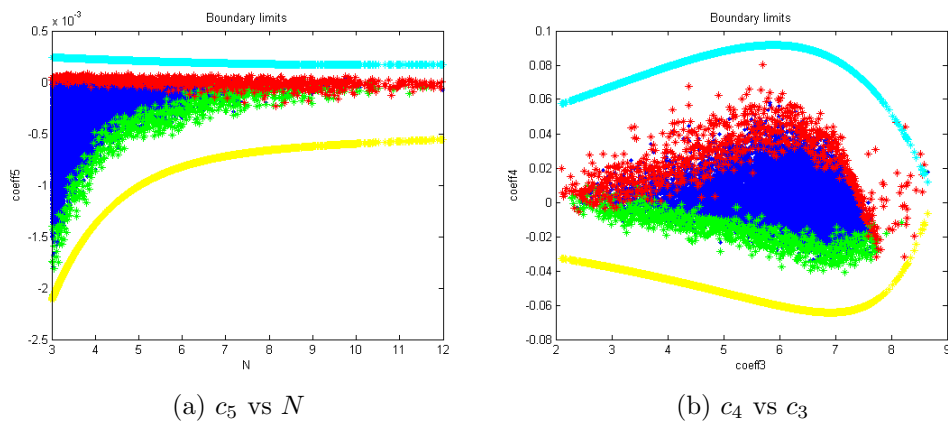


Figure 3.4: Lower (yellow) and upper (blue) domain limits

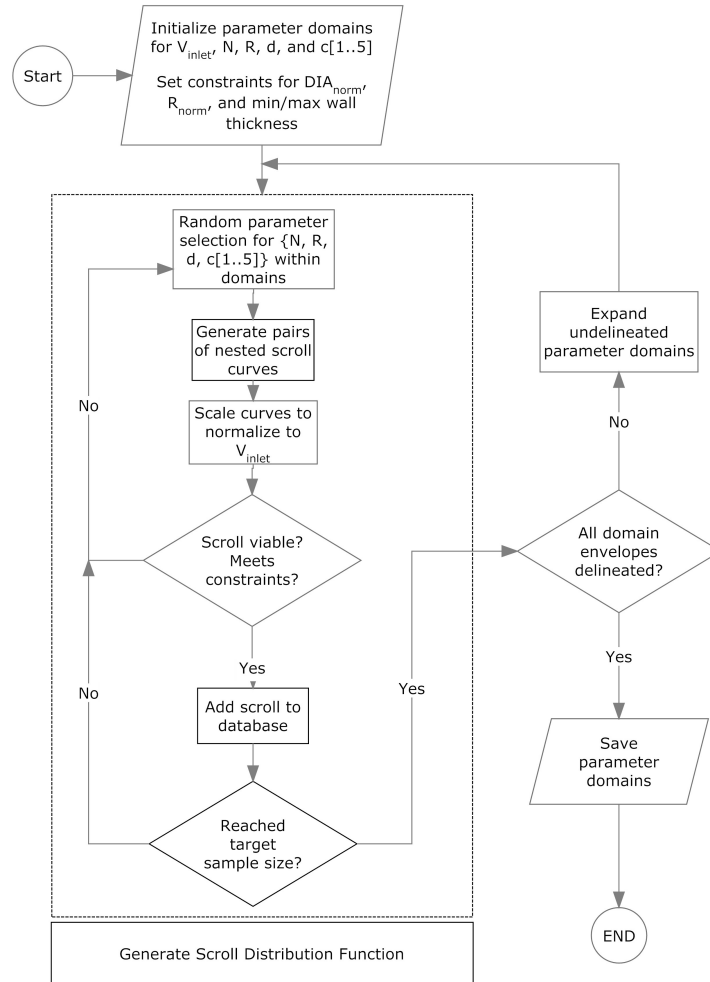


Figure 3.5: Orosz et. al.'s model algorithm

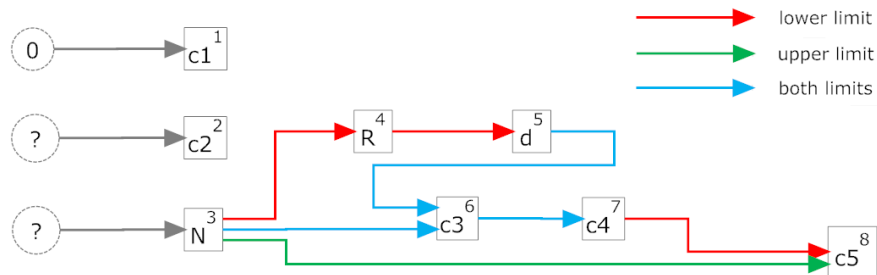


Figure 3.6: Hierarchical parameters selection

as represented in Figures 3.3. Each point in these Figures represents a viable geometry, the color illustrating its compactness factor as defined in Equation 1.5. From these relations, we derive a hierarchical parameter selection strategy (illustrated in Figure 3.6) so as to increase the viability probability of the candidate. The goal of this process is to refine the initial upper and lower domain limits ($X_{sup,init}$ and $X_{inf,init}$) of a parameter X in function of an already selected parameter Y^* , i.e.:

$$\begin{aligned} X_{dom,sup} &= \min(X_{sup,init}; f(Y^*)) \\ X_{dom,inf} &= \max(X_{inf,init}; g(Y^*)) \end{aligned} \quad (3.5)$$

where f and g are some equations expressing the upper and lower envelop limits of the parameter X in function to the other parameter Y . These equations are given by the Matlab function *EdgeFinder.m* and two examples are represented in Figure 3.4.

After having described the overall strategy to improve the probability to find a viable geometry, it is appropriate to define what is meant by *viable*. Once the pair of scrolls is normalized and scaled to satisfy the target inlet volume V_{in} , a geometry is defined as *non-viable* if one of the following condition is true:

- the spiral does not increase monotonically and it crosses itself or its mating curve;
- there is a violation of the conjugacy between the orbiting and the fixed scrolls;
- the scroll diameter is bigger than a limit defined as a function of the inlet volume (the relation is derived empirically by measurement on several Copeland scroll compressors);
- the inlet area is smaller than $100mm^2$, this value being defined in [10] as the smallest admissible inlet area before generating problematic throttling losses;
- the normalized orbital radius R^* is smaller than $2mm$. In the limit, an arbitrarily small orbit makes conversion of the orbiting motion of the moving scroll into rotation using an offset crank problematic;
- the wall thickness profile is not within the specified range. The next section explains how these limits are defined.

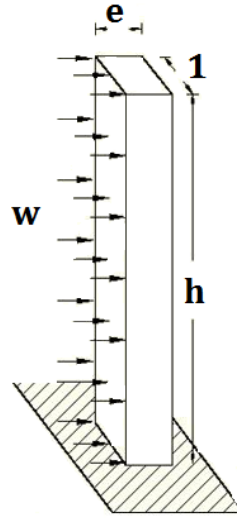


Figure 3.7: Cantilever beam theory

3.2.3 Minimum wall thickness requirements

The minimum scroll thickness profile is calculated so that the maximum wall deflection remains below a certain limit despite the pressure difference around the wall. This maximum deformation calculated empirically by measurements on several Copeland compressors is set to $5\mu m$.

The minimum thickness profile is calculated by modeling the scroll wall as a cantilever beam as illustrated in Figure 3.7¹. Following this assumption, the maximum deflection is given by

$$\delta_{max} = \frac{wh^4}{8EI} \quad (3.6)$$

Taking into account that $w = \Delta P.h$ and $I = \frac{1}{12}e^3$, one can reformulate Equation 3.6 and express the minimum wall thickness as

$$e_{min} = \sqrt[3]{\frac{3.\Delta P.h^5}{2.E.\delta_{max}}} \quad (3.7)$$

The last parameter to be set in order to solve Equation 3.7 is the scroll height h . For the first stage, the height is defined using a correlation with the inlet volume derived from the following empirical expression:

¹This assumption is conservative because the scroll curvature increases its deflection resistance.

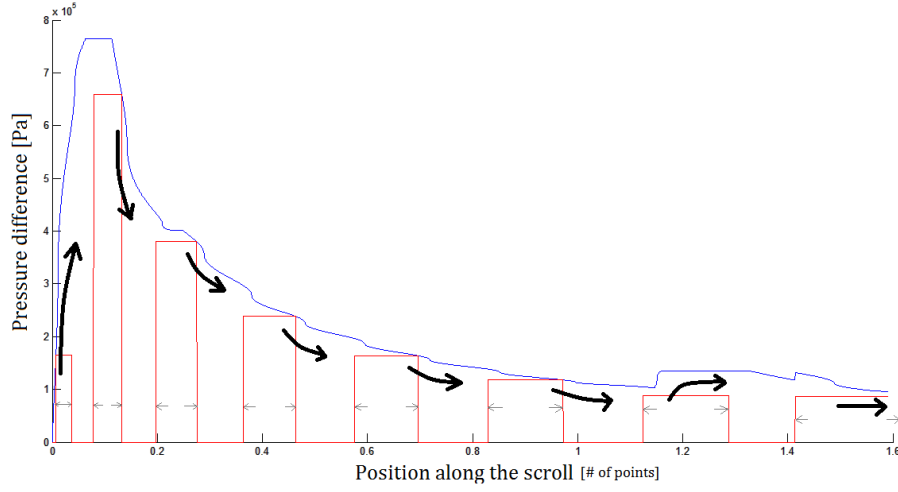


Figure 3.8: Pressure difference along the scroll

$$\frac{h}{mm} = 7. \left(\frac{V_{in}}{cm^3} \right)^{0.58} \quad (3.8)$$

This relation is once again derived from measurements taken on various Copeland scroll compressors. In the case of the second stage, Equation 3.8 provides a scroll height of $9.1cm$ which is impractical to manufacture (due to chattering in extended aspect ratio end mills); we thus impose a scroll height of $5cm$.

Whereas in [10] the thickness profile is derived from a power law based on two single points, this thesis realizes a deeper analysis of the pressure difference occurring along the scroll wraps over the course of a full revolution of the orbiting scroll. Based on the aforementioned equations and the modeled pressure in each expansion chamber, the matlab code *ThicknessProfile.m* computes the pressure difference occurring along every point of the orbiting scroll at every step angle of the discretized orbit. The thickness is then designed using the envelop of the maximum pressure difference observed at every point. The simulation results for one geometry are shown in Figure 3.8 and an animated video can be generated by running *ThicknessProfileAnimation.m*. Several comments are pertinent to this simulation.²

- As shown in Figure 3.9, each side along the scroll can either experience equivalent pressure or a pressure difference derived from two adjacent chambers. This explains why the ΔP profile (represented in red in Figure 3.8) is not a smooth curve but a succession of sliding rectangles.

²These observations are expressed in term of the orbiting scroll, but the same results could be derived for the fixed one.

Specifically, one half of the scroll is subjected to a pressure difference while the other half is not, as represented in Figure 3.9.

- While a monotonically decreasing profile might be expected intuitively, in fact there is an observable increase in the ΔP_{max} curve initially. It is important to keep in mind that even though the pressure decreases in the evolving expansion chambers, the pressure at the inlet remains relatively constant.³ The pressure difference ΔP along the scroll thus increases as long as one side remains in contact with the inlet while the other interacts with the first expansion chamber.
- As soon as both sides of the orbiting scroll are facing two adjacent expansion chambers, the pressure difference profile decreases monotonically.
- When the last expansion chamber $NCOMP+1$ opens to the exhaust, its pressure changes so as to be adapted to the outlet conditions. This pressure change occurs faster than the expansion process of the previous chamber $NCOMP$, resulting in a noncontinuous increase of the ΔP_{max} profile. This indicates a potential failure mode for a minimum wall thickness scroll geometry: **it may not withstand a severe over-or-under expansion if it has not been designed for this situation.** Note that the same warning applies to constant wall thickness scrolls, but where these are "over built" with respect to design conditions at the exhaust chamber the effect would be less severe. If the scroll geometry is optimized for design conditions having inlet and exhaust pressures corresponding to the expander volume ratio r_v , it may prove frail in off-design operation. In this case, the pressure difference experienced by the scroll at the end of the expansion process will increase and generate a higher scroll deflection resulting in leakages between the last expansion chambers and the exhaust. Figure 3.10 gives an example for two cases (over- and under-expansion) illustrating the area in which the thickness requirement (in magenta) is greater than the designed wall thickness (in blue). It should be noted that these constraints are conservative given that the 2D curvature of the scroll will tend to reinforce its resistance to the 1D deflection analyzed here.

This analysis raises another issue represented in Figure 3.11: the maximum pressure difference profile (and thus the minimum wall thickness requirements) depends on the scroll geometry. One is then confronted with a circular reference problem, also known as the *chicken or the egg* dilemma:

³notwithstanding the small pressure drop due to the inlet throttling

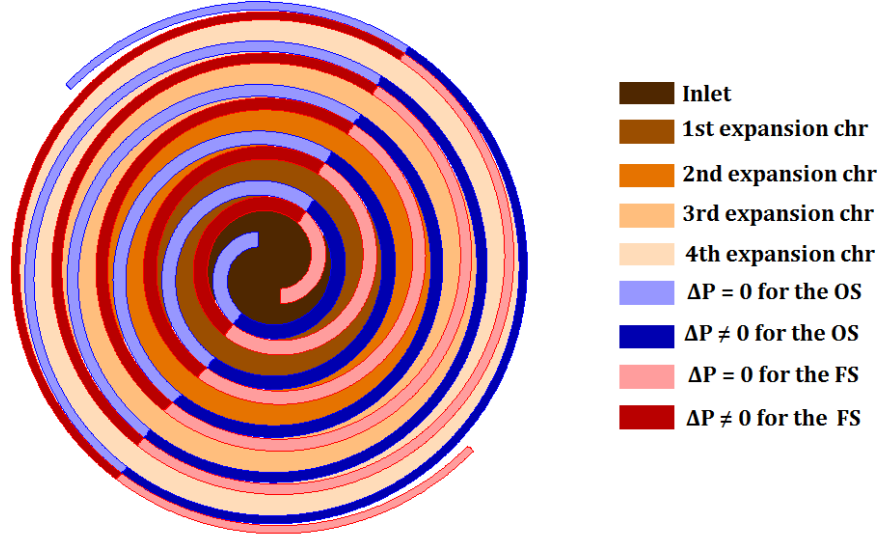


Figure 3.9: Selection process diagram

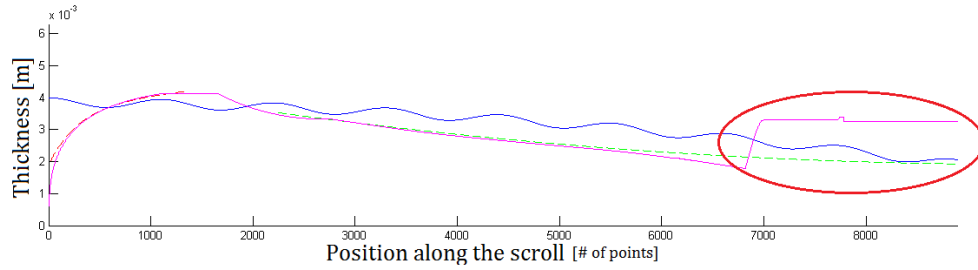
(a) Severe under-expansion ($r_{v,expander} = 4.9$ and $r_{v,actual} = 7$)(b) Severe over-expansion ($r_{v,expander} = 4.9$ and $r_{v,actual} = 2$)

Figure 3.10: Comparison between the actual wall thickness (blue) and the minimum one required (magenta) in case of an over/under-expansion

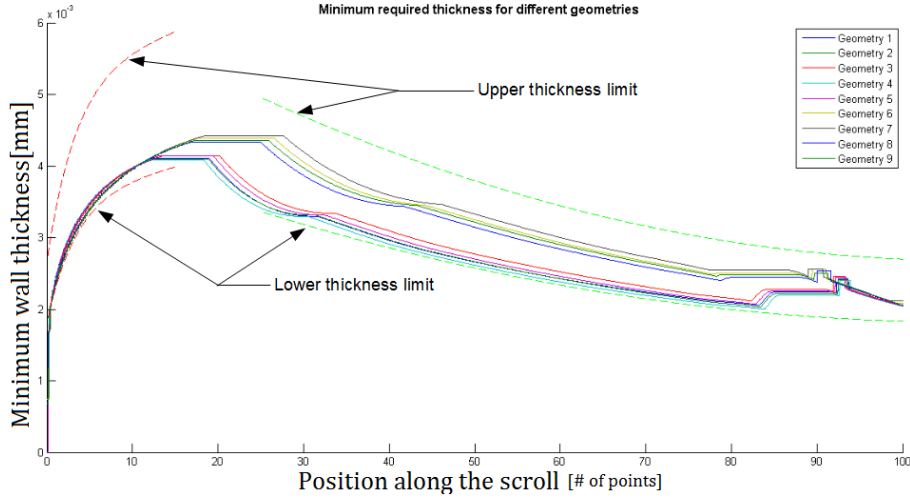


Figure 3.11: Pressure difference along the scroll

the minimum thickness profile is required as a viability criteria for the scroll generation procedure, but this profile depends on the geometry itself. To overcome this situation, a conservative thickness profile is derived from different geometries simulated as shown in Figure 3.11. The thickness integrity of selected geometries is then verified *ex post facto*, as explain in the next section.

Finally, the maximum wall thickness profile is obtained by multiplying the minimum one by a constant k ($k = 1.25$, for example) so as to define a viable thickness range as represented in Figure 3.11.

3.3 Selection strategy

As described above, the eight scroll parameters cannot be determined a priori by virtue of selecting some geometrical features; these must be chosen from candidates within a database that closely match the requirements. The scroll database is generated using the Matlab code *Scroll_Generator.m* which is based on the process described previously. Because the entire database is not generally generated by a unique simulation, we use the Matlab function *Collector_of_data.m* so as to assemble all the geometries into a single database file.

To parse the scroll database, the Matlab function *Scroll_selector.m* is used to select the geometries matching the previously defined volumetric ratio requirements⁴ and to rank them according to their compactness factor.

⁴ $r_v \in [r_{v,min} - r_{v,max}]$

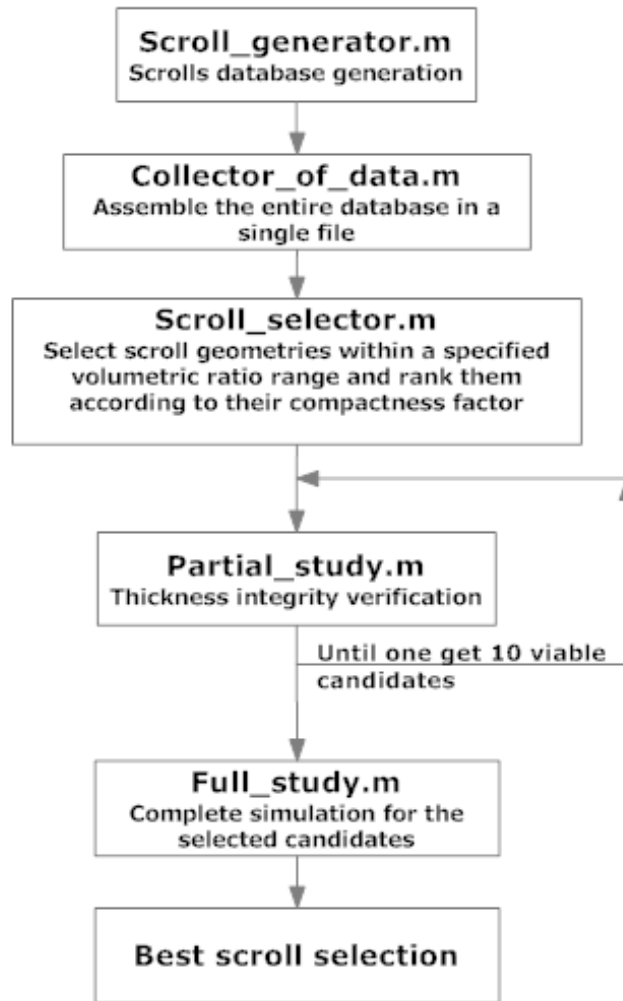


Figure 3.12: Selection process diagram

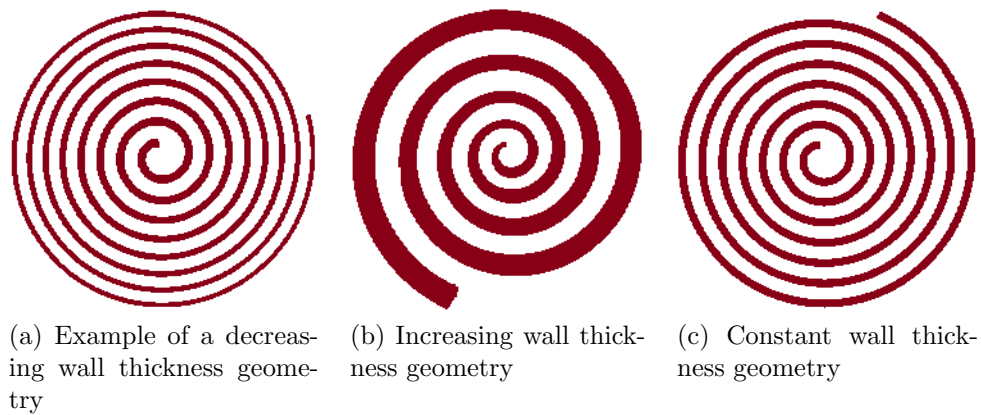


Figure 3.13: Three types of geometry investigated

As pointed out in Chapter 2, the modeling time is directly proportional to the degree of angular discretization. It is thus computationally expensive/time-intensive to run an arbitrarily accurate simulation for every geometry. To overcome this problem, the following procedure is employed: for the first geometry ranked, the model is run with a low angular step number⁵ so as to generate quickly the thickness profile required to check the geometry's integrity. If its thickness profile is greater than the required one, the geometry is kept as candidate. If it is not, the same process is carried out with the next geometry in the ranking. This process is then repeated until a target number of candidates is achieved (in this study, 13 candidates). Finally, a complete simulation⁶ for these candidates is performed using the function *Full_study.m* based on the geometric and the thermodynamic model described in Chapter 2. The candidate having the highest expansion isentropic efficiency is evaluated for prototyping.

3.4 Results discussion

This section analyzes the results of this study and describes the selected geometries for both stages. Although only a summary is given here, all of the results obtained by simulation can be found in the attached CD.

3.4.1 First stage geometry

The database explored for the first stage contains 11,448 geometries. After applying the selection process described in the previous section, 13 candidates were retained and classified according to three types of geometry : increasing,⁷ constant,⁸ and decreasing⁹ wall thickness geometries (see Figure 3.13). Table 3.2 summarizes the performance simulated with the deterministic model and Figure 3.14 illustrates the isentropic efficiency as a function of the compactness factor for the different candidates.

In agreement with our initial expectations, the constant (#12) and the increasing (#13) wall thickness geometries are found to present the lowest isentropic efficiencies. Furthermore, the candidate selected for the first stage is the geometry #10 presenting the highest compactness factor and which is represented in Figure 3.15. This decision is motivated by the following advantages:

⁵*num_ang_step* = 200

⁶*num_ang_step* = 1000

⁷#12, represented by "I"

⁸#13, represented by "C"

⁹#1 → 11, represented by "D"

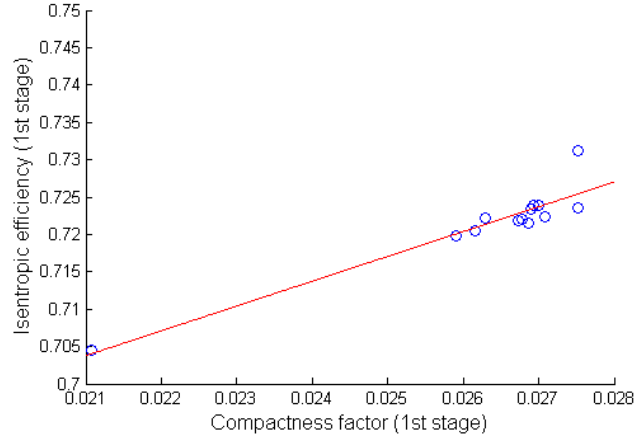


Figure 3.14: Relation between compactness factor and isentropic efficiency (first stage candidates)

- it has the highest isentropic efficiency;
- it has the smallest diameter and uses the least stock material.
- it has the highest orbiting radius ($R = 2.2mm$) which facilitates power takeoff with the offset crank (see Chapter 4).

However, looking at Figure 3.15, one can observe a small zone where the thickness criteria is not fully respected. In this case the small difference is considered negligible in light of the expectation that the scroll's curving shape increases its bending resistance.

The influence of the different loss mechanisms on the expansion performance is informative from a design perspective. Table 3.3 shows the evolution of the isentropic efficiency as a function of the losses explicitly taken into account in the model. Furthermore, Figure 3.16 displays the relative fraction of the different mechanical losses responsible for the 14.43% efficiency drop.

3.4.2 Second stage

The second geometry is chosen from a database including 11,091 geometries. Figures of merit for the 13 candidates kept by the selection process are shown in Table 3.4 and Figure 3.17 shows the isentropic efficiency as a function of the compactness factor for the second stage candidates. As for the first stage, it is evident that the constant and the decreasing wall thickness geometries present the lowest isentropic efficiencies. Moreover, comparing results in Table 3.2 and 3.4, one can observe that candidates of the second stage have

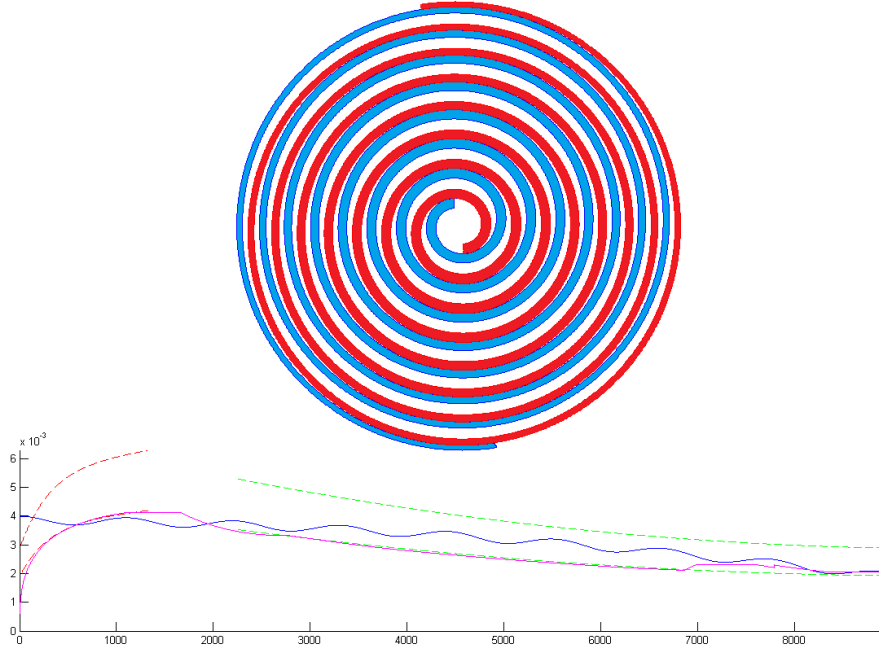


Figure 3.15: Scroll geometry selected for the first stage

#	r_v	D (mm)	f_c	η_{is} (%)	Types	Ranking
1	4.904	181.6	0.027006	72.9577	D	2
2	4.8063	183.8	0.02612	72.6324	D	11
3	4.8291	178.3	0.027087	72.7916	D	7
4	4.8166	179.2	0.023872	72.7048	D	10
5	4.8928	177.8	0.027514	72.8963	D	5
6	4.834	180.9	0.026724	72.7514	D	9
7	4.8259	180.2	0.026778	72.7647	D	8
8	4.8903	181.6	0.02629	72.9528	D	3
9	4.8696	181.1	0.026899	72.9003	D	4
10	4.8926	177.7	0.027521	73.6751	D	1
11	4.8246	183.47	0.026296	72.8004	D	6
12	4.9146	233.2	0.021077	71.4089	I	13
13	4.8475	187.1	0.02591	72.5887	C	12

Table 3.2: Performance table for the first stage

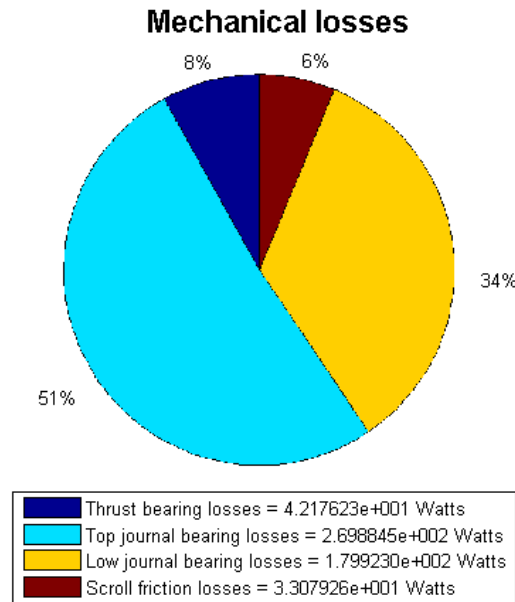


Figure 3.16: Mechanical losses fraction in the first stage

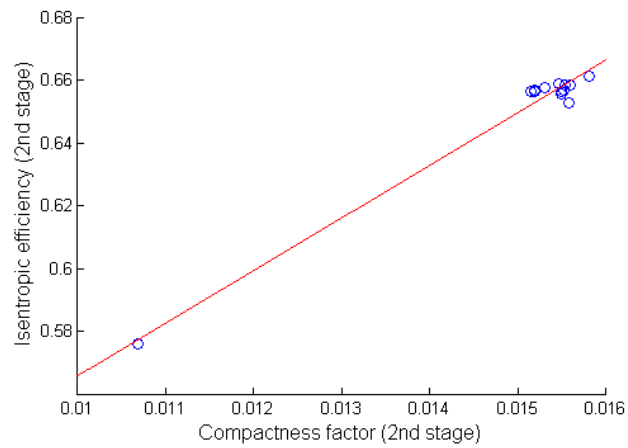


Figure 3.17: Relation between compactness factor and isentropic efficiency (second stage candidates)

Losses modeled	η_{is}	$\Delta\eta_{is}$
Inlet and Outlet throttling	97.19 %	-
<i>same as the previous</i> + Mechanical losses	82.77 %	14.43 %
<i>same as the previous</i> + Flank leakages	77.26 %	5.51 %
<i>same as the previous</i> + Radial leakages	73.67 %	3.59%
<i>same as the previous</i> + Ambiance heat losses	73.12 %	0.55 %

Table 3.3: Influence of losses on the isentropic efficiency - first stage

a smaller compactness factor and correspondingly a smaller isentropic efficiency.

The geometry chosen for the second expansion stage is candidate #1 which is shown in Figure 3.18. It is characterized by an efficiency of 66.14% and a volumetric ratio of 3.357. Like for the first stage, it is the geometry characterized by the highest compactness factor that presents the best expansion efficiency. Following the process used in evaluating the first stage, the influence of the different losses on the isentropic efficiency as well as the relative fraction of mechanical losses is illustrated in Table 3.5 and Figure 3.19.

Comparing mechanical losses between the first and the second stage (Figures 3.16 and 3.19), one can observe that $W_{loss,2nd}$ ($\simeq 720W$) is much greater than $W_{loss,1st}$ ($\simeq 530W$). Even if journal and thrust bearings losses are roughly similar, friction losses between the two scrolls are much greater in the second stage. This can be explained by the larger specific volume of R245fa in the second stage resulting in a larger pair of scrolls and thus a larger contact area.

3.4.3 Overall expansion

The full expansion process is characterized with an isentropic efficiency given by

$$\eta_{is,tot} = \frac{\dot{W}_{1st} + \dot{W}_{2nd}}{\dot{m}(h_{su} - h_{ex,is})} \quad (3.9)$$

After substitution of the corresponding values, we find a full expansion isentropic efficiency of $\eta_{is,tot} = 68.6\%$. The most interesting expansion properties are summarized in Table 3.6 and one can see in Figures 3.20, 3.21 and 3.22 the temperature, pressure and enthalpy evolution profiles in both expansion stages.

To conclude this chapter, the overall expansion improvement achieved by the scroll expander design process is compared to current best practice, i.e.

#	r_v	D (mm)	f_c	η_{is} (%)	Types	Ranking
1	3.357	212.4	0.015804	66.14	D	1
2	3.328	213.5	0.015588	65.83	D	4
3	3.354	215.8	0.015539	65.85	D	3
4	3.307	213.1	0.015524	65.66	D	7
5	3.353	216.9	0.015461	65.88	D	2
6	3.324	214.5	0.015496	65.66	D	8
7	3.356	216.7	0.015491	65.55	D	11
8	3.351	219.1	0.015298	65.75	D	5
9	3.305	217.6	0.015188	65.67	D	6
10	3.322	218.7	0.015188	65.64	D	9
11	3.367	222.4	0.015143	65.62	D	10
12	3.363	314.8	0.010686	57.61	I	13
13	3.364	216.1	0.015573	65.27	C	12

Table 3.4: Performance table for the second stage

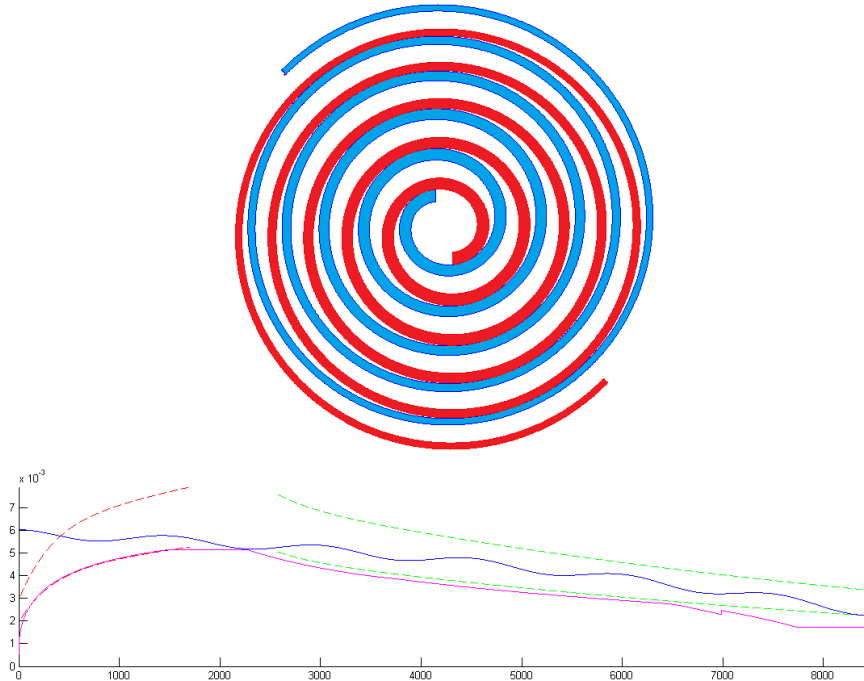


Figure 3.18: Scroll geometry selected for the second stage

Losses modeled	η_{is}	$\Delta\eta_{is}$
Inlet and Outlet throttling	88.7 %	-
<i>same as the previous</i> + Mechanical losses	68.75 %	19.95 %
<i>same as the previous</i> + Flank leakages	68.02 %	0.73 %
<i>same as the previous</i> + Radial leakages	66.68 %	1.34 %
<i>same as the previous</i> + Ambiance heat losses	66.14 %	0.54 %

Table 3.5: Influence of losses on the isentropic efficiency - second stage

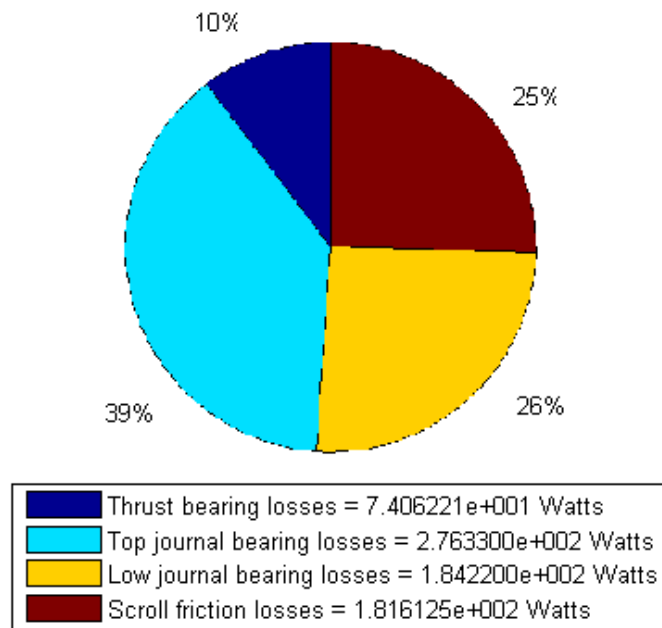
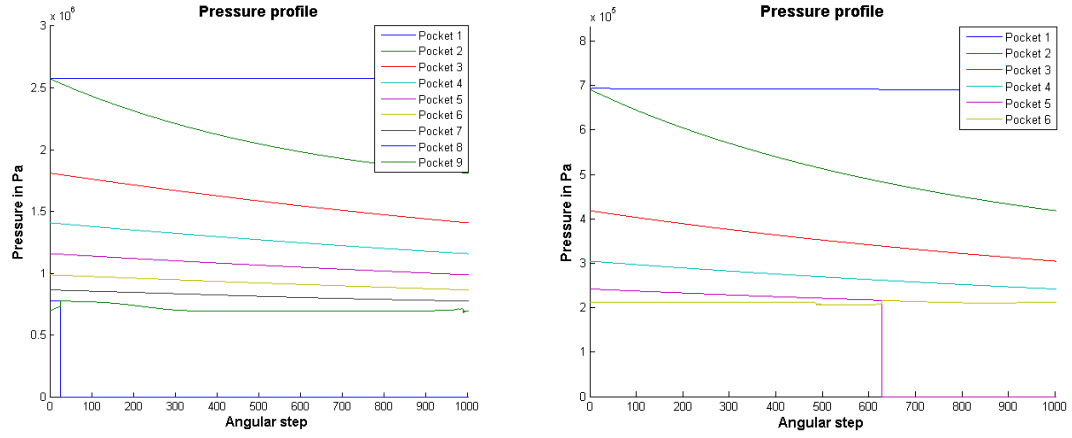


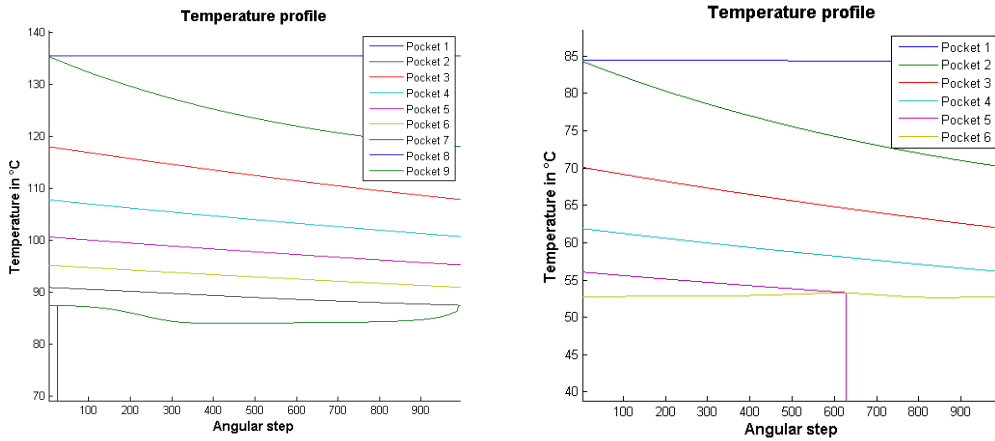
Figure 3.19: Mechanical losses fraction in the second stage



(a) First stage

(b) Second stage

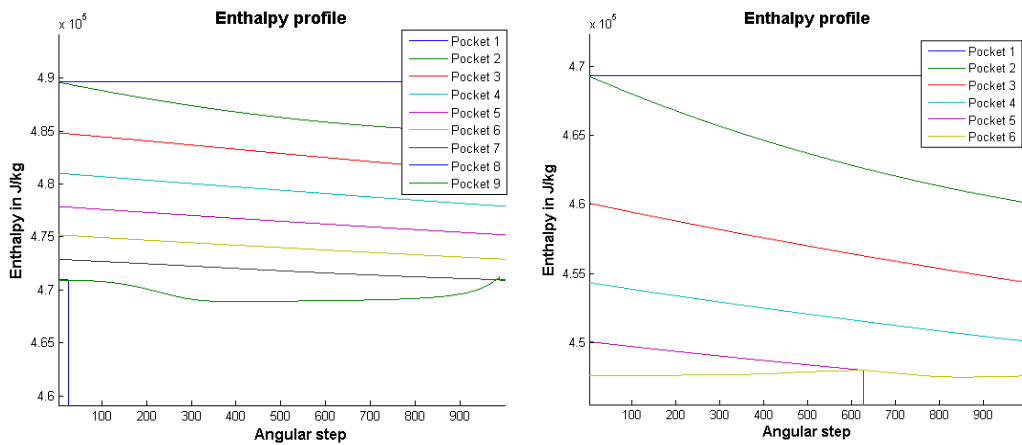
Figure 3.20: Pressure profile in each pocket



(a) First stage

(b) Second stage

Figure 3.21: Temperature profile in each pocket



(a) First stage

(b) Second stage

Figure 3.22: Enthalpy profile in each pocket

	First stage	Second stage	
T_{su}	135	84	$^{\circ}C$
T_{ex}	84	53	$^{\circ}C$
P_{su}	2576	692.3	kPa
P_{ex}	693.5	212.5	kPa
h_{su}	489.6	469	$kJ/kg.K$
h_{ex}	469	447	$kJ/kg.K$
r_v	4.89	3.36	$[-]$
η_{is}	73.127	66.14	$\%$
\dot{W}	3.03	2.501	kW

Table 3.6: Thermophysical properties of the full expansion

expansion by two reversibly employed scroll compressors in series. Assuming two constant wall thickness scroll compressors having a volumetric ratio of 2.8,¹⁰ the deterministic model described in Chapter 2 is run to obtain the results summarized in Table 3.7.¹¹¹²¹³

From Table 3.7, one can summarize our different investigations as follow

- In the case of an expansion performed by two commercial scrolls having small intrinsic volumetric ratios ($r_v = 2.8$, design A), the isentropic efficiency is severely penalized by large under-expansion losses especially in the first expansion stage. The efficiency would be 61.9% and 64.9% for the first and the second stage respectively, and the overall expansion would be characterized by a 62.4% isentropic efficiency.
- In the case of optimized volumetric ratios scroll geometries with a constant wall thickness profile (geometries #13 in Tables 3.2 and 3.4, design B in Table 3.7), the efficiency is improved by 10.8% and 0.37% in the first and the second stage. Hence, the expansion performance η_{is} are 71.98% and 65.27% for both stages, resulting in an isentropic efficiency of 67.43% for the entire expansion process.
- In the case of optimized volumetric ratios scroll geometries with a min-

¹⁰typical value for Copeland compressors

¹¹Design A : minimum wall thickness scroll geometries with optimal volumetric ratios

¹²Design B: constant wall thickness scroll geometries with volumetric ratio of 2.8 for both expansion stages

¹³Design C: constant wall thickness scroll geometries with optimized volumetric ratio both expansion stages

	Design A	Design B	Design C	
Wall thickness	Constant	Constant	Decreasing	[−]
$r_{v,1st}$	2.8	4.9	4.89	[−]
$r_{v,2nd}$	2.8	3.36	3.36	[−]
\dot{W}_{1st}	2.57	2.97	3.03	kW
\dot{W}_{2nd}	2.47	2.49	2.51	kW
\dot{W}_{tot}	5.04	5.45	5.54	kW
\dot{W}_{is}	8.08	8.08	8.08	kW
$\eta_{is,1st}$	61.9	71.98	73.12	%
$\eta_{is,2nd}$	64.9	65.27	66.14	%
$\eta_{is,tot}$	62.4	67.43	68.6	%

Table 3.7: Comparison of the performance of the Design A, B and C

imum wall thickness profile (design C in Table 3.7), the first and second stage improvements (in comparison to the Design A) are respectively 11.22% and 1.24% and thus their expansion efficiencies are equal to 73.12% and 66.14%. The overall expansion is finally characterized by a η_{is} of 68.6%.

In summarizing the above results, it can be concluded that improvements are possible in scroll expanders optimized for use in an ORC. Optimizing the volume ratio has a larger predicted effect (5.03%) on isentropic efficiency than optimizing the wall thickness profile (1.17%). These gains are additive and sufficiently large to justify further research and development in this topic (i.e. an overall efficiency improvement of 6.02%). To ascertain the reliability of these estimates, the design approach should be tested in an experimental setting. Towards this end, the next phase of work involves construction of a single stage prototype as presented in the two next chapters.

Chapter 4

Prototype architecture and CAD modeling

Once the scroll geometries are selected, the next step is to design the expander architecture. Because the accuracy of design tool is uncertain, a single stage prototype will be built and tested to validate the thermodynamic model. Since the 1980's, most mechanical designs are realized by CAD (*Computer-Aided Design*) referring to the use of computer systems to assist in the creation, modification or optimization of a design. In the frame of this project, the CAD environment is *Solidwork Student Edition 2012*. SolidWorks is a 3D mechanical CAD software which incorporates powerful design and simulation functionalities that make it widely used in the engineering world. Among its advantages, Solidworks presents the opportunity to work with the free CAM add-on HSMXpress. CAM (*Computer-Aided Manufacturing*) refers to the use of computer software to control machine tools and related machinery in the manufacturing of workpieces. In the scope of this project, HSMXpress is used with SolidWorks to generate high accuracy tool paths which are then uploaded in a Computer Numerical Control (CNC) machine to realize complex and accurate machining operations. This chapter provides a complete description of the expander architecture, followed by a brief note regarding 3D printing and CAM. Finally a draft drawing of the two-stage design is given.

4.1 Architecture and pieces description

The architecture presented here is the result of many updates to the initial solid model designed by Bertrand Dechesne (University of Liège) and Laurent Branthôme (Enertime). The basic features are derived from Copeland compressor ZR series.

4.1.1 Overall architecture

The single stage prototype is made of 30 pieces assembled as represented in Figure 4.1 and 4.2. The components inventory is as follows:

- | | | |
|--------------------|---------------------|---------------------|
| a) Expander inlet | j) Top bearing | s) Bottom bearing |
| b) Top gasket | k) Guiding tubes | t) Cross |
| c) Top BPC seal | l) Shaft adapter | u) Oil pump |
| d) Middle BPS seal | m) Low stator | v) Oil pump adapter |
| e) Low BPC seal | n) Main bearing | w) Bottom gasket |
| f) Fixed scroll | o) Generator rotor | x) Bottom flange |
| g) Orbiting scroll | p) Coil | y) Counterweight |
| h) Oldham joint | q) Supporting tubes | z) Casing |
| i) Thrust bearing | r) Supporting belt | |

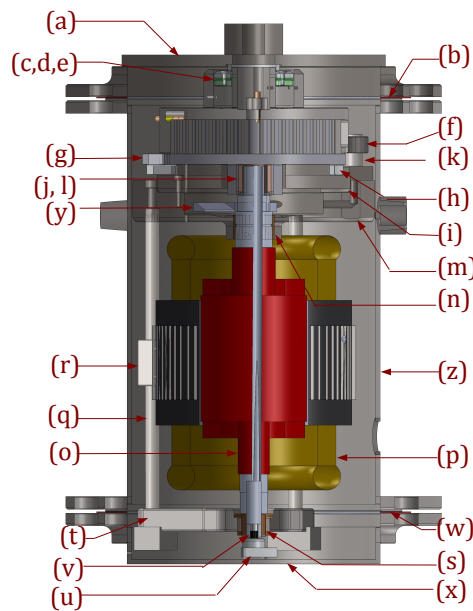


Figure 4.1: Overall scroll expander

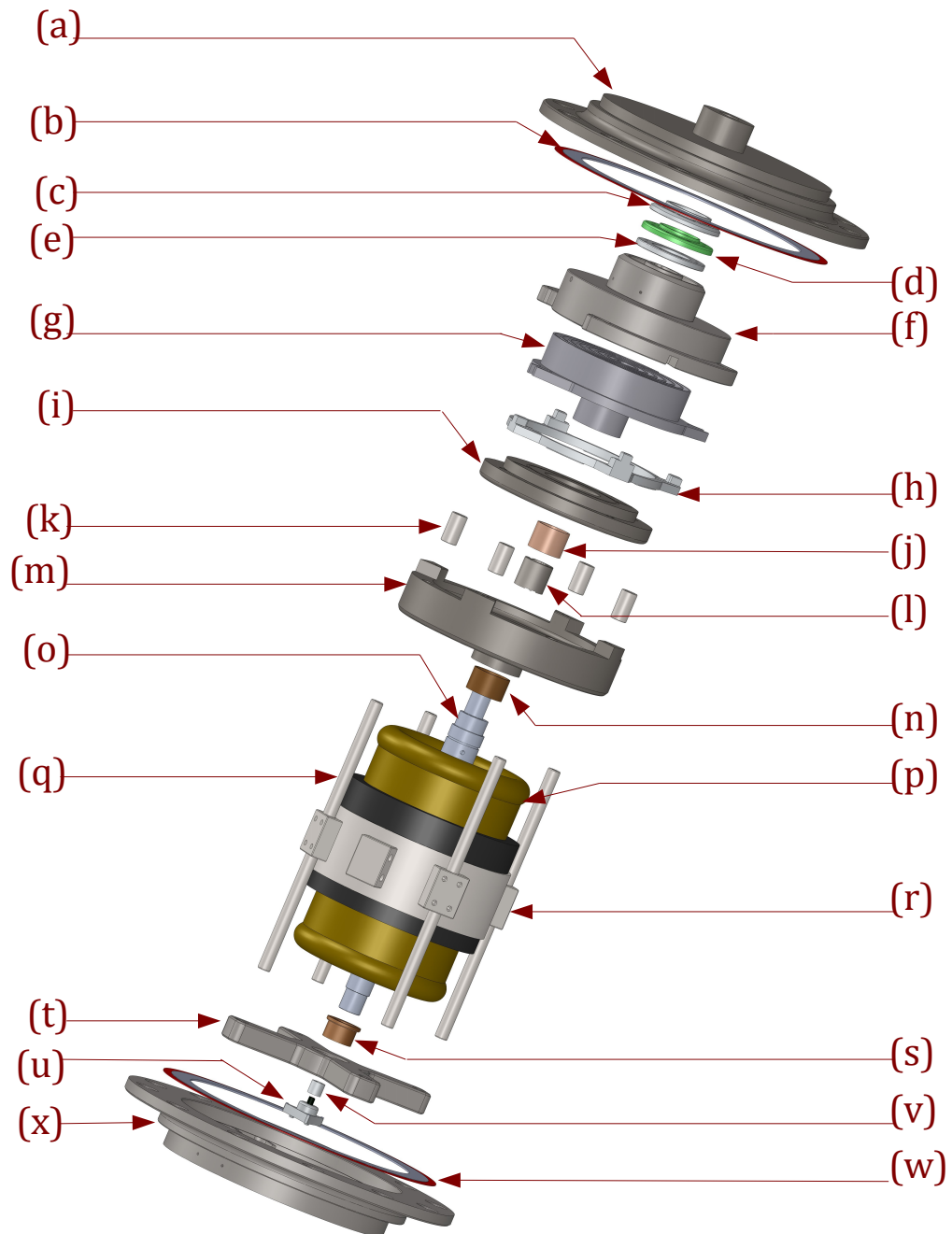


Figure 4.2: Exploded view of the expander

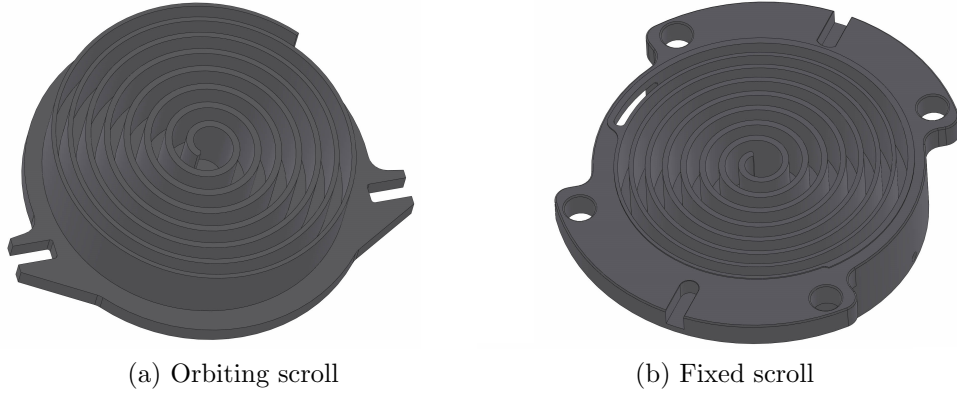


Figure 4.3: Scrolls

4.1.2 Fixed and orbiting scrolls

The expansion process takes place between the fixed and the orbiting scrolls represented in Figure 4.3. While most geometrical features can be designed using standard SolidWorks sketch tools, scroll curves have to be imported directly from Matlab to ensure a high accuracy. This process is achieved using the Matlab function *GeomSolidworks.m* which saves XYZ curves coordinates in a *.sldrcv* file which is then imported in SW to be interpolated by a fitting spline. As described in [10], the scroll coordinates are represented such that the further the spiral curve is from the center, the greater the distance between two points. To keep a relatively constant distance between each pair of points, the exported scroll curves are resampled as several segmented sub-curves of increasing angular resolution (parameters n). However, given limited processor power and the tendency of SW to crash when handling above a certain number of imported points, a trade-off between curve accuracy and computer capacity is necessary.¹

The curves location on the orbiting scroll plate is chosen so as to keep a suitable center of mass and to avoid side leakages during a complete revolution. Indeed, if curves are not appropriately located, an absence of contact between the fixed scroll tip and the orbiting scroll plate can occur resulting in a direct leakage to the outlet. For the same reason, the initial U-shaped tab guides for the oldham coupling ([10]) are redesigned to ensure a leakage-free expansion.²

¹in this study a 13,000 points curve resolution is achieved, giving an inter-points distance equal to 14 *μm* at the center and 350 *μm* at the end. A higher value at the end is tolerated because of the smaller degree of curvature to be interpolated

²Although outlet leakages are not a problem for a single stage expander (since they

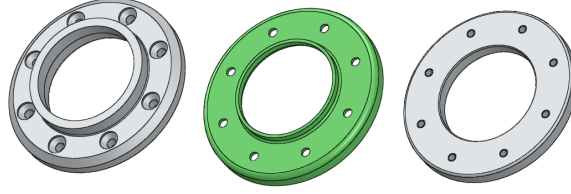


Figure 4.4: BPC gaskets

The fixed scroll features a back pressure chamber (*BPC*) on its upper side (Figure 4.5a). This toroidal chamber is filled by high pressure fluid designed to exert an force in the axial direction to maintain an axial compliance between the two scrolls (which are repelled because of the internal pressure). BPC diameters are obtained by expressing the axial equilibrium i.e.:

$$\frac{\pi}{4}[(D_{fs,o}^2 - D_{bpc,o}^2)P_{ex} + (D_{bpc,o}^2 - D_{in,o}^2 + D_{in,i}^2)P_{su}] + W_{weight} + F_{spring} = F_{repulse} \quad (4.1)$$

where $F_{repulse}$ is the repulsive force given by the thermodynamic model, $D_{bpc,o}/D_{bpc,i}$ are the outside/inside BCP diameters, $D_{in,o}/D_{in,i}$ are the outside/inside inlet port diameters, $F_{spring} = n_{spring}k(L_{init} - L_{cmp})$ with n_{spring} and k the number of springs and their stiffness, L_{init}/L_{cmp} the initial and compressed string length, $W_{weight} = g.m_{ass}$ is the fixed scroll weight, and, finally, P_{su}/P_{ex} the supply/exhaust pressure.³

Instead of connecting the BPC directly to the inlet port, two holes are drilled through the outside so as to realize a BPC control circuit as represented in Figure 4.11. This provides an ability to control the chamber's pressure and thereby the axial compliance of the two scrolls. This would in turn facilitate a proposed analysis to investigate the effect of BPC pressure on the expander efficiency and derive an optimum. It is expected that an excessive pressure generates higher friction resulting in mechanical losses, whereas insufficient in excessive leakages. The combined BPC and inlet port seal is made of three elements that actuate as a piston, represented in Figure 4.4. Although under working conditions this piston is pushed up against the inner lip of the expander inlet because of the pressure difference, eight evenly spaced springs are fixed in the BPC so as to support the piston during startup. Without these springs, the absence of a pressure difference would

occur at the end of the expansion process), they must be avoided in the case of a two-stage/single-shaft design.

³To maintain a factor of safety in case of a design oversight, the actual diameters $D_{bpc,o*}$ and $D_{bpc,i*}$ are obtained by multiplying the results given with Equation 4.1 by 1.25

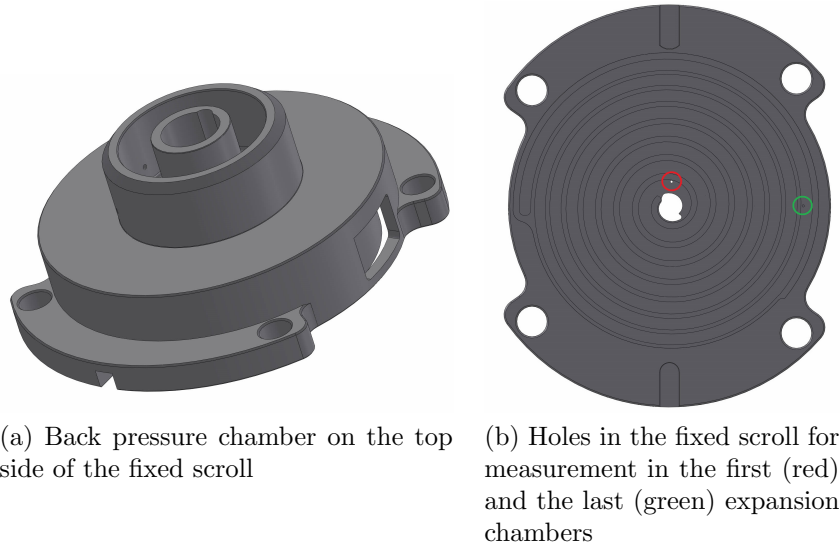


Figure 4.5: BPC and pressure holes

fail to push up the piston and it would remain at the bottom of the BPC, the inlet port would not seal, and the refrigerant would by-pass the expander and flow out of the enclosing pressure vessel.

The fixed scroll piece is also designed in order to facilitate pressure measurements in the first and the last expansion chambers. Two holes are thus drilled in strategic locations as represented in Figure. Ideally, sensors should be flush-mounted, but access restriction constrains the sensors to be installed recessed. In such a case, as has been analyzed by Walter et al. [27], the pressure from the expansion chamber travels through an indicator passage to reach the sensor which results in signal distortions due to acoustic oscillations and phase shift. It is thus important to design the indicator passages so that the natural frequencies are much higher than the measured signal frequency.⁴

4.1.3 Electric generator

Electric power is produced by a 5.6kW *Wattsaver Plus* induction machine manufactured by Leeson and composed of a coil (stator) and a shaft (rotor). Asynchronous machines are well suited to work as generators given that they present advantages such as a simple and robust construction, a minimal maintenance and a low-cost.

⁴The specification of this part of the design is ongoing at the time of writing of this thesis

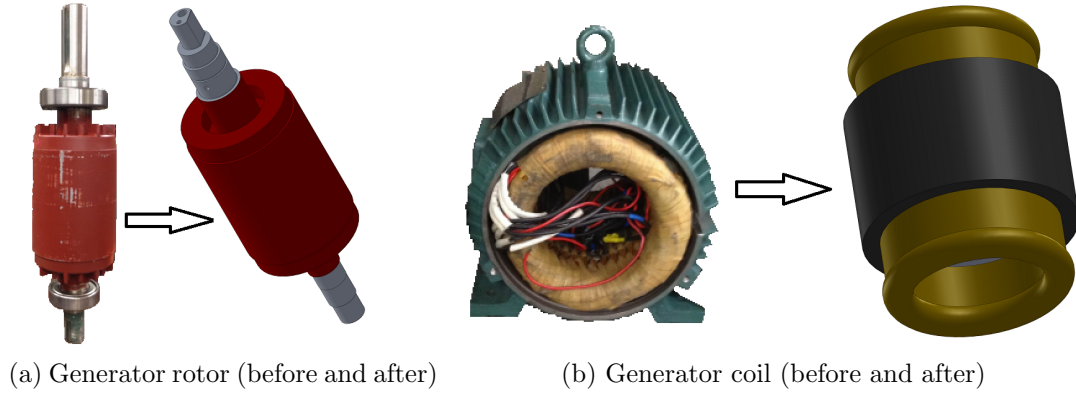


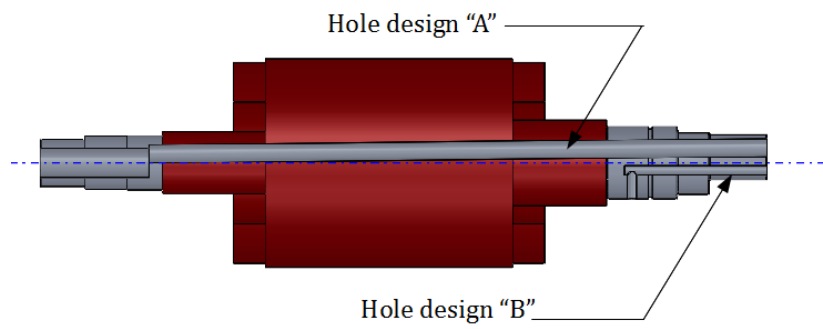
Figure 4.6: Induction generator

The initial motor is machined to become the parts represented in Figure 4.6. The coil is simply removed from its casing whereas the rotor requires significant adaptation via machining. Since the moving part orbits, the shaft requires an offset crank so as to translate the scroll motion into a rotation. One can notice in Figure 4.7b that the offset value ($R' = 3.091mm$) is not equal to the actual orbit radius ($R = 2.199mm$). The shaft was actually machined for a first scroll geometry and has been modified thereafter. To avoid buying a new generator, the shaft adapter is designed with a larger radial clearance so as to be positioned at a radial offset R instead of R' and thus correct the difference $\Delta R = R' - R$. The other shaft end is simply turned to fit the bottom flanged sleeve bearing and shortened to meet length requirements.

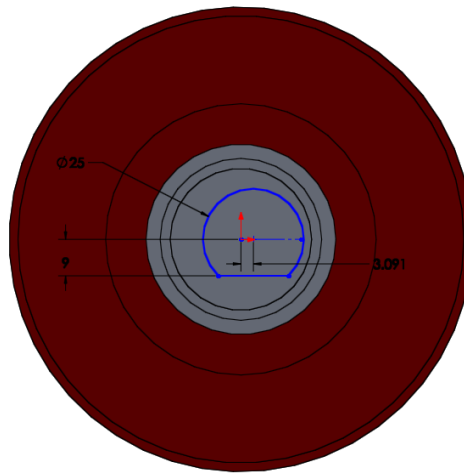
Finally, one can observe in Figure 4.7a two oil delivery holes drilled through the rotor, each designed according to a different lubricant distribution method. As described in [10], an initial off-axis through-hole design (design "A"), similar to the Copeland system, was chosen to deliver the oil to the top of the expander. However, the cost and difficulty of the operation is not well-matched with the project's ultimate goal which is to provide a cost effective technology appropriate to developing countries. Therefore, another method (design "B") that is easier to realize is selected and described in section 4.1.7.

4.1.4 Casing elements and fixtures

The expander external envelop is a semi-hermetic pressure vessel consisting of three elements represented in Figure 4.8a : the bottom flange (c), the expander inlet (a) and the central casing (d). These three pieces are assem-



(a) Cross section showing oil delivery holes through the shaft



(b) Crank offset equal to $R' = 3.091mm$

Figure 4.7: Generator rotor design features

bled with 24 bolts uniformly distributed around the upper and lower flanges. Two gaskets (b) are placed between each piece so as to ensure a leak proof expander sealing. Concerning the inlet flange, the upper cylinder is threaded for connecting an intake fluid manifold to the expander. On the other side, a mating surface is machined to fit with the upper BPC floating piston seal. Within the bottom flange are four supporting notches designed to locate the cross support. Finally, the central casing is a cylinder with six ports. As illustrated in Figure 4.8a, there is the expander outlet, an electrical connection port for extracting generator output and sensor wires, and four “stability ports.” The purpose of the latter is to improve the overall structural stability by pinching the low stator with 4 set screws placed around it, and to maintain its axial alignment. The stability ports are sealed with plugs to ensure the system remains hermetic.

The structural skeleton comprises fixtures supporting the different elements at their correct relative locations. As can be seen in Figure 4.8b, these include:

- **a low stator** (*a*) carrying the thrust bearing, with a central hole fitting the middle journal bearing and four threaded holes to support the linear bearings;
- **a supporting belt** (*b*) keeping the generator coil at its correct location and carried by the four supporting poles;
- **a cross support** (*c*) press fitted in the four bottom flange notches. The central hole positions the flanged sleeve bearing supporting the rotor.
- **four supporting poles** (*d*) connecting the three aforementioned pieces. Holes on both end are drilled and tapped to bolt them to the cross support and the low stator.

4.1.5 Bearings

Mechanical axial compliance of the two scrolls to take up wear is facilitated by four linear bearings represented in Figure 4.9 (*a*). Radial forces are however supported by three journal bearings located on the top (*b*), the middle (*d*) and the bottom (*c*) of the rotor. The overall axial load from the scrolls is supported by a thrust bearing placed just under the orbiting scroll (*e*). As can be seen in Figure 4.9, a groove is made in the contact area so as to get a uniform oil film supplied by two passages drilled through the piece. As described in Chapter 2, thrust bearing diameters are sized as a function of the scroll geometry so as to maintain a theoretical axial clearance of $15\mu m$.

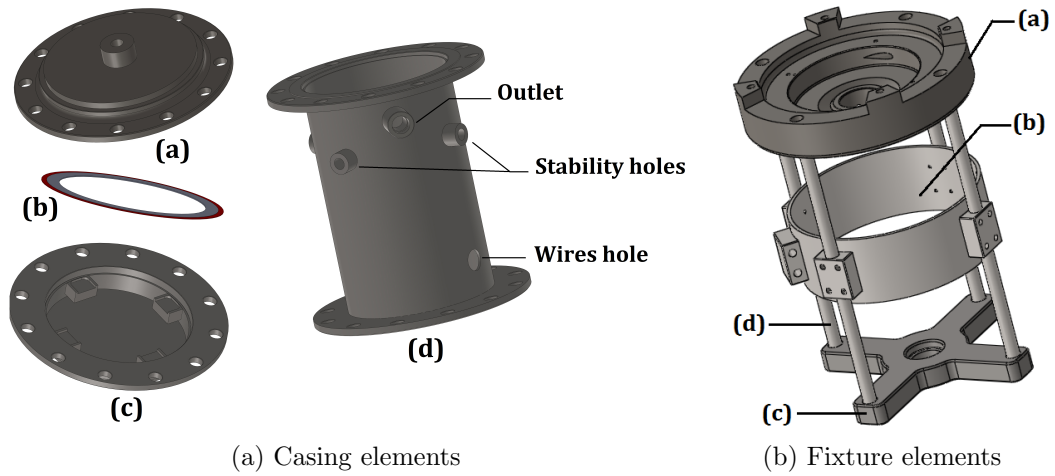


Figure 4.8: Fixtures and casing

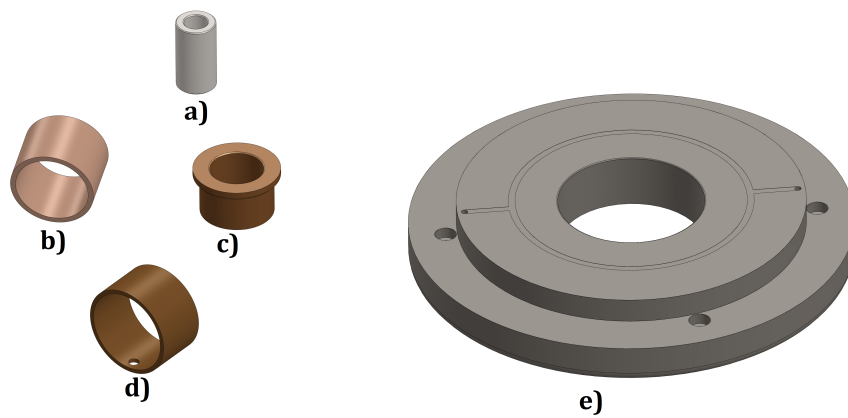


Figure 4.9: Journal bearings (left) and thrust bearing (right) of the expander prototype

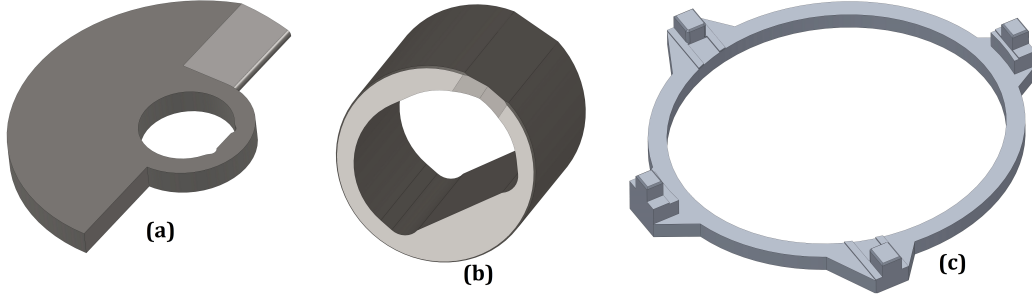


Figure 4.10: Counterweight (left), shaft adapter (middle) and Oldham joint (right)

4.1.6 Counterweight, shaft adapter and Oldham joint

In dealing with the eccentric motion of the orbiting scroll, a counterweight is required to avoid mechanical vibrations. It is designed so as to cancel the resulting centrifugal force (given by $F = m.\omega.R^2$), i.e.:

$$F_{CW} = F_{o,scl} + F_{s,ad} + F_b \quad (4.2)$$

where F_{CW} , $F_{o,scl}$, $F_{s,ad}$, F_b are respectively the counterweight, the orbiting scroll, the shaft adapter and the upper bearing centrifugal forces.

The shaft adapter is an intermediate element interacting with the offset crank and turning within the orbiting scroll sleeve bearing, providing the degree of freedom needed to convert the orbiting motion of the scroll to shaft rotation. It is designed with some radial clearance (sliding of the crank) so as to ensure a compliant radial position of the orbiting scroll despite wear in the scroll walls enlarging the orbital radius over time.⁵ Furthermore, grooves and notches are provided to enable oil flow along the shaft adapter so as to lubricate the lower pieces.

Finally, to maintain an orbiting motion without angular misalignment and ensure mating of the two scrolls, an Oldham coupling, represented in Figure 4.10, is employed to fix the kinematic relationship of the scroll pair. Since this piece oscillates at high frequency (about 50 times per second), it is made of a lightweight strong material (i.e. aluminum) with four pads on the bottom so as to reduce contact area and thus friction losses.

⁵As described in the *Electric generator* section, a further additional radial clearance is employed to accommodate the slightly larger crank radius of the originally machined shaft

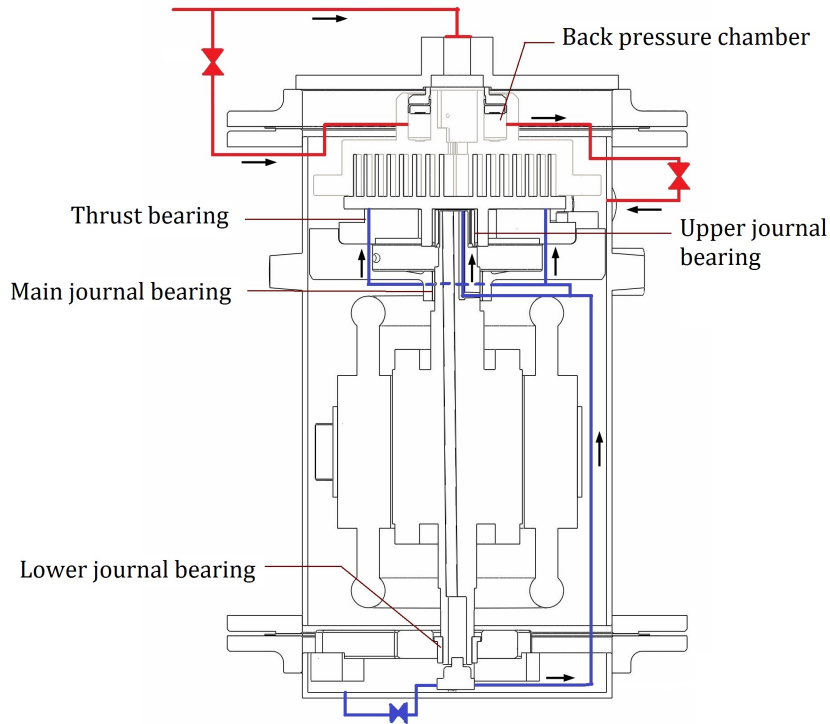


Figure 4.11: BPC (red) and lubrication (blue) circuits

4.1.7 Lubrication circuit

In order to reduce wear and mechanical losses by friction in the various bearings lubrication strategies are deployed. Based on a method described in the *Machinery's HandBook* [22] taking into account bearing size and loads supported, the entire system is estimated to require $0.23l/min$. Lubricant distribution is realized by the oil circuit represented in Figure 4.11 (in blue). Oil collected at the expander bottom is pumped by a modified motorcycle oil pump shown in Chapter 5. An external valve is used to control oil flow so as to find the optimal lubrication and a vertical pipe brings the oil up to the low stator. The flow is then divided, a first fraction goes through the rotor up to the shaft adapter and the upper journal bearing. The other oil fraction goes through the low stator to lubricate the thrust bearing. The oil then falls by gravity along the shaft and supplies the lower journal bearing fitted in the cross support.



Figure 4.12: Pieces 3D printed with a FDM printer

4.2 3D printing

Although CAD offers powerful visualization tools to verify the overall architecture, inconsistencies can remain. To ensure a kinematically viable design, a 60% scale model is 3D printed (by a printer *uPrint Dimension Elite*) using the FDM technique. *Fused Deposition Modeling* is a manufacturing technology based on an additive principle, i.e. by laying down a plastic filament (or a metal wire) in layers. As represented in Figure 4.12, only the thrust bearing, the Odham joint, the fixed and the orbiting scrolls are 3D printed since these components represent the most complex parts.

4.3 CAM with HSMXpress

Tool paths to control CNC machines are generated using the SolidWorks freeware add-on HSMXpress. This process facilitates rapid, complex and accurate operations and obviates the need to write G-code manually.⁶ The first CAM step, the job set up, consists of defining the type of operation (milling

⁶G-Code is the common name for a widely used numerical control (NC) programming language

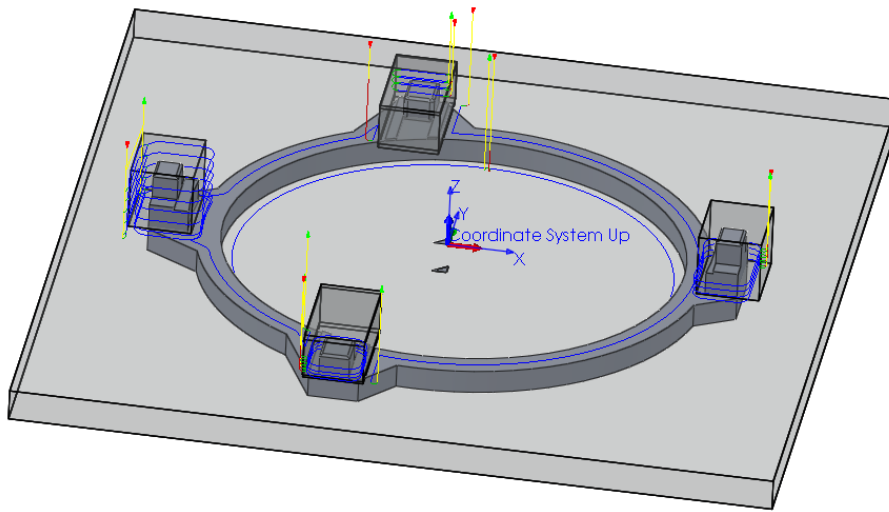


Figure 4.13: Tool paths generated for the Oldham joint

or tuning), the initial stock, the fixtures (arbitrary) and the coordinate system. Once the job is defined, the user can select and parameterize as many operations as are required. To do so, typical parameters to set up are:

- type of work: drill, face, trace, contour, pocket clearing, slot, thread, bore, etc;
- tool selection;
- spindle speed, feed rate and depth of cut;
- location of operation, stock to leave, clearance, retract and feed heights, etc.

To verify the generated tool path, the user can simulate the operation and check its viability visually. During the simulation the speed of simulation, the stock to show, etc., can be controlled by the user. Once the code is verified, it is exported as a *.nc* file containing all the relevant G-code instructions. An example is illustrated in Figure 4.13 for the Oldham joint (all the CAM files relative to the different parts are contained within the CD attached to this thesis).

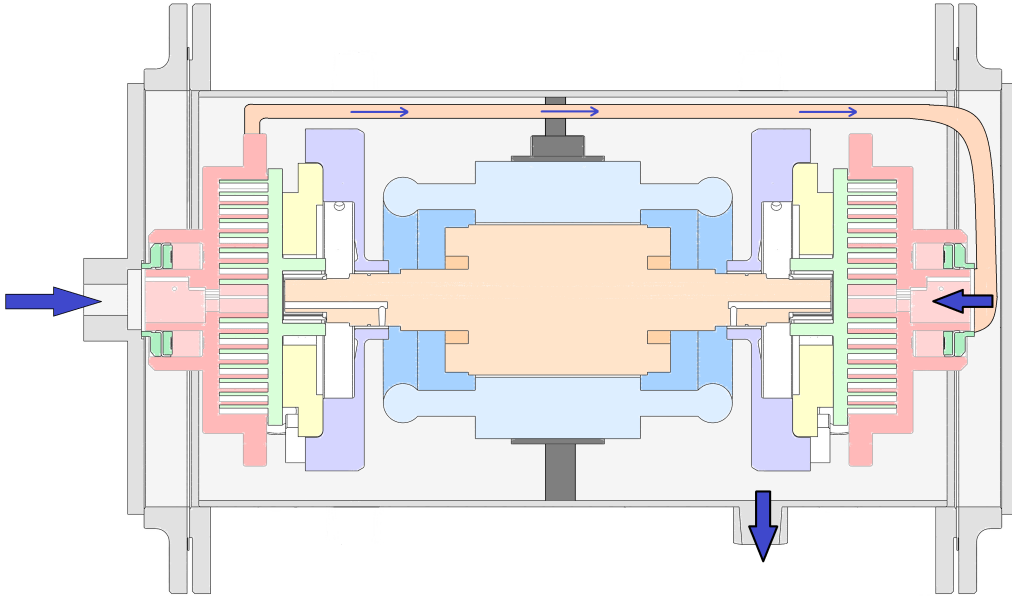


Figure 4.14: Draft overview of the two-stage prototype

4.4 Draft of the two-stage/single-shaft scroll expander

To conclude this chapter, a first draft version of the two-stage/single-shaft scroll expander prototype is presented in Figure 4.14. In this architecture, the working fluid enters the first expansion stage on the left, is expanded in the first stage and ducted to the second stage (on the right). As can be observed, both expansion stages are installed on a common rotor and thus rotate at the same spindle speed. Hence, electricity is produced by only one generator resulting in a single output voltage and frequency. Furthermore, this design also halves the power electronics required, which make the expansion unit simpler and less expensive. However, it should be noted that the architecture presented in Figure 4.14 is a concept sketch that will be refined later in the project, and as such is outside the scope of the present work.

Chapter 5

Manufacturing of a single stage prototype

This chapter covers the practical part of the project: the fabrication of the single stage prototype described in the previous chapter. First, a brief description of the relevant tools and machines is given. Relevant elements of manufacturing theory are then presented, followed by a brief discussion of material selection. Finally, a summary of the operations required to manufacture all the parts and an overview of the assembly are given.

5.1 Machines and tools

The fabrication of a prototype requires many operations performed by various machines and tools. The following section describes the main ones used in this project.

5.1.1 Machines

Lathe

A lathe is a machine tool for shaping a piece of material by rotating it while pressing a fixed cutting tool against it. This process produces features on the workpiece having a symmetry about its axis of rotation. Standard lathe operations include cutting, turning, facing, drilling, knurling, boring or reaming. The lathes used in this project include a HAAS CNC turning center and a Monarch manual engine lathe represented in Figure 5.1.¹ The manual lathe has been upgraded with a DRO (*Digital Read Out*), providing a display of the actual tool position along the Z and X axes. While most operations are

¹built by *Monarch and Co.* in 1941, this machine is still fully functional

realizable manually, some pieces requiring more complex profiles (machining of a round corner, better accuracy or higher spindle speed) require the use of a CNC lathe.

Milling machine

A mill is a machine tool in which a workpiece attached to a table is fed against a rotating cutter that shapes it. Standard operations with a milling machine include drilling, facing, flank milling and end milling. Unlike with a lathe, there is not limitation to symmetrical profiling when shaping with a milling machine. The mill used in this project is a vertical CNC milling machine built by Vectrax and is represented in Figure 5.2. The table holding the workpiece can be controlled in three different ways: manually, using the “Manual Data Input” (MDI) command field to enter G-codes (definition of tool location coordinates) or by uploading a document with G-codes generated by a CAM program such as HSMXpress. As explained previously, a tight manufacturing tolerance ($10\mu m$) is required to avoid flank and radial leakages. Such tolerance requires a CNC machine tool with a high degree of accuracy and repeatability; for the scroll wraps themselves a HAAS machine center is used.

Welding station

A welding station is a set of equipment required to achieve a welding operation. In the frame of this project, only MIG (*metal inert gas*) welding has been used. One can find a more detailed description of this technology in section 5.2.3. The station used to fabricate the prototype is a HOBART handler 210 and is represented in Figure 5.4. The main components are an hand-held welding gun, a shield gas bottle supply, a wire feed unit, a power supply and a grounding clamp.

Bandsaw

A bandsaw is a cutting tool which uses a blade consisting of a continuous band of metal with teeth along one edge. The blade is driven by two wheels rotating in a same plane. In this project, rough and fast cuts of any kind are realized with vertical and horizontal bandsaws as represented in Figure 5.3.

Driller

A drilling machine is a device fitted with an end cutting tool that is rotated with sufficient power either to create a hole or to enlarge an existing hole in a

solid material. Both hand-drill and drill press are used during the fabrication process of the prototype.

Belt sander

A belt sander is an electric sander fitted with a revolving abrasive belt. It is used to sand down materials for finishing purposes.

Machine coolant system

A coolant system, while comparatively simple, is crucial in machining hard materials. As a piece is machined, heat is generated because of friction between the tool and the work surface. Except in the case of light cuts, cutting operations generate more heat than surrounding air (having a low thermal conductivity) can remove. Because of this thermal imbalance, it results an increase of the cutter and workpiece temperatures which causes two main problems: excessive tool temperature decreasing its lifetime, and an excessive work surface temperature generating local thermal expansion, which negatively influences the tolerance. To prevent these problems, a water-oil based *cutting fluid* is projected at the cutter-chip interface so as to limit these temperatures. The oil fraction reduces friction between the tool cutting edge and the chip and ameliorates rusting of machine parts. In this project, coolant is used in all operations on the lathe, the bandsaw and the mill.

5.1.2 Tools

The fabrication of a prototype includes use of many hand tools (hammer, wrench, caliper, allen keys, etc.) and cutting tools. The following section gives a non-exhaustive description of main cutters and other tools employed alongside the machines.

Cutting tool material

In order to insure a good machining quality, a cutting tool must present three main properties. Firstly the cutter material must be harder than the workpiece material. It also must be tough enough to prevent chipping or fracture. Furthermore, the cutting tool needs to maintain its properties at high temperatures in order to withstand the heat generated in the metal-cutting process. Finally, it must withstand wear in use and last long enough to justify the expense. Tool materials may be classified in two main categories: *stable* and *unstable* materials. Unstable materials require an initial

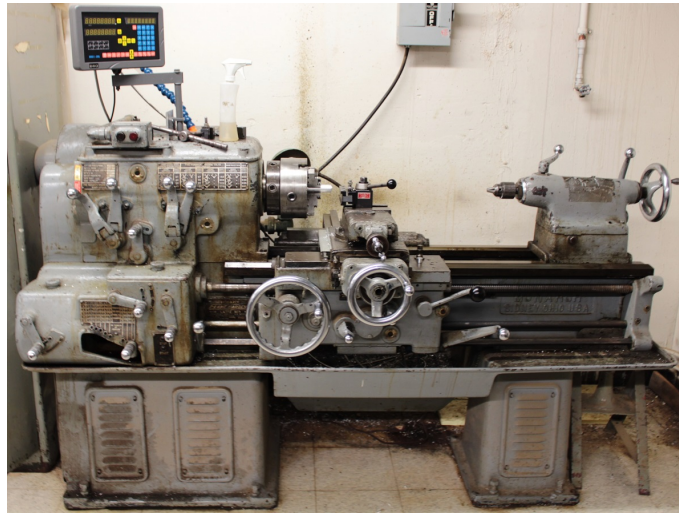


Figure 5.1: Lathe + DRO



Figure 5.2: CNC milling machine



Figure 5.3: Horizontal bandsaw



Figure 5.4: MIG welding station



Figure 5.5: Coolant system

heat treatment to obtain their mechanical properties. They are called *unstable* since their hardness is generally influenced by the surrounding thermal environment. On the other hand, stable materials retain their mechanical properties despite variable operating conditions. Table 5.1 represents the different types of tool material used in this project.

Drilling tools

In Figure 5.7 illustrates a regular twist drill bit, a center-drill and a hole saw. Drill bits are cylindrical cutting tools characterized by a length, a lip angle, a point angle and a spiral shape. They are used to drill holes and they exist in many sizes following different measurement standards (metric, fractional-inch and US numbers systems). Center-drills are smaller and thicker drill bits used to predrill an engaging hole so as to facilitate a subsequent job. Hole saws are used to bore relatively large diameter holes in thin material and they take the form of an open cylinder with saw-teeth on the open edge. In this project, hole saws are used to create the different holes in the casing.

Name	Un/stable
HSS (High Speed Steel)	Unstable
HSS + Colbalt	Unstable
Cemented carbide	Stable
Coated carbide (TiN and TiCN)	stable

Table 5.1: Tool materials used in the project

Lathe tools

As aforementioned, a lathe can be used for different types of machining operations, and each of them requires a dedicated tool. Figure 5.6 presents a cutoff blade, a turning/facing cutter and a boring tool.

Tapping tools

Threads in a pre-drilled hole are created in a tapping operation with a twist-cutting tool called a *tap*. Figure 5.8 illustrates a typical tap as well two tap-handles required to apply the tool. Taps used in this project are made of uncoated and TiCN-coated HSS.

Milling tools

Milling machines can perform several types of operations and these generally require a specific tool, with tool changes occurring in between operations. In addition to the drill bits described previously, Figure 5.9 displays the different tools used in the frame of this thesis. An edge finder is used to accurately determine edges of a workpiece during the set-up phase of a machining operation, while flat and ball end mills are used for shaping operations. Milling cutters are classified according various criteria: four or two flutes cutter, centered-cutting or non-center-cutting (unable to realize plunging cuts) cutter, flat or ball end mill, etc. Finally, one can see a replaceable carbide-insert end mill. Though more expensive initially, it facilitates replacement of worn or broken carbide-inserts rather than the entire tool which is more economical over the long term.

5.2 Elements of manufacturing theory

Some relevant elements of manufacturing theory are described in this section. First, a brief note about measurement systems is presented, followed by discussion of feed rate, depth of cut and spindle speed. Next, the theory of metal inert gas welding is discussed. Finally a description of tolerances and fitting standards is given.

5.2.1 Measurement systems

A measurement system is a set of units used to quantify an item according to length in 1-3 dimensions. In machining, the length units define the contours and geometries of the workpiece to be shaped. In the USA, two standards of

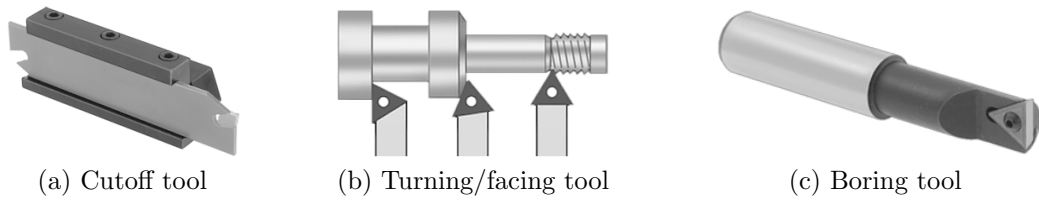


Figure 5.6: Lathe tools

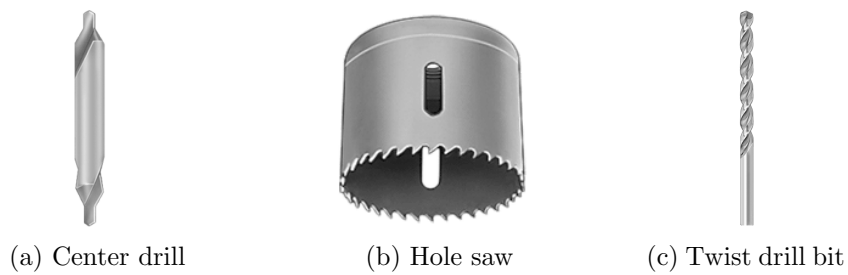


Figure 5.7: Drilling tools

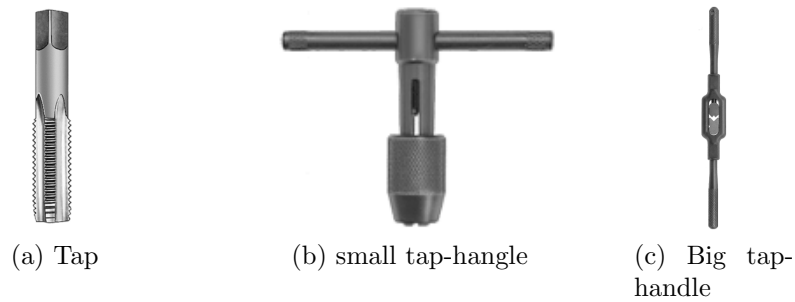


Figure 5.8: Tapping tools

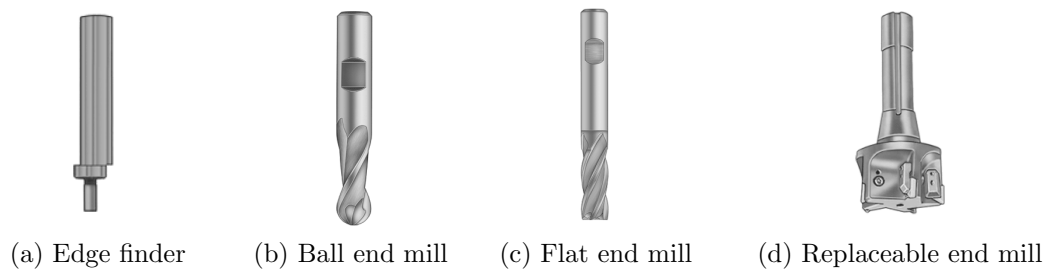


Figure 5.9: Milling tools

Unit		Division		SI equivalent
1 inch (in)	=	/	=	25.4 mm
1 foot (ft)	=	12 in	=	30.48 cm
1 yard (yd)	=	3 ft	=	0.914 m
1 mile (mi)	=	1760 yd	=	1.609 km

Table 5.2: US and SI systems comparison

measurement coexist: the *Imperial* and the *Metric* systems. Table 5.2 provides a brief summary describing these two measurement standards. It should be noted that in machining, *in* and *mm* are the most common length units employed. While metric measures use a decimal display, imperial lengths are generally expressed in term of a fraction multiple of $\frac{1}{64}$ (examples: $\frac{7}{64}in$, $\frac{9}{16}in$, or $\frac{3}{4}in$).²

5.2.2 Feed rate, depth of cut and cutting speed

Cutting speed, feed rate and depth of cut are important machining parameters for operations involving relative motion between the tool and the workpiece. These parameters are vital since they influence the surface quality, the roughness, the tool lifetime, the machining time and the operation tolerance.

Cutting speed is defined as the relative velocity between the cutting edge of a tool and the workpiece surface it is operating on. It is expressed in unit of length per unit of time, typically m/min (meter per minute) or sfpm (surface feet per minute). Optimal cutting speed is function of many factors such as the cutter and workpiece materials, the cutter and workpiece geometries, the use or not of a coolant system, the target machining quality, the chosen feed rate and depth of cut, etc. From a workpiece material point of view, the softer the work material, the faster the cutting speed. As described in Figure 5.10, Aluminum generally accepts a much higher cutting speed than hard steel. Conversely, as can be seen in Figure 5.11, the softer the cutter material, the slower the cutting speed. Optimal cutting speeds can be found in reference websites or books like the *Machinery's Handbook* [22], extensively used in this project. From a selected cutting speed, one can easily derive the spindle speed of the tool or the piece using one of the following relation:

²While conversions between the systems appear trivial, the use of two different systems has been the source of much confusion resulting in accidents in the engineering world, for example the loss of the Mars Climate Orbiter in 1998.

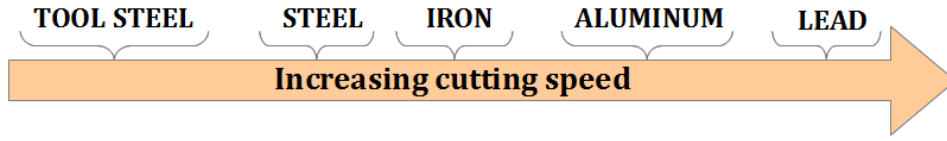


Figure 5.10: Effect of the workpiece material on the cutting speed

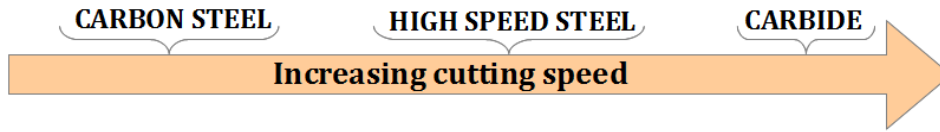


Figure 5.11: Effect of the tool material on the cutting speed

$$\underbrace{N = \frac{12 v_c}{\pi D}}_{\text{Imperial standard}} \quad \text{or} \quad \underbrace{N = \frac{1000 v_c}{\pi D}}_{\text{SI standard}} \quad (5.1)$$

where v_c is the cutting speed, D is the diameter of the tool (mill and drill) or the workpiece (lathe) and N is the spindle speed in rpm [8].

Feed rate is defined as the velocity at which the cutter is fed against the workpiece. Like cutting speed, feed rate depends on the tool and workpiece materials, the surface finish desired, the number of teeth or flutes, the spindle speed and the available spindle power of the machine. Feed rate can be either expressed in units of length per revolution (for milling and boring - *in/rev* or *mm/rev*) or in units of length per time (for milling - *in/min* or *mm/min*) depending on the operation. Because references give the chip load (feed per tooth) for a type of operation, feed rate can be derived using the relation

$$FR = N R_{th} f_l \quad (5.2)$$

where FR is the feed rate, N is the spindle speed, R_{th} is the number of teeth (flutes) and f_l is the chip load (expressed in mm/tooth).

Values obtained with 5.1 and 5.2 are theoretical guidelines to optimize a machining process. However, in practice, a machinist observes and reacts to the process using, e.g., color and shape of chips, noise and other indicators to refine the feed rate and cutting speed. For example, blue or brown chips are representative of excessive operating temperature; an appropriate response is to reduce the spindle speed and the depth of cut.

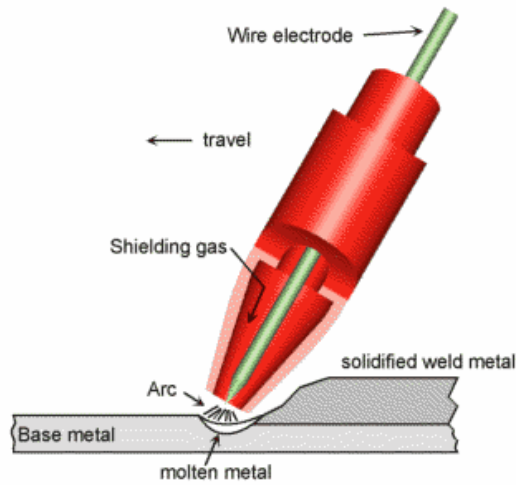


Figure 5.12: MIG welding principle

Figure 5.13: Welding equipments

5.2.3 MIG welding

Welding is the process of joining workpieces by melting them and resolidifying them, often involving adding a filler material to form a weld pool at the joint. *Metal Inert Gas* (aka MIG) welding, also called *Gas Metal Arc Welding* (aka GMAW), dates from 1920's and became commercially available in the 1940's. Today, this technology is the most common welding process used around the world.

The general principle has not changed much since its inception. Unlike TIG welding using a filler rod and a separate non-consumed electrode, MIG welding uses a consumable wire electrode that is continuously fed from a spool, as illustrated in Figure 5.12. An arc is then formed between the wire electrode and the workpieces which causes the wire to melt and become the filler material. As the name suggests, MIG welding uses a shielding gas to prevent exposure of the molten weld pool to the air. The reaction of O_2 , H_2 and N_2 with the weld pool can create problems including joint porosity and excessive splatter. Shielding gas also plays a major role in weld penetration, arc stability and mechanical properties of the joint. Typical shielding inert gas are He , Ar , CO_2 , and (rarely) H_2 , the choice depending of several factors such as the nature of material to be welded.

Welding is an art that requires many hours of practice and training to achieve acceptable results. The different parameters to be set up before a welding operation are the wire diameter, the voltage and the wire feed rate. Guidelines as a function of the thickness and the welded material are given on

the welding post. Finally, MIG welding is a hazardous operation that requires safety measures so as to prevent any severe injury. Indeed, high temperature arc (up to 4000 °C), splash and UV light stipulate that the welder to wear heavy leather gloves, long sleeve jackets and a protective helmet, as shown in Figure 5.13.

5.2.4 Tolerance and fits

Machining processes are real as opposed to ideal operations. Thermal expansion, tool wear and lack of precision are responsible for deviations between actual and theoretical dimensions. Tolerance is defined as the amount of variation permitted on dimensions of machine parts. It is equal to the difference between the maximum and minimum limits of any specified dimension. One can define a *unit of tolerance* i as

$$\frac{i}{\mu m} = \underbrace{0.45\left(\frac{D}{mm}\right)^3}_{\text{error in machining}} + \underbrace{0.001\left(\frac{D}{mm}\right)}_{\text{error in measurement}} \quad (5.3)$$

that describes, for any dimension D , a constant error in machining. From this unit of tolerance, it is then possible to define a *size of tolerance* TL_n as a function of the *tolerance grade* n chosen. The smaller the grade, the better the machining quality and the smaller the tolerance. Mathematically, a tolerance size of grade n is defined by

$$TL_n = k(n)i \quad (5.4)$$

where $k(n)$ is a constant given by ISO standards (for example, for a grade $n = 7, k(7) = 10$). One can distinguish accurate ($n \in [01 - 7]$), fit ($n \in [5 - 13]$) and draft ($n \in [14 - 18]$) machining qualities. After having defined the size of tolerance, it is important to determine its location relative to the basic dimension. ISO standards give different *types of tolerance*, for holes and shafts, that are labeled with a letter as represented in Figure 5.14. Detailed information about tolerance standards may be found in [9].

Like any mechanical system, the expander consists of an assembly of several pieces that require accurate matching. ISO standards provide normalized clearance, interference and transition fits as described in Figure 5.15. These fits ensure a viable assembly taking into account tolerances of the different pieces. Further information regarding fits is provided in the references [22] and [8]. In the case of journal bearings, one generally selects an H7/g6 clearance fit or uses the general rule of thumb to find an appropriate radial clearance

$$\frac{c_r}{mm} = \frac{(D/mm)^3}{90} \quad (5.5)$$

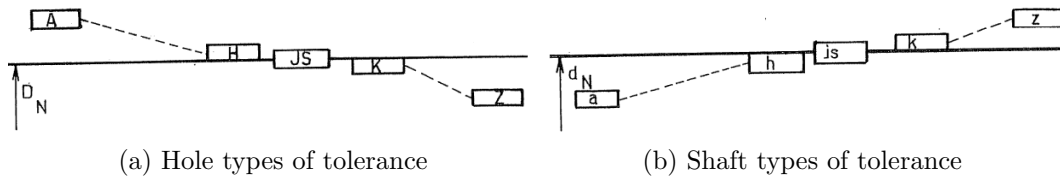


Figure 5.14: ISO types of tolerance

these two approaches giving the same order of magnitude.

5.3 Materials selection

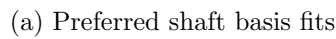
Material selection is an important step in the design of a prototype. The goal of this process is to choose a material that meets many performance requirements while minimizing cost. Theoretical strategy includes expression of an objective relation as described in [17]. One can then use an Ashby plot generated by a program, e.g. CES Selector, so as to visually identify the best candidate. Typical properties to take into account are:

- | | |
|------------------------|-------------------------|
| • Machinability | • Mechanical properties |
| • Weldability | – stiffness |
| • Density | – hardness |
| • Corrosion resistance | – fatigue resistance |
| • Price | – ductility |
| • Availability | – tensile strength |

Four materials are chosen to fabricate the expander: aluminum, carbon steel, P20 steel and oilite. A brief description of each of these materials as well a listing of the prototype pieces utilizing them is presented below.

Aluminum

Aluminum is the 13th chemical element in the periodic table. It is a silvery white, soft and ductile metal that presents good machinability and weldability properties. It is also widely used because of its low density and ability to resist corrosion. Two types of aluminum are employed in this project: the alloys 6061 and 2024. The first one provides a combination of good strength, machinability, corrosion and fatigue resistance, whereas the second



(b) ISO fits (Table from the *Machinery Hand book*, p647)

Figure 5.15: ISO fits

<i>Properties</i>	Al 6061	Al 2024	1018 steel	P20 steel	Oilite
<i>Density ($kg.m^{-3}$)</i>	2700	2780	7870	7833	6500
<i>Yield strength (MPa)</i>	242	296	373	840	76
<i>Hardness (Brinell)</i>	80	120	131	300	60

Table 5.3: Mechanical properties of the selected materials

one has increased strength by the addition of copper, which consequently decreases its corrosion resistance. Aluminum parts in the prototype include the four supporting tubes (flexibility), the two back pressure chamber seals (easy machinability and lightness) and the Oldham coupling (easy machinability and lightness).

Steel

Steel is an alloy of iron and carbon ($C_c \in [0.002 - 2.06]\%$). Many types of steel are differentiated by their compositions and heat treatments. In this project, two forms of steel are used to fabricate the expander prototype: an alloy steel commonly called 1018 and a tool steel called P20.

Unlike carbon steel containing only iron and carbon, alloy steel contains a variety of elements to improve its mechanical properties. The 1018 steel used in this project contains manganese (0.75%), phosphorous ($< 0.04\%$) and sulfur ($< 0.05\%$). It is the most commonly used and widely available alloy steel globally. It has a combination of interesting properties such as a good weldability, high strength and a good corrosion resistance. Parts made of 1018 steel are the low stator, the counterweight, the casing and the shaft adapter.

P20 steel is a tool steel belonging to the low-carbon mold steel group. Its main alloying elements are Carbon ($\sim 0.35\%$), Manganese ($\sim 0.8\%$), Chromium ($\sim 1.7\%$), Silicon ($\sim 0.5\%$) and Molybdenum ($\sim 0.45\%$). P20 steel is sometimes preferred because of its higher hardness and wear resistance. Parts made of P20 steel include the two scrolls and the thrust bearing.

Oilite

Oilite, also known as SAE 841, is a porous bronze alloy impregnated with an oil lubricant (SAE 30). It is formed using powder metallurgy and oil volume fraction is roughly 19%. Oilite is composed of Copper (88%), Tin (10%) and Iron (1%). The oil reduces wear as well as required maintenance. The three bearings in the prototype are made of Oilite.

Finally, it should be noted that some parts are prefabricated elements

adapted from other systems. These include the *shaft generator* which is an induction motor working reversely, the *oil pump* which is a small motorcycle oil pump, and the *four linear bearings* appropriated from a Copeland scroll compressor.

5.4 Operations summary and assembly

A complete description of each step of each machining process would be a prohibitively extensive undertaking, instead a summary is given in Table 5.4. Figure 5.16 provides an overview of all parts manufactured in this project i.e.

- | | |
|-----------------------------------|---------------------|
| a) Coil + support | j) Oldham joint |
| b) Generator rotor | k) Journal bearings |
| c) Bottom/top flanges | l) Counterweight |
| d) Low stator | m) Oil pump |
| e) Thrust bearing | n) Guiding tubes |
| f) Supporting tubes | o) Casing |
| g) Counter pressure chamber seals | p) Orbiting scroll |
| h) Shaft adapter | q) Fixed Scroll |
| i) Cross | |

Finally, one can find in Figures 5.17, 5.18, 5.19 and 5.20, four pictures taken during the first assembly of the prototype in June 2013 at MIT.

Table 5.4: Operation summary table

Piece	Material	Turning/Facing	Cutoff	Boring	Welding	Milling	Drilling	Tapping
<i>Bottom flange</i>	Steel	-	-	-	C	E	-	-
<i>Central cross</i>	Steel	-	-	A	-	E	E	-
<i>Shaft</i>	Steel	B	A/B	-	-	E	E	-
<i>Coil support</i>	Steel	-	F	-	C	E	E	G
<i>Bottom bearing</i>	Oilite	A	A	A	-	-	-	-
<i>Supporting tubes</i>	Al 2024	A	F	-	-	-	A	G
<i>Low stator</i>	1018 st	A/B	A	B	C	E	E	G
<i>Thrust bearing</i>	P20 st	B	-	A/B	-	E	B/E	-
<i>Counterweight</i>	1018 st	-	-	-	-	E	E	-
<i>Shaft adapter</i>	1018 st	A	A	-	-	E	A	-
<i>Main bearing</i>	Oilite	A	A	A	-	-	E	-
<i>Top bearing</i>	Oilite	A	A	A	-	-	-	-
<i>Oldham joint</i>	Al 2024	-	-	-	C	E	-	-
<i>Orbiting scroll</i>	P20 st	-	-	B	-	E	-	-
<i>Fixed scroll</i>	P20 st	-	-	-	-	E	E	-
<i>CP seals</i>	Al 6061	A	A	A	-	E	E	G
<i>Top flange</i>	Steel	A	A/F	A	C	E	A	-
<i>Casing</i>	Steel	-	-	-	C	E	D	G
<i>Oil pump</i>	Al 6061	-	-	H	-	-	D	-
<i>Guiding tubes</i>	Steel	-	-	-	-	-	-	-

A Manual lathe

B CNC lathe

C MIG Welding station

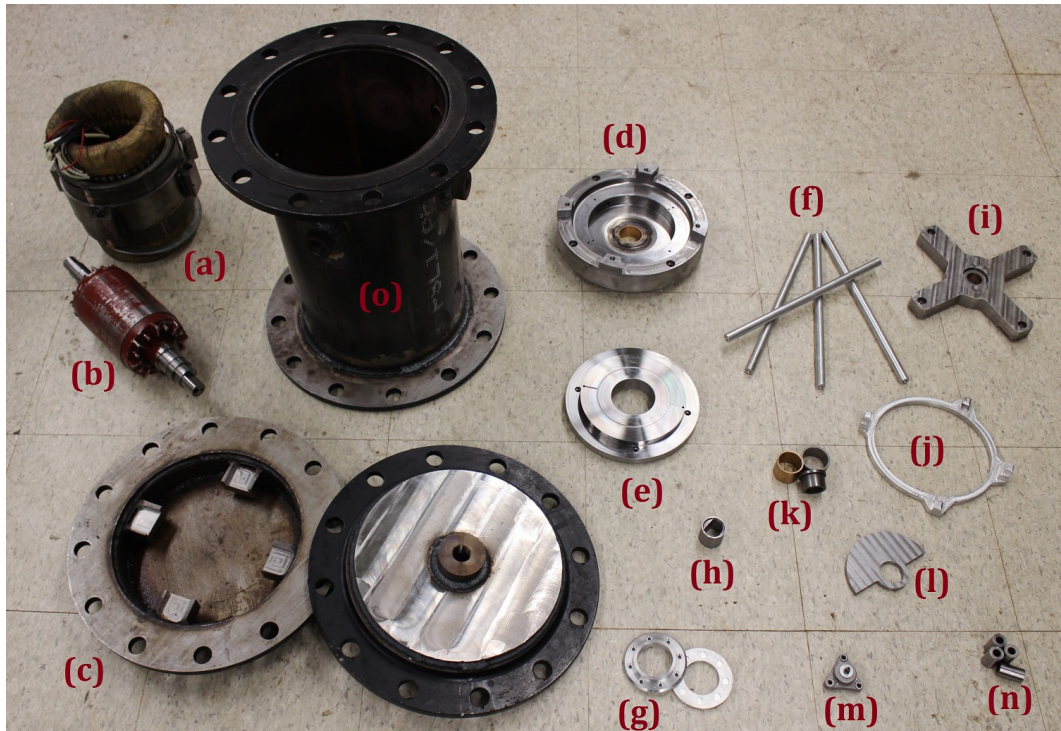
D Press driller

E CNC milling machine

F Horizontal bandsaw

G Hand taper

H Vertical bandsaw



(a) Pieces Overview



(b) Orbiting scroll

Figure 5.16: All the manufactured pieces

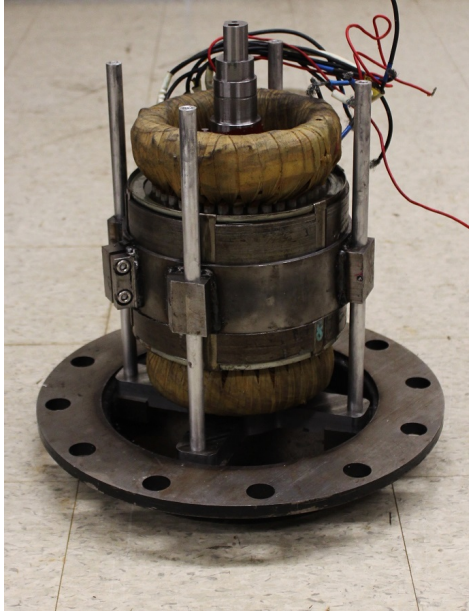


Figure 5.17: Assembly - Step A



Figure 5.18: Assembly - Step B



Figure 5.19: Assembly - Step C



Figure 5.20: Assembly - Step D

Chapter 6

MicroCSP test rig

This chapter describes a typical Micro-CSP plant for which the scroll expander is developed. The general working principle of this power plant with its main components is outlined. Subsequently, a simple thermodynamic model of an ORC is developed to investigate the influence of the expander efficiency and different operating conditions on the power plant performance.

6.1 CSP description

As referenced in the introduction, the project of *STG International* is to develop a renewable Micro-CSP technology in order to produce heat and electricity in remote areas of solar-resourced developing countries such as e.g. Lesotho and India. The working principle of such a power plant is presented in Figure 6.1 and can be summarized as follows:

Sun radiation is concentrated by the tracking parabolic trough collectors (PTC) onto a pipe located at the trough focal point. This focused solar energy is transferred to a heat transfer fluid (HTF), such as propylene glycol, circulating inside a selectively-coated absorber pipe insulated by a glass cylinder (2). Then, the working fluid (R245fa) absorbs heat from the HTF in the vaporizer and electricity is generated by the action of the expander in the organic Rankine cycle presented in Chapter 1. The generated electric power is then used to charge a bank of 48V-batteries which supplies the load (4) using a DC-AC converter. After the working fluid has passed through the scroll expanders and a regenerator, it is returned to a liquid state in the air-cooled condenser (5). Finally, a storage tank (6) installed between the collectors and the vaporizer is used as a thermal buffer to damp variability of solar insolation and provide a stable thermal source to the vaporizer, as well as enabling some extended operation through thermal energy storage. A complete operating diagram is given in Figure 6.3 in which one can see

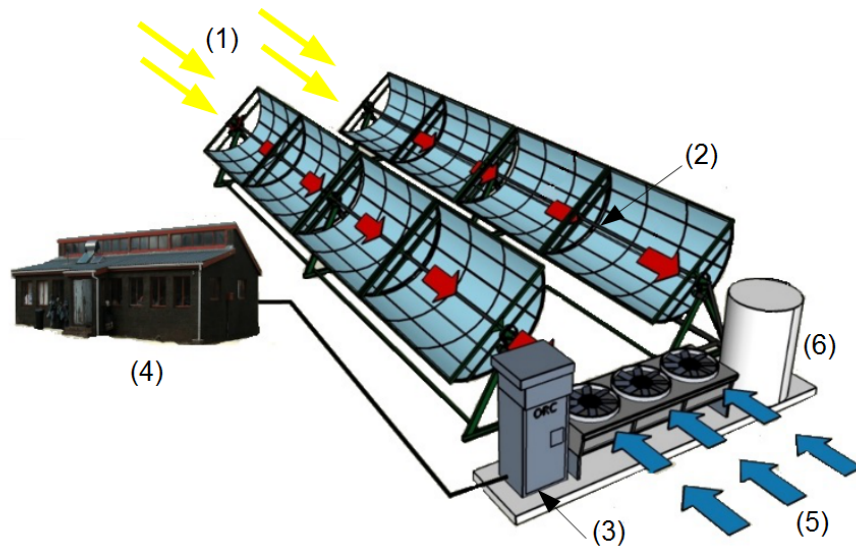


Figure 6.1: Working principle of a Micro-CSP system (source: STG international)

the Piping and Instrumentation diagram (P&I diagram) of a power plant built by *STG International*. Moreover, technical specifications of this kind of power plants are given in Table 6.1.

An example of such technology is the Micro-CSP test rig deployed by *STG International* on the Eckerd college campus in St. Petersburg, FL. Figures 6.4, 6.5 and 6.6 respectively show its parabolic trough collectors, the ORC unit and the thermal buffering tank. Furthermore, its main components are listed hereunder:

- **Solar collectors** - The solar array consists of 20 SopoNova linear parabolic troughs collectors manufactured by *Sopogy, Inc* employing single-axis tracking. Each module measures 1.50m wide and 3.60m long with a concentration ratio of roughly 38 and a mirror reflectivity of 89%. The total collected surface area of the array is $104m^2$.
- **Thermal tank** - Located between the collector array and the vaporizer, an insulated HTF tank is used as thermal storage in order to extend the daily operation time of the CSP. It also plays the role of thermal damper moderating temperature changes to provide a stable heat supply to the ORC.
- **Condenser** - Water often being a precious resource in underserved areas, this ORC uses an air-cooled tube-fin condenser with three fans of variable speed produced by *Russell* (model CAC-28) .

- **Expander** - Two Copeland scroll compressors arranged in series are currently used to perform the expansion process. The first stage expansion is performed by a ZR48 whereas the second one is carried out by a ZR125. Both are hermetic scrolls that have been converted to semi-hermetic scroll expanders.
- **Vaporizer and recuperator** - Both recuperator and vaporizer are brazed-plate heat exchangers manufactured by *ITT inc.* with a total exchange surface of $0.8m^2$ and $2.5m^2$ respectively.
- **HTF and WF pumps** - HTF is circulated by a *Dayton* gear pump (model NG11V-PH) driven by a 1hp 1800RPM 48VDC motor. The working fluid, on the other hand, is pumped by an *Hypro 2351B-P* plunger displacement pump with 3/4hp 48VDC motor drive.
- **Liquid receiver** - A liquid receiver is used to store the excess refrigerant circulated throughout the system, mainly due to 2-phase boundary fluctuations in the vaporizer.
- **Filter and dryer** - A filter is used in the HTF loop to prevent any entrained solid element from obstructing conduit or damaging fluid machinery. Similarly, a filter/dryer is used in the WF loop to remove any moisture which might have infiltrated the ORC loop.
- **Heating element** - A by-pass of the collector loop can be realized in order to operate the ORC even in case of bad weather (for experimental purposes). The heat is then provided by a heating element similar to the one used in a water heater (see Figure 6.2).



Figure 6.2: Heating element

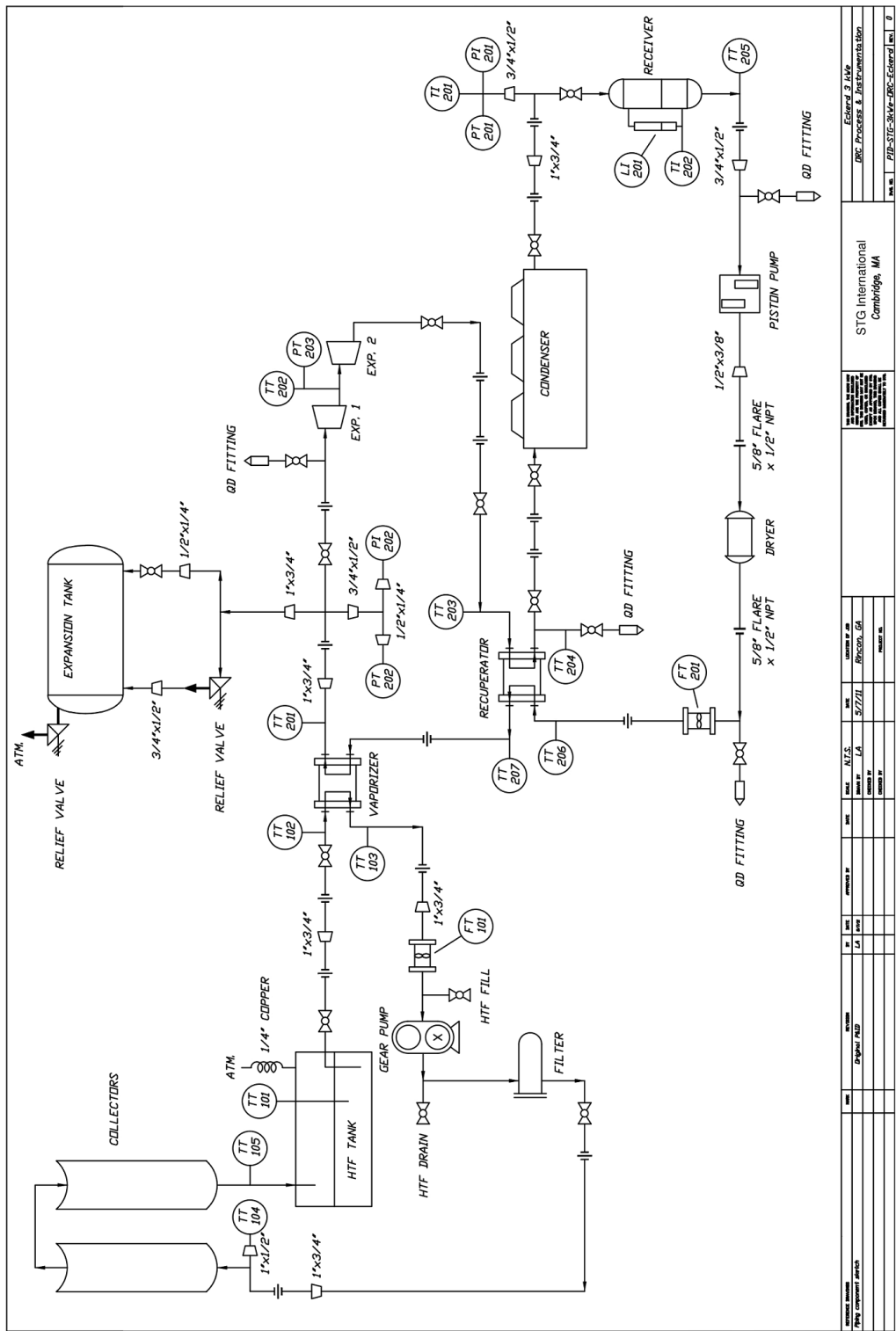


Figure 6.3: P&I diagram of a Micro-CSP (source: STG international)

MicroCSP Inputs		
Direct sunlight (peak)	800 – 1000	W/m^2
Direct sunlight (nominal)	400 – 600	W/m^2
Collector efficiency	50 – 70	%
Array surface area	70 – 100	m^2
Thermal input	40 – 60	kW
HTF temperature	160	$^{\circ}C$
ORC nominal working conditions		
Working fluid	R245fa	
mass flow	0.15	$kg.s^{-1}$
Evaporating temperature	135	$^{\circ}C$
High pressure	2500	kPa
Condensing temperature	35	$^{\circ}C$
Low pressure	250	kPa
Micro-CSP outputs		
Electric power	3 – 5	kW_e
Thermal power	20 – 25	kW_{th}
Thermal-electric efficiency	< 15	%
Solar-electric efficiency	2 – 10	%
Battery voltage	48	V
Daily hot water capacity	1000	l

Table 6.1: Technical specification of the Micro-CSP plant

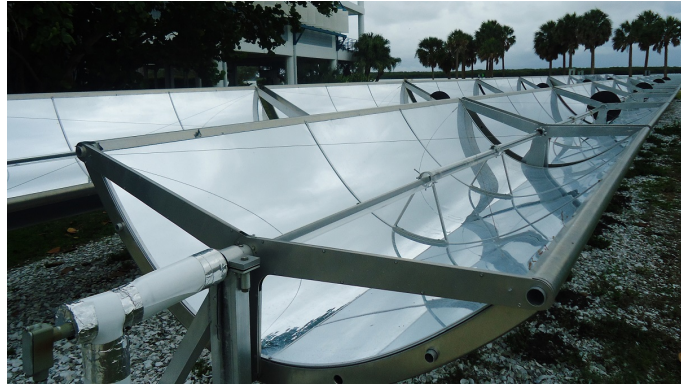


Figure 6.4: Parabolic trough collectors of the test rig

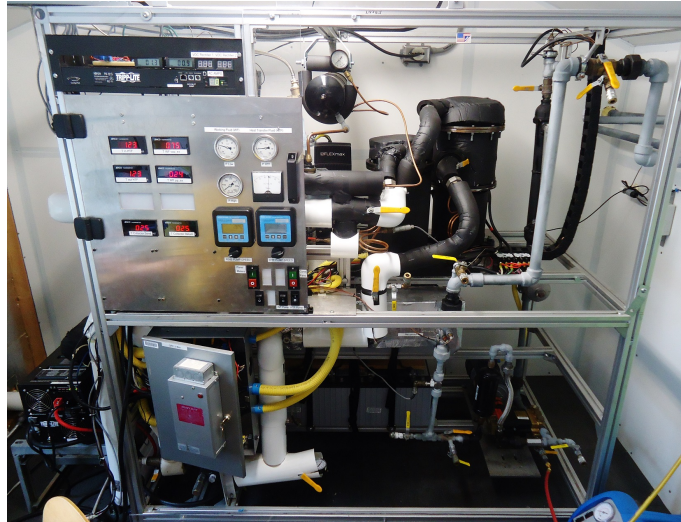


Figure 6.5: ORC unit of the test rig



Figure 6.6: Condenser and thermal tank of the test rig

Nominal conditions			
Pump efficiency	η_{cmp}	65	%
Expansion efficiency	η_{epx}	72	%
Carnot efficiency	η_{carnot}	25.42	%
Mass flow	\dot{m}	0.15	$kg.s^{-1}$
Evaporating temperature	T_{ev}	135	$^{\circ}C$
Superheating	SH	5	$^{\circ}C$
Condensing temperature	T_{cond}	35	$^{\circ}C$
Ambient temperature	T_{amb}	30	$^{\circ}C$
HTF max temperature	T_{HTF}	150	$^{\circ}C$
PTC efficiency	η_{PTC}	59	%

Table 6.2: Nominal conditions

6.2 Micro-CSP performance modeling

To conclude this thesis, a simple thermodynamic model of the ORC cycle is developed in Engineering Equation Solver (EES)¹ so as to evaluate the influence of different parameters on the Micro-CSP efficiency defined as

$$\eta_{MicroCSP} = \frac{\dot{W}_{net}}{\dot{Q}_{sun}} \quad (6.1)$$

$$= \frac{\dot{Q}_{ev}}{\dot{Q}_{sun}} \frac{\dot{W}_{net}}{\dot{Q}_{ev}} \quad (6.2)$$

$$= \eta_{PTC} \eta_{ORC} \quad (6.3)$$

where \dot{W}_{net} is the net mechanical power generated by the expanders, \dot{Q}_{ev} the heat transferred in the vaporizer, \dot{Q}_{sun} the heat concentrated by the solar collectors, η_{ORC} the ORC thermodynamic efficiency and η_{PTC} the solar collector efficiency. Table 6.2 describes the nominal operating conditions of the model and Figure 6.7 shows the related $h - s$ and $T - s$ diagrams for these conditions.

6.2.1 Influence of the condensing temperature

We first investigate the influence of the condensing temperature on the Micro-CSP performance. Since T_{cond} doesn't affect the PTC efficiency, the Micro-

¹the code can be found in appendix

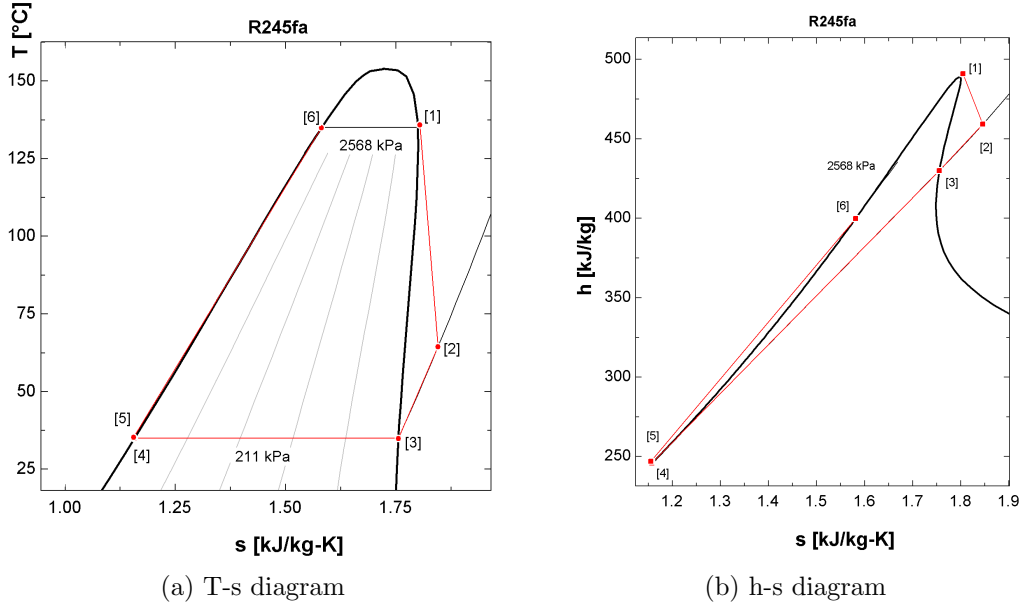


Figure 6.7: T-s and h-s diagrams of the ORC cycle under nominal conditions

CSP performance follows the evolution of η_{ORC} as a function of the condensing temperature. Results are displayed in Figure 6.8 and Table 6.3; note that the effect of T_{cond} on the ORC performance is linear. Specifically, a 5°C drop of the condensing temperature induces a 0.6% increase of η_{ORC} , 70 extra Watts generated during the expansion and 200 additional Watts required to vaporize the organic fluid. In other words, decreasing the condensing temperature by 8.6°C would result in a 1% increase the ORC efficiency.

However, it is important to keep in mind that the potential to decrease T_{cond} in a Micro-CSP application is limited. As discussed above, water is often too precious for cooling the condenser and ambient air is used to provide the necessary heat sink of the ORC. T_{cond} is thus higher (due to the heat exchanger pinch) than the outside temperature, which can be as high as 40°C for target deployment locations.

6.2.2 Influence of the expansion efficiency

In this section the impact of the the expansion efficiency on the Micro-CSP performance is examined. Analogous to the case of the condensing temperature, η_{exp} does not affect the PTC efficiency and the Micro-CSP performance follows the evolution of η_{ORC} as a function of the expansion efficiency. Results obtained by the simulation are shown in Figure 6.9 and few points are described in Table 6.4. As expected, the higher the expansion efficiency, the

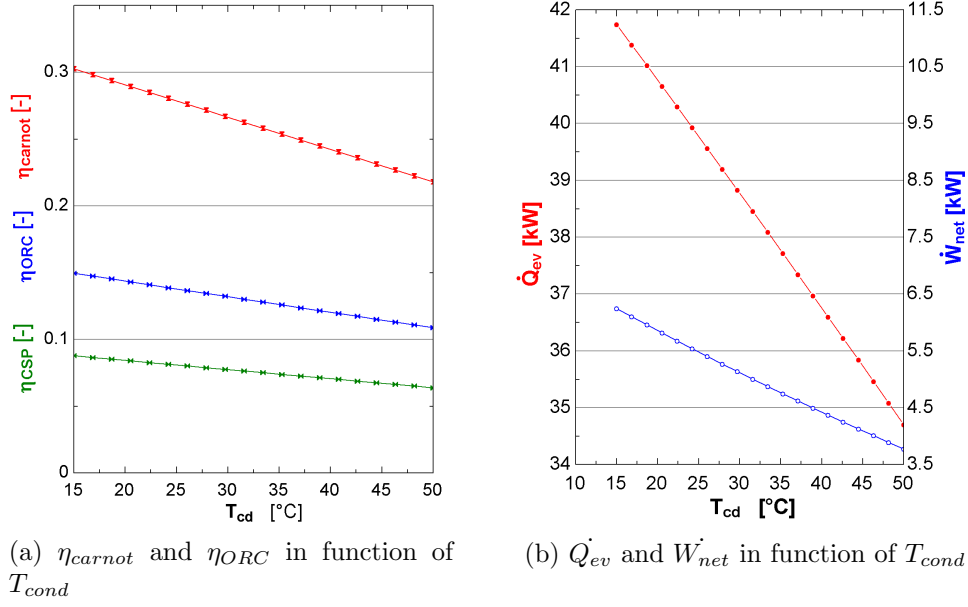


Figure 6.8: ORC performance in function of the condensing temperature

T_{cond}	η_{Carnot}	η_{ORC}	\dot{W}_{net}	\dot{Q}_{ev}
$[^{\circ}\text{C}]$	$[\%]$	$[\%]$	$[\text{kW}]$	$[\text{kW}]$
15	30.3	15	6.2	41.7
23.7	28.2	13.9	5.6	40.1
32.5	26.1	12.9	4.9	38.3
41.2	23.9	11.9	4.3	36.5
50	21.8	10.9	3.8	34.7
$\Delta - 5$	$\Delta 1.2$	$\Delta 0.6$	$\Delta 0.7$	$\Delta 1$

Table 6.3: ORC performance in function of the condensing temperature

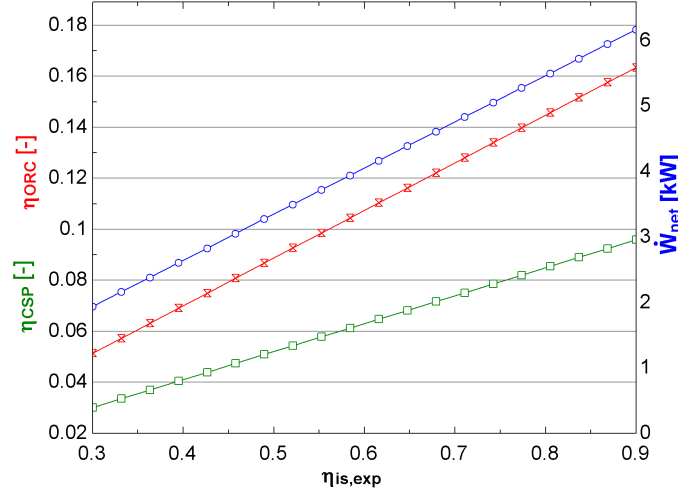


Figure 6.9: ORC performance as a function of the expansion efficiency

η_{exp}	η_{ORC}	\dot{W}_{net}
[%]	[%]	[kW]
30	5.1	1.9
45	7.9	3
60	10.7	4.1
75	13.6	5.1
90	16.3	6.2
$\Delta 1$	$\Delta 0.18$	$\Delta 0.07$

Table 6.4: ORC performance as a function of the expansion efficiency

better the ORC performance and the greater the net power generated. Numerically, its influence is linear and an increase of the expansion isentropic efficiency $\Delta\eta_{exp}$ of 1% results in a 0.19% increase of the ORC efficiency and 70 extra Watts produced. To achieve an increase of the ORC efficiency of 1%, the expander isentropic efficiency must increase by 5%.

As shown in Chapter 3, this project proposes to improve expansion efficiency by 6.2% (62.4% with two Copeland scroll compressors in series working reversely as compared to 68.6% with a two-stage/single-shaft scroll expander). Specifically, 5.03% of improvement is due to the optimized volumetric ratio whereas the decreasing wall thickness profiles contributes to 1.17%. This expansion improvement would thus result in an estimated 1.24% increase of the ORC efficiency.

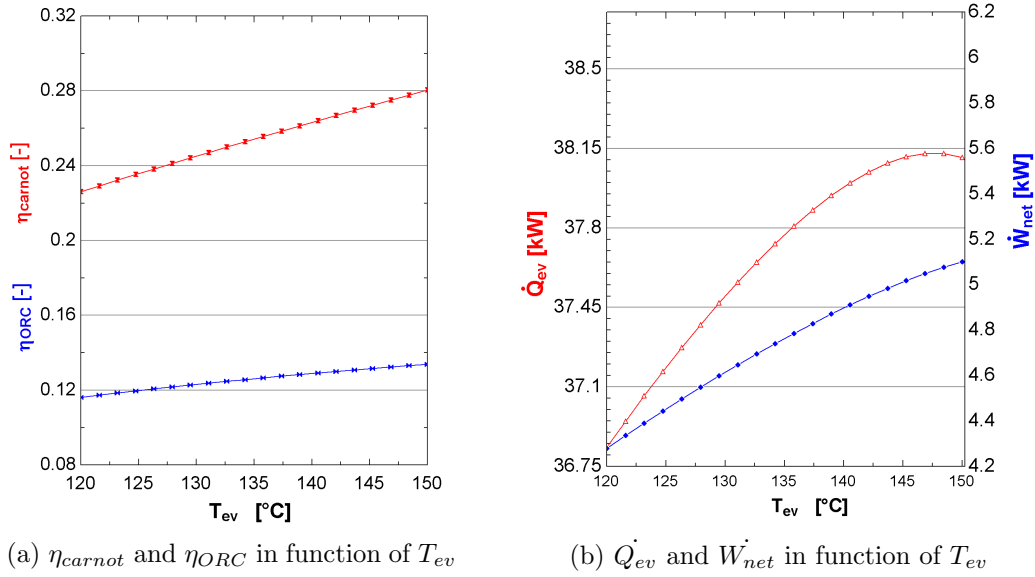


Figure 6.10: ORC performance as a function of the evaporating temperature

6.2.3 Influence of the evaporating temperature

Finally, we investigate the influence of the evaporating temperature on the Micro-CSP performance. Results are displayed in Figure 6.10 and Table 6.5; note that in this case the effect is non-linear. On average, a change of 5°C causes a 0.3% increase of η_{ORC} , requires 220 additional Watts for \dot{Q}_{ev} and enables production of 140 extra Watts for \dot{W}_{net} . Increasing the evaporating temperature by 17.1°C (on average, since T_{ev} effect on η_{ORC} is not linear) would be necessary in order to improve the ORC efficiency by 1%.

However, it is important to keep in mind that the potential to increase T_{ev}

T_{ev} [°C]	η_{Carnot} [%]	η_{ORC} [%]	\dot{Q}_{ev} [kW]	\dot{W}_{net} [kW]
120	22.6	11.6	36.8	4.3
127.5	24	12.1	37.4	4.5
135	25.4	12.6	37.8	4.8
142.5	26.7	13.1	38.1	5
150	28.1	13.4	38.1	5.1
$\Delta 5$	$\Delta 0.9$	$\Delta 0.3$	$\Delta 0.22$	$\Delta 0.14$

Table 6.5: ORC performance as a function of the evaporating temperature

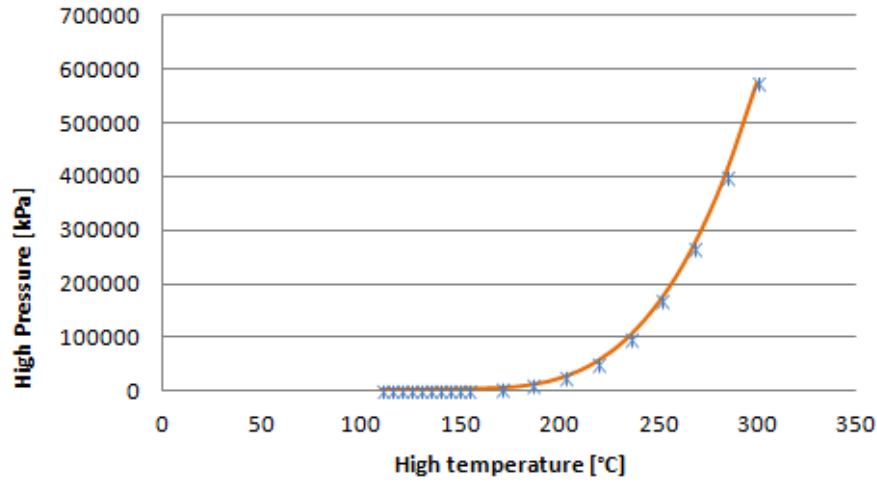


Figure 6.11: High pressure as a function of the "evaporating" temperature

in a Micro-CSP application is limited. A first limitation results from the pressure rise with the evaporating temperature: as indicated in Figure 6.11, the higher the evaporating temperature, the higher the corresponding pressure. Higher pressures require more robust and expensive components and to maintain unit safety, criteria which becomes an economic limitation concerning T_{ev} above a break-even value with respect to power generated. Furthermore, thermal efficiency of solar collectors decreases with the HTF temperature. As explained by Kutscher et al. [16], PTC thermal efficiency is a function of both the fraction of direct normal radiation absorbed by the receiver and the heat lost to the environment when the receiver is at operating temperature. The higher the HTF temperature, the greater the heat lost to the environment and thus the smaller the thermal efficiency (see Figure 6.13). It results an asymptotic temperature distribution along the collector as represented in Figure 6.12. In consequence, the additional collector surface area required to increase the HTF temperature by 1°C increases monotonically with the temperature itself. One thus encounters tradeoffs because of economic returns or available space at high temperatures.

As illustrated in Figure 6.14, the optimal T_{ev} maximizing the Micro-CSP efficiency is given by a trade-off between the PTC thermal efficiency (decreasing with T_{ev}), the ORC efficiency (rising with it) and the maximum high pressure authorized. As indicated above, however, the equipment costs of increased evaporating temperature may increase faster than the increase in system efficiency, i.e. the optimal evaporating temperature should be calculated by an analysis of the specific cost of energy using, e.g. discounted

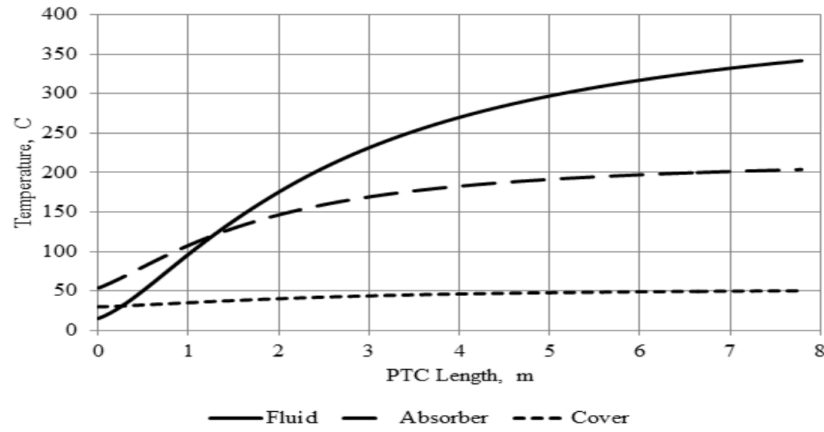


Figure 6.12: Temperature distribution along a PTC for the HTF, the absorber tube and the cover tube (source: Ashraf Kotb [15])

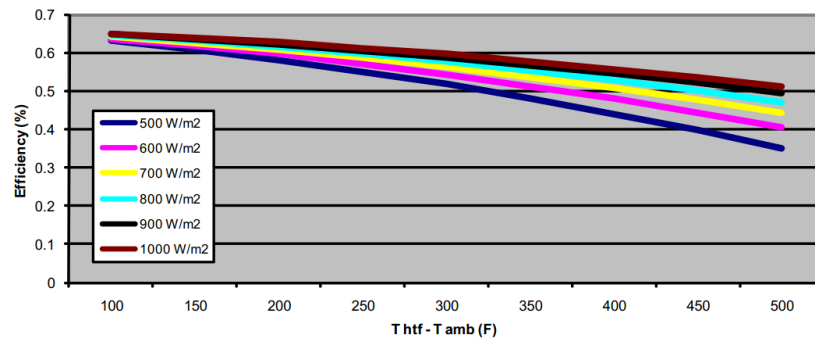


Figure 6.13: PTC thermal efficiency in function of the HTF temperature (source: SopoNova datasheet)

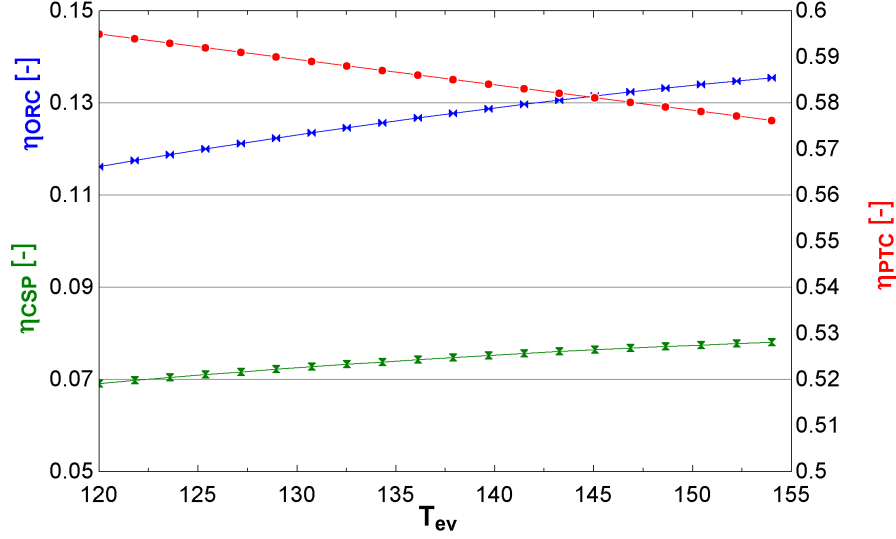


Figure 6.14: η_{PTC} , η_{ORC} and $\eta_{MicroCSP}$ in function of the evaporating temperature

cash flow (DCF) analysis for a given project specification or a metric such as levelized cost of electricity (see [24]). These topics are outside the scope of this study, which focuses on efficient expander design.

6.2.4 Results comparison

Finally, one can compare these three performance parameters as follow: in order to increase the Micro-CSP efficiency by 1%, one can:

- increase the evaporating temperature by $36.2^{\circ}C$ (on average, since T_{ev} effect on $\eta_{MicroCSP}$ is not linear);
- decrease the condensing temperature by $14.5^{\circ}C$;
- increase the expansion isentropic efficiency of 9%.

In light of the results given by this parametric study, the motivation for an investigation into optimized expander performance is clear: it is a powerful lever for improvement that can be influenced through mechanical design. As shown in Chapter 3, this project outlines a pathway for increasing the expansion efficiency for a Micro-CSP plant by 6.2% compared with best practices (68.6% with our two-stage/single-shaft scroll expander in comparison with 62.4% for two reversed Copeland scroll compressors in series). Specifically,

5.03% of improvement is due to the optimized volumetric ratio whereas the decreasing wall thickness profiles contributes to 1.17%. This expansion improvement would thus result in an overall 0.7316% increase of the MicroCSP efficiency under nominal conditions.

Chapter 7

Conclusion and perspectives

To conclude, the contents of this thesis are summarized as follows. In the first chapter, context and the rationale that motivated the project are initially described. Then an overview of ORCs and scroll expanders is presented to illuminate the purpose and nature of this work.

In the second chapter, the deterministic model developed by Dechesne [10] is presented and modified with particular focus given to improved methods for representing mechanical losses occurring in the scroll expander.

Chapter 3 presents the Danfoss framework used to generate variable wall thickness scroll geometries and identifies the interdependence of its parameters. Using this framework, a database including 30,000 geometries is generated, and a selection process is described leading to the selection of two optimal scroll candidates for primary and secondary expansion stages. The thermodynamic performance improvement achieved by this design is evaluated. We conclude that the isentropic efficiency improvement (6.2%) of this new design, in comparison to a standard system (using constant wall thickness scrolls), is mainly due to the optimized volumetric ratio (5.03%) with an additional 1.17% resulting from compactness achieved via a decreasing wall thickness profile.

Following the selection of scroll geometry, Chapter 4 presents a CAD model developed in SolidWorks for a single-stage prototype. This prototype is being developed to validate predictions of the design and evaluation programs with experimental data. The various constituent elements and some design details are also described.

Chapter 5 presents the practical part of the project, i.e. the manufacturing and fabrication of the single stage prototype. Tools and machines used in the project are presented and relevant elements of manufacturing theory are detailed. Finally, an operations summary and visuals of the assembled prototype are given.

To conclude, Chapter 6 describes a typical Micro-CSP plant for which

the scroll expander is being developed. After having presented the general working principle of such a power plant and its main components, a simple thermodynamic model is developed to investigate the influence of different operating parameters on the power plant performance. This study indicates us that the 6.2% expander efficiency improvement predicted by this design process would enhance the Micro-CSP performance by 0.7316% under nominal conditions.

This thesis is one part of an ongoing, multi-faceted project, and provides a foundation for further research and development. Guidelines and tasks for advancing to a further stage in the project include the steps listed below:

- select the pressure sensors for the fixed scroll and machine their mounting features
- check the envelope sealing with a pressurized test and eliminate any leakage
- realize the oil delivery and the BPC circuits piping;
- run the single-stage prototype as a compressor to *wear in* the mating surfaces;
- once the prototype is fully checked, install it in the Eckerd College solar ORC test rig and generate operational data;
- compare these experimental measurements with predicted performance by the deterministic model;
- according to the degree of validation of the design tool and deterministic model, identify improvements to the process as needed, following the selection process described in Chapter 3;
- develop and test the two-stage/single-shaft scroll expander prototype

Appendix

For the sake of conciseness, appendices are provided in an attached CD to this report. The reader can thus have access to the different files created in *EES*, *Matlab* and *SolidWorks* with which results mentioned in this thesis are obtained. Moreover, pictures of each piece and some manufacturing processes are also given. The directories structure of the attached CD is as follows:

```
Attached CD
├── Datasheets and papers
│   ├── Datasheets
│   ├── Papers
│   └── Thesis
├── EES files
├── Excel files
├── Matlab files
│   ├── 1st stage - results
│   ├── 2nd stage - results
│   ├── Deterministic model related codes
│   ├── Scroll database
│   └── Scroll generation related codes
├── MSc thesis
├── Pictures
│   ├── Assembly
│   ├── Machines
│   ├── Manufacturing processes
│   └── Zoom on each component
└── SolidWorks files
    ├── 3D print
    ├── Copies & beta versions
    ├── Pictures
    └── Components and assembly
```

Bibliography

- [1] Air squared - scroll expander produces 1kw of quiet power. <http://airsquared.com/news/patented-scroll-expander-produces-1-kw-of-quiet-power>.
- [2] Emerson official website, compressor section. http://www.emersonclimate.com/en-US/products/compressors/scroll_compressors/Pages/scroll_compressors.aspx.
- [3] World bank data, access to electricity (% of population. <http://data.worldbank.org/indicator/EG.ELC.ACCS.ZS/countries?display=graph>.
- [4] *Energy Resources: Occurrence, Production, use*. Springer, 2000.
- [5] I. Bell. *Theoretical and Experimental Analysis of Liquid Flooded Compression in Scroll Compressors*. PhD thesis, Purdue University, 2011.
- [6] J.-L. Caillat, S. Ni, and M. Daniels. A computer model for scroll compressors. *International Compressor Engineering Conference*, page 601, 1988.
- [7] Y. Chen. *Mathematical modeling of scroll compressors*. PhD thesis, Purdue University, December 2000.
- [8] J.-F. Debongnie. Cours d'usinage. *University of Liège*, 2006.
- [9] J.-F. Debongnie. Cours de conception mecanique. *University of Liège*, 2007.
- [10] B. J. Dechesne. Designing a scroll expander for a micro-solar power plant. Master's thesis, University of Liège, August 2012.
- [11] J. Gravensen and C. Henriksen. Danfoss: Scroll optimization. *32nd European Study Group with Industry*, 32:3–35, August 1998.

-
- [12] J. Gravensen and C. Henriksen. The geometry of the scroll compressor. *SIAM Review*, 43:113–126, 2001.
 - [13] B. Hamrock, S. Schmid, and B. Jacobson. *Fundamentals of Fluid Film Lubrication*, chapter Chapter 10 - Hydrodynamic Journal Bearings - Analytical Solutions. Taylor and Francis, 2004.
 - [14] Y. Hori. *Hydrodynamic Lubrication*, chapter Chapter 3. Fundamentals of Journal Bearings. Springer Tokyo, 2006.
 - [15] A. Kotb. Hourly simulation of parabolic trough solar collector with simultaneous solar radiation and weather conditions during sunshine period in cairo-egypt. *IOSR Journal of Engineering*, 3, 2013.
 - [16] C. Kutscher, J. Stynes, and F. Burkholder. Generation of a parabolic trough collector efficiency curve from separate measurements of outdoor optical efficiency and indoor receiver heat loss. *J. Sol. Energy Eng.*, 3, 2013.
 - [17] J. Lecomte-Beckers. Cours de sélection des matériaux. *University of Liège*, 2011.
 - [18] V. Lemort. *Contribution to the Characterization of Scroll Machines in Compressor and Expander Modes*. PhD thesis, University of Liège, 2008.
 - [19] V. Lemort. Production de froid et chaleur basse temperature. *University of Liège*, 2010.
 - [20] V. Lemort, S. Declaye, and S. Quoilin. Experimental characterization of a hermetic scroll expander for use in a micro-scale rankine cycle. *Proceedings of the Institution of Mechanical Engineers, Part A, Journal of Power and Energy*, 2011.
 - [21] J. Manzagol, P. dHarboul, G. Claudet, and G. Gistau Bague. Cryogenic scroll expander for claudet cycle with cooling power of 10 to 100 watts at 4.2 k. *Cryogenic Engineering Conference*, 47, July 2002.
 - [22] E. Oberg, F. Jones, H. Horton, and H. Ryffel. *Machinery's Handbook 26th Edition*. Industrial Press Inc., 2000.
 - [23] E. Orallil, Md. Ali Tarique, C. Zamfirescu, and I. Dincer. A study on scroll compressor conversion into expander for rankine cycles. *International Journal of Low-Carbon Technologies*, 6:200–206, April 2011.

-
- [24] M. S. Orosz. *ThermoSolar and Photovoltaic Hybridization for Small Scale Distribute Generation: Applications for Powering Rural Health*. PhD thesis, Massachusetts Institute of Technology.
 - [25] M. S. Orosz, A. V. Mueller, B. J. Deschene, and H. F. Hemond. Geometric design of scroll expander optimized for small organic rankine cycles. *Journal of Engineering for Gas Turbine power*, 135, March 2013.
 - [26] S. Quoilin. *Sustainable Energy Conversion Through the Use of Organic Rankine Cycles for Waste Heat Recovery and Solar Applications*. PhD thesis, University of Liège.
 - [27] T. Walter, C. Gossweiler, and B. Willson. Application of an improved model for the determination of acoustic resonances in indicator passages for combustion pressure measurements. *Kistler Instruments Review*.
 - [28] U. Wang. The rise of concentrating solar thermal power. *Renewable Energy World.com*, 2011.